PhD Dissertation

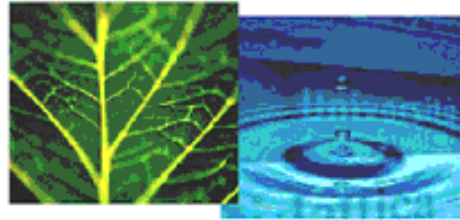**International Doctorate School in Information and Communication Technologies**

DIT - University of Trento

Study of the electromechanic aspects of RF MEM devices with particular emphasis on the dynamic behavior for the case of RF MEM switches and tuneable capacitors

Parisa Ture Savadkoohi

Advisor:

Dr. Benno Margesin

MEMS Unit, Fondazione Bruno Kessler (FBK), Povo, Trento, Italy

---

April 2010

Abstract

Research on MEMS (Micro Electro Mechanical systems) has seen an amazing growth during the last 15 years, stimulated both by their interesting physical properties and their attractive application potential. One of those appealing MEMS applications are Radio Frequency (RF) switches. These devices have some outstanding advantages like low insertion loss, high isolation and linearity, but they suffer from some drawbacks like low switching speed and lack of reliability. In the near future for many applications, like mobile phones and communication systems, reliable switches with higher commutation speed are expected. This thesis is focused on the study of the dynamic behavior of the RF switches with the aim to find suitable ways to develop switch geometries with faster switching characteristic. The study considers process related aspects, theoretical calculations, numerical simulations and dynamic measurements. In addition other devices that are useful for the design of the complex RF circuits and that are characterized by a complex dynamic behavior like in plane forces are studied.

Keywords [RF MEMS, Electromechanic, Dynamic, Charging, Varactor]

Contents

List of Tables

List of Figures

Chapter 1

Introduction

This chapter provides a brief overview on MEMS, on the current research activities on RF MEMS switches, MEMS varactors and MEMS technologies and introduces the main motivations of the work presented in the thesis. Finally the structure of the thesis will be presented.

1.1 MEMS Overview

Today MEMS is a generic term commonly used to describe micro scale devices that typically involve some sort of mechanical movement. These devices and related technologies are a branch of the microelectronic devices. The microelectronic technology and the integrated circuit devices have experienced in the last twenty years an extraordinary development in many terms. Microelectronic devices have seen a tremendous reduction in minimum feature size from micron level at the end of the eighties to less than 100 nm today, following exactly the predictions of Moore's law. At the same time the integration capabilities on a single chip have grown by orders of magnitude, leading in this way to the powerful microprocessors and memory devices of these days. Amazingly this tremendous technological development has gone in parallel with a cost reduction never seen before. The overall cost of microprocessors and memory devices is now

much lower than twenty years ago and is steadily decreasing. The cost
reduction is even more dramatic if the cost of a single function (transistor,
memory cell, stored bit etc) is considered. All this could only be achieved
with the help of two assets: new and powerful microfabrication technologies
and large volume fabrication technologies. The field of MEMS devices and
related technologies evolved in parallel from the integrated circuit industry.
The intrinsic characteristics of these devices are again miniaturization, mi-
croelectronics integration and mass production. MEMS technology makes
it possible to combine electromechanical and microelectronic components
in a single device ranging from $1\mu m - 1$cm [52, 41, 39] and electromechan-
ical devices. Mechanical sensors and actuators with electronic processors
and controllers can be fabricated on a single substrate in an unbroken,
wafer-level process flow and integrated at chip level. Accurate dimensions
and placement precision are guaranteed by lithography. Also in this case
the batch-based fabrication process has the potential to be scaled up to suit
large volume needs and so reduce the cost and improve the yield and reli-
ability significantly [9]. The first practical applications of MEMS technol-
ogy were implemented in products such as tire pressure sensors as early as
1950's and now have developed into mass production of automotive airbag
sensors (accelerometers) and avionics equipment. Since 1970's, MEMS-
based sensors such as pressure and temperature sensors, accelerometers,
and gas chromatographs have been developed [41]. Also the integration
of MEMS technology in RF circuitry fabrication leads to revolutionary
progress in miniaturization, superior performance and lower manufactur-
ing cost of these devices. These superior performances made their ways
into a wide array of commercial, aerospace and defense application ar-
eas, including satellite communications systems, wireless communications
systems, instrumentation and radar systems. Among the basic RF compo-
nents one of the most important in RF microwave applications is the RF

MEMS switch. It is essentially a miniature device, which uses a mechanical movement to achieve an open- or short-circuit in a transmission line. Petersen was the first to demonstrate the possibility to build MEMS switches with simple cantilever beams [36, 37]. At the beginning only low-frequency MEMS devices were investigated, because they could be integrated with CMOS circuits. Therefore, many devices were based on polysilicon, which has excellent mechanical properties [16]. However, adventuring into the microwave field, it became apparent that a high-resistance material, such as polysilicon, could not be employed in low-loss circuits that are necessary in the microwave and millimeter-wave region (1-100 GHz). This led to the development of extremely low-loss metallic MEMS components. Au and Al are the most common materials used for this purpose [31]. They have some distinct advantages over solid-state devices such as low insertion loss, high isolation, low cost and high linearity. Current research on RF MEM components follows five distinct paths [39]:

- High-Q inductors: Even if conceptually simple these are probably the most crucial passive device in the RF field. Typical devices build in CMOS or bipolar technologies are clearly totally insufficient with respect to discrete devices and only of limited use. Many different technological approaches have shown that it is possible to build "air coil" devices with high Q values.

- Varactors: These are tunable capacitors, i.e. capacitors where the capacitance can be tuned via electrical means. These are enabling devices for essential complex circuits like tunable filters, matching networks, phase shifters, LC-tanks and low noise controlled oscillators. MEM varactors and inductors have been demonstrated from $DC-120$ GHz and are now a relatively mature technology.

- Resonators and filters: Another key device in the RF and microwave field are resonators, employed for example in the reference oscillators and more in general in all transceiver architectures.

- FBAR: Thin film bulk acoustic resonators and filters that use acoustic vibration in thin films have demonstrated excellent performance up to 3 GHz with very high $Q(> 2000)$. Also RF micromechanical resonators and filters that use the mechanical vibration of extremely small beams as a high Q resonance element have been demonstrate with success between 0.01-200 MHz.

- RF MEM switches: Last but not least these complex devices are the key element for all reconfigurable systems. In fact in the last 15 years most of the effort spend in research on RF MEMS was devoted to them.

RF switches are essential components for many systems in microwave technology such as mobile phones, WLAN systems, radars etc. The huge number of potential applications and the intrinsic drawbacks of the presently used components make the development of RF MEMS switches a highly desirable and viable alternative. Two basic types of RF MEM switches have been studied in terms of contact configuration, i.e. switches with either ohmic or capacitive contacts. Many different electromechanical types of RF MEM switches have been developed and tested but two types stand out for their performance and are therefore pursued by several different research organization: the electrostatically actuated capacitive shunt switch and the electrostatically actuated ohmic relay. They will be discussed in more detail in the next chapters.The majority of RF MEMS switches rely on the electrostatic actuation that based on the attractive Coulomb force that existed between charges and opposite polarity because of its simple fabrication and low power consumption . Radio Frequency and Microwave

Monolithic Integrated Circuits (RFICs and MMICs) fabricated on silicon substrates have obtained widespread use in personal communication, GPS, and other systems that are highly cost sensitive. The possibility of integrating low cost RF and microwave circuits with digital and analogue circuits on the same chip has created a strong interest in silicon as a microwave substrate. For the practical realization of MEMS devices there have been developed several different MEMS technologies that can be grouped in the broad categories outlined below.

- **Bulk micromachining:** In bulk micromachining, the 3-D structure is sculpted within the confines of a wafer by exploiting the anisotropic etching characteristics of different atomic crystallographic planes in the wafer. Alternatively, structures may be formed by the process of fusion bonding, which entails building up a structure by atomically bonding various wafers.

- **Surface micromachining:** In surface micromachining, the 3-D structure is built up by the orchestrated addition and removal of a sequence of thin film layers to/from the wafer surface, which are called structural and sacrificial layers respectively. The success of this approach usually depends on the ability to release/dissolve the sacrificial layers while preserving the integrity of the structural layers and therefore depends on the relative selectivity of the dissolving/etching processes.

- **LIGA:** LIGA is a technology which creates small, but relatively high aspect ratio devices using x-ray lithography. The process typically starts with a sheet of PMMA. The PMMA is covered with a photo mask, and then exposed to high energy x-rays. The mask allows parts

of the PMMA to be exposed to the x-rays, while protecting other parts. The PMMA is then placed in a suitable etchant to remove the exposed areas, resulting in extremely precise, microscopic mechanical elements. LIGA is a relatively inexpensive fabrication technology, especially when based on optical lithography, and suitable for applications requiring higher aspect ratio devices than those achievable in Surface Micromachining.

- **Deep Reactive Ion Etching:** Deep Reactive Ion Etching (DRIE)is a type of Bulk Micromachining technique, which etches mechanical elements into a silicon wafer. Unlike traditional Bulk Micromachining, which uses a wet chemical etch, DRIE micromachining is based on plasma etching to create the features. This allows greater flexibility in the etch profiles, enabling the fabrication of a wider array of mechanical elements. Because the fabrication tools needed to perform DRIE is quite expensive, i.e. this technology is typically more expensive than traditional Bulk Micromachining based on wet etching.

- **Integrated MEMS Technologies:** Since MEMS devices are created with the same tools used to create integrated circuits, in some cases it is actually possible to fabricate Micromachines and Microelectronics on the same piece of silicon. Fabricating electromechanic devices and transistors side by side enables the realization of devices that can have some intelligence on board. A number of exciting products are already taking advantage of this capability to build smart electromechanic components.

1.1.1 General Fabrication Process and Materials

The fabrication process design criteria and the choice of materials include the compatibility with standard IC fabrication processes and all the crit-

ical switch parameter specifications. In general, RF MEMS switches are fabricated using a combination of surface micro-machining and a set of processing steps selected from standard integrated circuit manufacturing technologies. Excluding the packaging, most of the reported RF MEMS switches are realized using five to ten mask levels with a process sequence which may vary for different implementations. While selection of the wafer, overall thermal budget, material etching and deposition techniques are influenced by general process compatibility issues, contact and structural material considerations determine the switch parameters including contact resistance, metal to metal sticking behavior, life time expectation and environmental and packaging compatibility. In spite of the diverse process designs and implementations, the basic steps are similar, as summarized below and shown in Fig.1.1.

1. For RF MEMS very often a low-loss, high resistivity substrate is the starting material. Thermally oxidized high resistivity silicon ($> 3k\Omega - cm$)[33] is generally preferred, but GaAs [10] or glass e.g. quartz or AF45 [37] have also been used.

2. The transmission or interconnecting lines are realized by depositing and patterning a thick (3-5μm). highly conducting layer e.g. Au, Cu or Al[34]. Low temperature deposition techniques such as sputtering or electroplating are generally preferred for the deposition of the metal layers. In three terminal devices the actuation electrodes and biasing resistors are patterned in polysilicon or high resistive and resistant metals. The capacitive contact area under the bridge may have one or more metal layers (e.g. Ti- Al-1%Si-TiN) in order to provide a low resistivity path with smooth surface.

3. A thin (0.1 - 0.3μm) dielectric layer is deposited and patterned for the capacitive switch contacts and electric isolation of the actuation electrodes. Low temperature (e.g. $< 350°C$) processing is needed to avoid the adverse

effects of high temperature on the bottom metal layers. Mostly PECVD dielectric constant materials [51] and PECVD oxide are preferred, however the use of high dielectric constant materials like anodized tantalum oxide [21] or sputtered strontium titanate oxide [34] have also been demonstrated.

4. The next step consists of sacrificial layer deposition and patterning. Polymers like positive photo resist or polyamide [33], [34], 2-4μm in thickness are spin-coated and patterned. The sacrificial layer thickness determines the 'air gap' between the bridge and the capacitive contact.

5. Typically the freely moving structural part is defined by depositing and patterning 1- 2μm thick metal layers on top of the sacrificial polymer deposited in step 4. High conductivity thermally-stable metals with low fatigue are preferred. In current designs the metals are aluminum alloys, gold or nickel .

6. The final step consists of the removal of sacrificial layer using a proper release process to avoid stiction [10]. It is carried out at low temperature e.g. an isotropic dry etch in oxygen plasma if photo resist or polyimide is the sacrificial layer. The above mentioned steps are the minimum number of steps needed to fabricate an electrostatically actuated capacitive switch. For ohmic switching devices the dielectric over the contact is replaced by a contact metal, e.g. gold [20]. In capacitive devices, a thin (0.1 - 0.3um) and smooth bottom electrode (underpass) is often added locally at the switch contacts to ensure good down capacitance requiring intimate contact with minimal air gap caused by protrusions. Refractory metals such as tungsten or titanium [29, 24], with high conductivity and which retain smoothness after subsequent temperature steps are preferred.
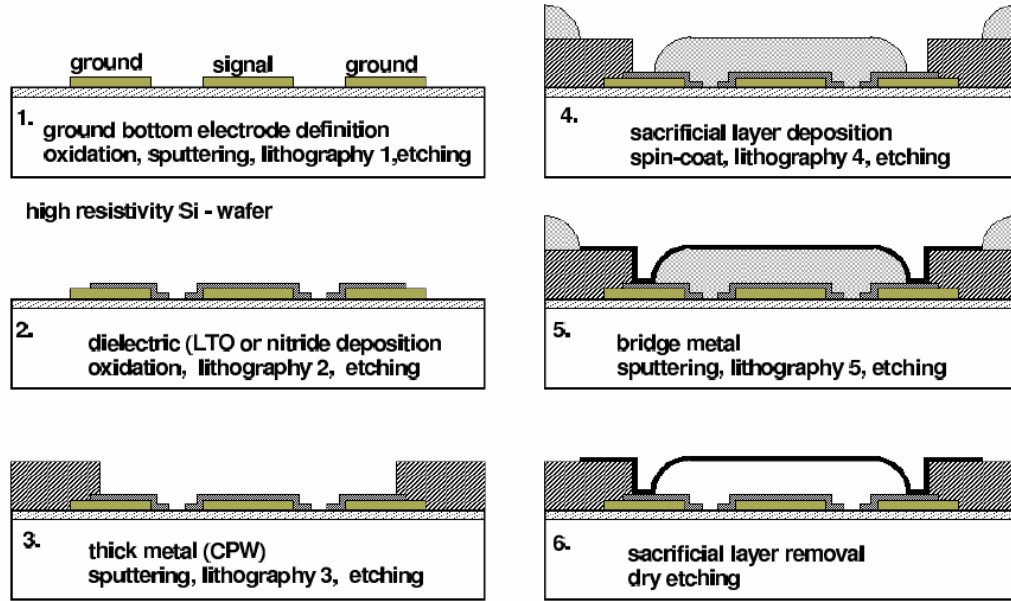
Figure 1.1: General fabrication process sequence for RF MEMS capacitive switch in CPW transmission line configuration

1.2 Motivation and Context

MEMS switches and other components have been very interesting area for research and development in the last few years [39, 49]. It is well known that they have excellent performances at microwave to mm-wave frequencies. In comparison with other types of switches (e.g. GaAs-based FET, pHEMT or PIN-diode switches), MEMS switches offer lower insertion loss and higher isolation, zero power consumption, small size and weight and very low intermodulation distorsion. Regarding the current research topics in this field, within this general and also local context and fostered by the ever increasing demand for low cost communication, the need for low power, multifunctionality, higher speed of the electromechanic switches is one of the major aspects that not yet matches the requests coming from the system applications, which therefore has been chosen as the primary investigation area covered within this thesis work. Developing a switch design

or even a new type of process that leads to devices with shorter switching times has a potentially strong impact on system architectures and could allow the use of these devices in applications beyond their current capabilities. This would also represent a big improvement in the technological capabilities of FBK. In parallel it is of high interest to enhance the device library of the FBK process by adding other devices useful for the construction of complex RF circuits, also in view of the platform approach of the FBK technology. Among these devices, tuneable capacitors are of high interest for a variety of applications. Regarding the RF MEM switch the main aspect studied was the switching time itself, but also other aspects such as high actuation voltage, self actuation and stiction have been considered. The main purpose of the research work consists in the investigation of the different effects contributing to the switching time and the means to reduce/mitigate them. As stated above switching speed is one of the disadvantages of MEMS components compared to PIN diodes and FET transistors. While their mass is typically very small, inertia due to mechanical movement still limits their speed typically in the order of a few microseconds, whereas typical values for solid state devices are in the nanosecond range. As there are essentially three aspects involved in the dynamic response of electrostatic switches, i.e. the natural mechanical frequency, the impact velocity and the relaxation time, the research work has been focused on them. In addition, different designs as well as different operating modes have been considered and studied by modelling, dynamic measurements and numerical calculation in the attempt to find out the best methodology for the design of faster switch topologies. Moreover, most of the designs of RF MEM switches consider just vertical mechanical movements. Therefore the study of a switch based on a lateral movement is of interest, at least form a basic research point of view. Therefore one part of our research work has been focused on the design and modelling of

a novel structure based on electrostatically induced torsion.

1.3 Innovative Aspects

Different phenomena that affect the switching time are modelled and discussed. Some solutions to overcome drawbacks like slow switching times and stiction are presented together with the results of the experimental measurements, which show that the adopted methodology and the design solutions are effective. In addition some new geometries designed to explore devices with lateral movement are presented. The results of the measurements show that the devices are mechanically functional and exhibit small switching times.

1.4 Thesis Overview

A general introduction of MEMS and RF MEMS and the actual disadvantages of the RF MEMS switches are discussed in ***chapter 1***, together with an overview of the thesis.

In ***chapter 2*** a detailed discussion of RF MEM switches is given. In particular different types of actuation mechanisms, mechanical movements and contact types, as well as the adopted circuit and substrate configurations are discussed, together with the most important RF MEMS applications, technologies and issues related to reliability and the switching time.

In ***chapter 3*** the mechanical equations of motion, viscous flow, spring constant and critical stress are introduced. Two types of actuation mechanisms such as the parallel plate actuator and the electrostatic comb drive are shortly introduced and a comparison of this two actuation mechanisms is made. In addition electrical, mechanical and environmental degradation

will be discussed.

A brief introduction to numerical modelling of the dynamic response of switches, their switching time and related phenomena are presented in *chapter 4*, together with an analysis of the relevant design factors and process parameters that determine the dynamic response of the switches. In *chapter 5*, a brief description about the fabrication of three of the studied devices is given. Next the static CV measurements, the 3-D profilometer measurements and the dynamic measurements performed at the University of Padova with the kind permission and help of Prof. G. Meneghesso and Dr. A. Tazzoli will be presented. The measurement setup for the dynamic characterization will be presented in some detail. The closure times and release times under different actuation voltage pulses will be discussed in detail and the results of the experimental measurements will be compared with simulations. Finally the means which can be helpful in developing switches with improved mechanical performance will be discussed.

Chapter 6 is dedicated to the design of a varactor prototype based on a lateral movement and the problems encountered. An improved design, that includes a comb drive mechanism for the lateral movement, is presented. As these devices (from a purely mechanical point of view) act also in a switch-like manner, the results obtained in terms of actuation time are compared with those of the other discussed geometries.

In *chapter 7* a summary of the results is given and the possible future work outlined.

Chapter 2

Radio Frequency RF MEMS Switches: an Overview

2.1 Introduction

Basically MEMS switches are devices that use a mechanical movement to achieve a short circuit or an open circuit in an RF transmission line. RF MEMS switches are specific micromechanical switches that are designed to operate at RF-to-millimetre-wave frequencies (0.1 to 100 GHz). The forces required for the mechanical movement can be applied using either electrostatic, magneto static, piezoelectric or thermal effects. The majority of RF MEMS switches rely on electrostatic actuation, which is based on the attractive Coulomb force existing between charges of opposite polarity. Electrostatic devices are characterized by low power consumption as power is ideally consumed only during the switching. In addition they can be build with relatively simple fabrication technologies [49, 39] and are suitable for wafer-scale manufacturing techniques. MEMS switches show remarkable advantages over their solid state counterparts (PIN diodes or FET transistors) that make them very attractive for many applications.

2.2 MEMS and Semicondutor Switches:Basic Differences

The basic difference in working principles between semiconductor and series MEMS switches is shown in Fig. 2.1, showing the devices in 'on' and 'off' states. For a semiconductor the figure of merit (FOM), equivalent to the reciprocal of the cut off frequency [20], can be expressed as:

$$FOM\ (semiconductor\ )= CR = \varepsilon_0\varepsilon_r\rho \quad (2.1)$$

where $C = \frac{\varepsilon_o\varepsilon_r d_x d_y}{d_z}$ and $R = \frac{\rho d_z}{d_x d_y}$ represent the capacitance and resistance of a semiconductor volume with dimensions d_x, d_y and d_z respectively. As shown by the above equation the fundamental limit for the microwave switching behaviour is largely determined by the dielectric constant of the material in the off state and by the conductivity in the on-state, independent of the dimensions, which determine the power handling capability of the devices. Using the same criteria for a series MEMS switch with gap height g_0, and the contact film thickness t, resistivity ρ, area A and effective area a_e, the FOM is given by

$$FOM\left(MEMS\quad Series\quad Switch\right)= CR = \frac{\varepsilon_0\rho t}{g_0 a_e} \quad (2.2)$$

Eqn.2.2 further demonstrates that if the switch working principle is based on a physical movement when changing state from the 'off -state' to 'on-state' an "engineer-able" degree of freedom can be introduced into the device. This additional degree of freedom and absence of the semiconducting junctions gives MEMS devices a distinctive advantage in performance as summarized in Table 2.1 [39].

Parameter	RFMEM	PIN	FET
Voltage[V]	20-80	$\pm 3 - 5$	3-5
Current[mA]	0	3-20	0
$C_{up}Series[fF]$	1-6	40-80	70-110
$R_sSeries[\Omega]$	0.5-2	2-4	4-6
Isolation[10-40GHz]	Very heigh	Heigh	Medium
Isolation[60-100GHz]	High	Medium	None
Loss[1-100GHz]	0.05-0.3	0.3-1.2	0.4-2.5
Power handling[W]	< 1	< 10	< 10
Switching time[μs]	1-300	0.001-0.1	0.001-0.1

Table 2.1: Performance comparison between RF MEM switches and solid state switches
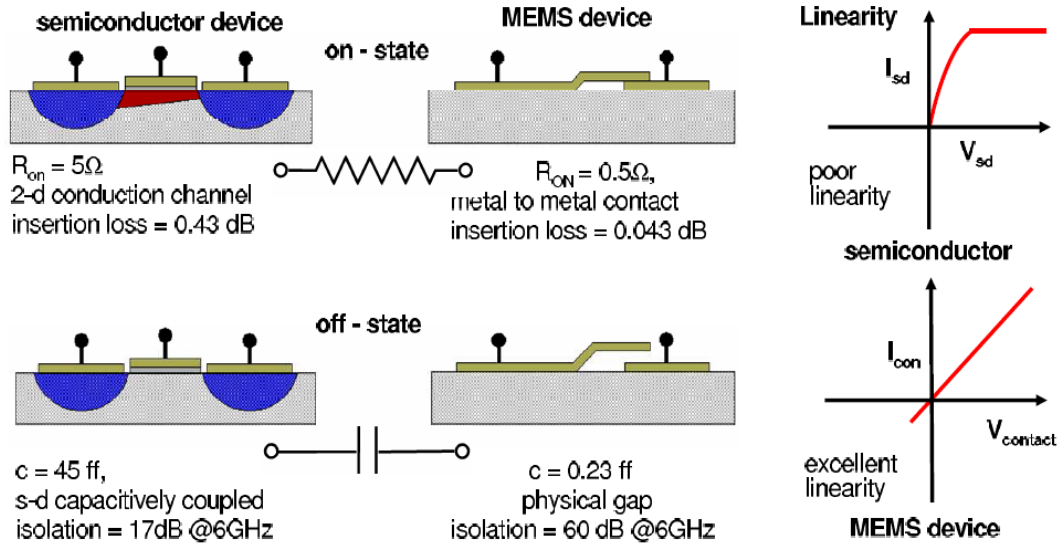
Figure 2.1: Principal differeces between semiconductor and MEMS Switches

2.3 RF MEMS Switches

In comparison to other mature MEMS fields, the radio frequency MEMS are relatively new. The first MEMS switch designed specifically for microwave applications was reported in 1990 [27] RF MEMS devices that serve as fundamental building blocks are: RF MEMS switches or relays,

tuneable capacitors or varactors, high Q inductors, resonators and filters, which can substitute the discrete off-chip counter parts in existing microwave systems[39].

The main advantages of RF MEMS Switches are outlined as below:

1. **Very Low Insertion Loss:**
   Since metals are used for building the transmission lines instead of semiconductors, RF MEMS switches are characterized by very low loss, typically in the order of 0.05 to 0.2 dB at 10 GHz.

2. **Very High Linearity:**
   MEMS switches are very linear devices, which results in a very low intermodulation product. They are about 30-60 dB better than FET switches, PIN diodes or BST varactors [13]. From a system point of view this is one of the most interesting aspects.

3. **Extremely Low Power Consumption:**
   Although a relative high voltage is needed for the electrostatic actuation of the MEMS switches,the associated current flow is very small, leading to very low DC power consumption, this feature makes these devices interesting for applications on satellites and for any type of portable devices.

3. **Very High Isolation:**
   The isolation of MEMS metal-contact switches is based on a gap, in general of several microns filled with air or other inert gases. This provides a very small off-state capacitance (C_{up}), typically in the order of 1-6 fF, which leads to an excellent isolation characteristic which can be up to 40 GHz for a single device, i.e. thousand times better than FET devices.

Actuation method	Power usage	Force Generated	Deflection Range	Speed
Themnal	High	Moderate	Small	ms
Electromagnetic	Medium/high	High	Large	$\mu s/ms$
Electrostatic	Low	Moderate	Moderate	μs

Table 2.2: Qualitative comparison between the different actuation mechanisms

These intrinsic advantages along with the IC-processing compatibility make RF MEMS an enabling technology for low cost and high performance systems in both military and commercial applications such as wide-band tuneable/switchable filters, antenna beam-steering systems, reconfigurable matching networks, reconfigurable array antennas and satellite communications.

2.3.1   Actuation Mechanism

There are many different actuation mechanisms that can be effectively used for RF MEMS switches. The three most used mechanisms are: electrostatic, thermal and electromagnetic actuation. This thesis will focus only on electrostatic actuation because this is the most widely used mechanism and the one which is employed in the most mature RF MEM switch prototypes. The Electrostatic actuation is based on the attractive Coulomb force developing between charges of opposite polarity. This physical effect can be exploited both to induce a vertical movement or an in plane lateral movement. In the first case a parallel plate capacitor configuration is used, while in the second case a comb like structure is used. In both cases relatively high forces can be applied even if medium to high voltages are necessary. Among the appealing features of an electrostatic drive is the low power consumption as power is virtually consumed only during switching. The realization of this type of actuation mechanism is relatively simple and it has been successfully used in many devices, not only in RF MEMS. The

need of high voltages is a potential drawback of this mechanism. This can be the origin of catastrophic device failures and limit their reliability. In table 2.2 a qualitative comparison between different actuation mechanisms for RF MEMS switches is shown [39, 49].

2.3.2 Contact type

In principle two different electric contacts can be realized for RF MEMS switches: the capacitive contact and the metal to metal contact. The capacitive contact is based on a capacitor used to shunt the transmission line to ground. The performance of this contact type is characterized by the capacitance ratio between the up-state (open circuit) and down-state (short-circuit) positions. Typically values are 80-160 depending on the design and the technology. The down-state capacitance is typically in the order of 2-3 pF. This type of contact is suitable for applications in the range of 8 to 100 GHz. In general, it is hard to obtain a large down-state capacitance using nitride or oxide layers, which limits the low-frequency operation of this contact. On the other hand, DC-contact switches with small up-state capacitances (open circuit) can operate from 0.01 to 40GHz, and in some cases up to 60GHz (e.g. the Rockwell Scientific switch has an up-state capacitance of only 1.75 fF and an isolation of 23 dB at 60GHz). In the down-state position (short-circuit), the DC-contact switch becomes a series resistor with a resistance of 0.5-2Ω, depending on the contact metal used [39, 49, 35].

As outlined above from the contact type perspective, there are two types of switches based on MEMS technology: metal contacting or ohmic [55] and capacitive coupling [17]. The metal contacting switches use (Fig.2.2) metal-to-metal direct contact to achieve an ohmic contact between two electrodes. This ohmic contact characteristic allows the device to be suitable for low
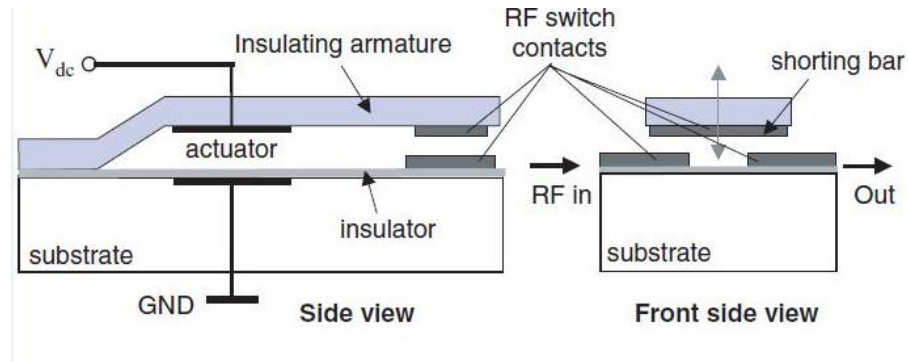
Figure 2.2: Side and front view of a electrostatically actuated cantilever based ohmic series relay. The broad side implementation in CPW can also be configured as a classical bridge type structure.

frequency applications including DC, as well as moderate to high frequency. The capacitive coupling switch,has a thin dielectric film and an air gap between the metallic contact surfaces and the part of the transmission line under the beam called underpass, i.e. the active overlap area. The air gap is electro-mechanically adjusted to achieve a capacitance change between the 'up' and 'down' state.

2.3.3 Series and Shunt Implementation

From the application perspective, the MEMS switches are further classified into other two categories i.e. serial and shunt switches. Although both ohmic and capacitive coupling switches can be used either as serial or shunt switches, ohmic switches are generally used in serial mode, while capacitive coupling switches are preferably employed as shunt switches. The comparison of advantages and disadvantages between the switches is primarily performed with respect to the RF circuit design rather than the MEMS component itself. To further indicate the position of the armature relative to the RF signal line, the switching device can either be configured as broadside or inline [49]. In an inline switching device, the armature

for instance a bridge is an integral part of the transmission line [49]. For a broadside switching device the long side of the armature is not inline but typically positioned perpendicular to the signal line[49]. In addition to the above mentioned basic configurations which lead to different RF MEMS switching configurations , a multitude of actuation mechanisms can be implemented leading to tens of different configurations. Two types of electrostatically actuated switching devices stand out because of their compatibility with the IC fabrication process and easy implementation in CPW or micro-strip line configurations. These are the capacitive shunt switch and the ohmic series relay. According to the two principal contact types RF MEMS switches come in two configurations: metal-contact and capacitive-contact. Fig 2.3 shows two metal-contact series switches developed by Analog Devices [60] and Lincoln Laboratory [12] respectively with their equivalent circuit model. Fig. 2.4 presents a capacitive shunt switch developed by Raytheon [19].
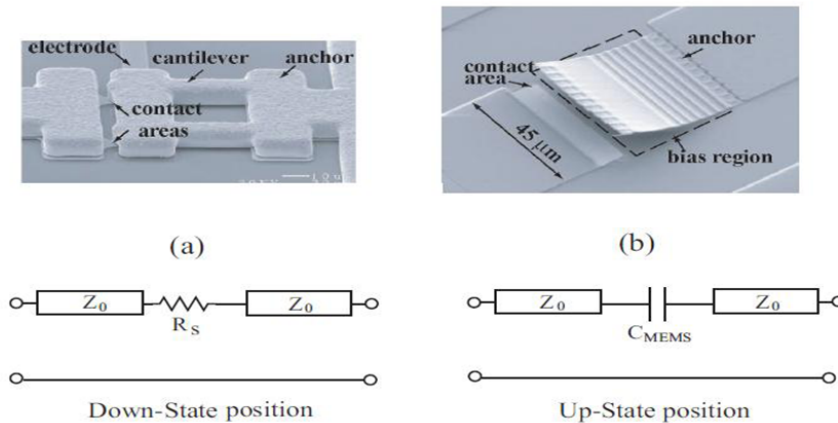
Figure 2.3: Series metal contact switches developed by a) Analog devices b) Lincoln laboratory with their corresponding equation circuit.
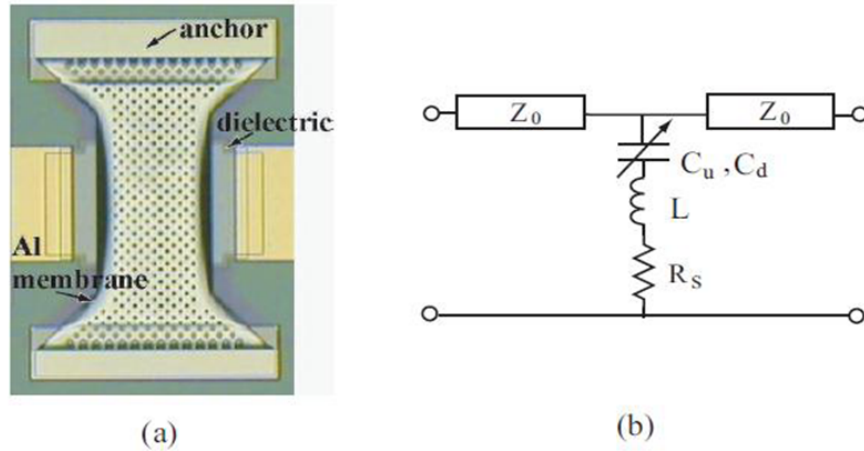
Figure 2.4: Shunt capacitive switch developed by Raytheon a) top view b) cor-responding electrical model.

2.3.4 RF MEMS Tuneable Capacitors

A tuneable capacitor, also referred to as 'varactor', is a capacitor where the capacitance can be tuned or varied by electrical means, e.g. by a DC (tuning) voltage, which makes the capacitance voltage dependent, $C=C(V)$. The RF tuneable capacitors find applications in tuneable matching networks, tuneable filters, phase shifters, and as frequency controlling elements for instance in LC tank of a low noise VCO. Semi conducutor on-chip varactor diodes or MOS capacitors, suffer from excessive series resistance and non-linearity [43]. RF MEMS varactors on the other hand use highly conducting thick metal layers, with air as dielectric, thus offering substantial improvement over conventional on-chip varactor diodes in terms of power loss. In addition, the RF MEMS capacitors have excellent linearity, wide tuning range and ability to separate the control circuitry from the signal circuit, which greatly simplifies the overall design.

The principle of gap-tuning MEMS capacitor controlled by electrostatic means is similar to RF MEMS switches and is shown in Fig. 2.5. The top plate is suspended with a support beam of spring constant k, while the

bottom plate is fixed. An applied DC bias reduces the air gap, thus increasing the capacitance. The thin dielectric film covering the bottom plate and the overlap area determines the down capacitance. The suspensions as well as the plates are fabricated from metal to obtain a low parasitic series resistance and high Q [56].

2.3.5   RF MEMS Inductors

The MEMS inductor, another outstanding example of RF MEMS, needs a mention, because of the superior performance and ubiquitous presence in RF communication designs. The stringent phase noise requirements in applications like voltage controlled oscillators (VCO) need inductors with quality factor $Q > 30$. On-chip inductors implemented in CMOS or bipolar technologies having $Q < 10$ make off-chip, discrete inductors the only viable choice. The key parameters that characterize the performance of inductors are the quality factor Q, the inductance L and the self-resonant frequency (SRF) at which the device transforms from inductive to capacitive characteristics. MEMS technology improves the on-chip inductor performance by etching away the lossy substrate from underneath the inductor spiral, resulting in a membrane-supported inductor as shown in Fig. 2.6. Reduced substrate losses and reduced capacitive coupling to the substrate lead to higher Q and increased SRF. Another approach to build floating or levitated 'onchip' inductors using an IC compatible process is to pattern the spiral in thick electroplated metal like Cu, Al or Au over a sacrificial dielectric or photo-resist layer. Inductors ranging from 1.5nH to 18nH with Q from 30 up to 80 at 2GHz have been fabricated and reported [1]. High Q inductors have also been fabricated using low loss, high resistivity substrates such as Si or Alumina without the need to resort to levitated or out-of-plane configurations with measured Q values up to 107 [7].
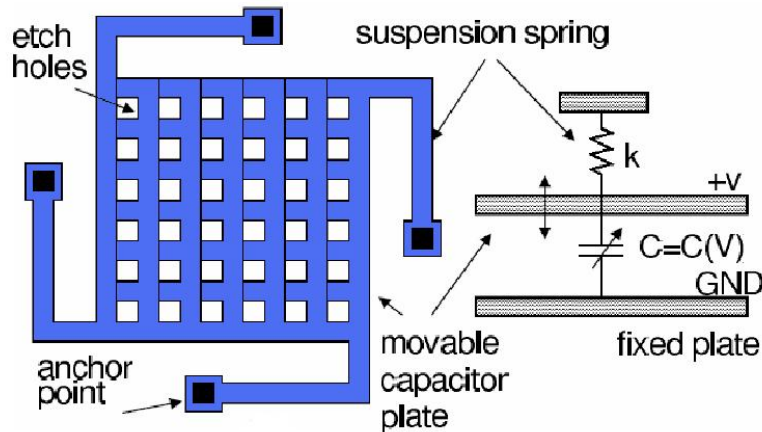
Figure 2.5: Schematic top view of the tuneable capacitor, the whole structure is suspended above the actuation plates by four anchor posts, represented by spring constant k.

2.4 RF MEMS Applications

Compared to a semiconductor switch (FET or PIN diode) an electrome-chanical switch has far less series resistance, resulting in much lower loss and less power dissipation. The small mass of MEMS switch actuators require very little operating power and these advantages make RF MEMS switches suitable for many applications. In the following paragraphs some of them are shortly listed.

2.4.1 Switching Networks

Switching networks are part of virtually every communication system and include SPNT switches for filter or amplifier selection, NxN switching ma-trices and in general SPDT and DPDT routing switches. Switch matrices
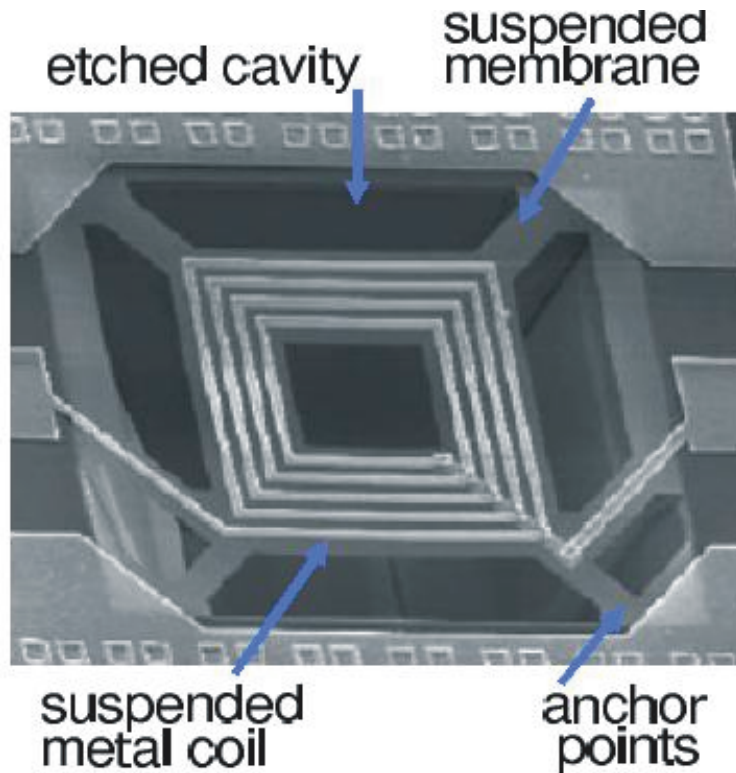
Figure 2.6: Bulk micromachined inductor with metal coil suspended over a cavity [56]

in satellite systems are built using coaxial switches, while base station systems are implemented using PIN diodes except for the power amplifiers. PIN diodes require additional amplifier stages to compensate for the losses introduced by the switching network. Coaxial switches have excellent overall performance, but they are heavy and costly.

2.4.2 Portable Wireless Systems

In order to integrate the whole front end design of a wireless telephone system on a chip, the main bottleneck are not the switches, but the high Q filters and diplexers and also the crystal references [5]. Filters are currently being addressed using FBAR technology. Using RF MEMS devices

(switches, varactors and inductors) it may be possible in the near future to eliminate the off chip inductors in the oscillator circuit or integrate a tuneable filter directly on the silicon chip.

2.4.3 Phased Arrays

RF MEMS switches are best suited to those communication systems, e.g. phased arrays, that use large numbers of switching devices. The average loss of the state-of-the-art 3-bit MEMS phase shifter shows an improvement of more than 3dB over comparable GaAs FET devices [6]. This translates to 6 to 8 dB improvement in a radar or a two-way telecommunication system. The improvement is quite significant in Ka, V or W-band systems. With MEMS switches it is therefore possible to eliminate a few amplifier stages in T/R chain resulting in an overall 20-100mW DC power reduction per element at X to V-band frequencies.

2.5 Overview on Current RF MEMS Technologies

In the last ten years quite a number of companies and academic institutions have developed suitable MEMS technologies for the fabrication of RF MEMS switches. In this section some of them like those from Radant, Teravicta and FBK (Foundazione Bruno Kessler) are shortly outlined.

2.5.1 The TeraVicta RF MEMS Technology

TeraVicta Technologies provides next-generation radio frequency components and module solutions based on proprietary MEMS technology. Teravicta's RF MEMS switch-based products provide the ultra low loss, broadband performance and low power consumption necessary for superior multi-

band/mode cellular handsets, reconfigurable radios and smart antennas. Applications for TeraVicta's products include cellular phones, wireless LAN's, fixed broadband wireless, cellular phone base stations, automated test equipment, satellite and military communications and radar systems. Founded in July 2000, TeraVicta Technologies is a Texas based company that has developed breakthrough semiconductor components that are capable to manage radiofrequency signals used by leading-edge electronic products from automatic test equipment to wireless handsets. The company's products are based on next generation MEMS technology that uses semiconductor micro-fabrication techniques to build miniature components that switch, route and manage critical RF signals. This allows TeraVicta to integrate RF switches and other advanced components at the chip level, reducing size and cost while improving performance [54].

2.5.2 The Radant RF MEMS Technology

Radant MEMS has been developing and manufacturing devices since 1999. Radant RF MEMS switches and assemblies have been developed and are suitable for many government and commercial applications including radars, telecommunication, phase shifters, cellular phones, satellites, automatic test equipment, wireless LAN and many others. Radant MEMS electro-statically actuated micro switches have a demonstrated lifetime of over 100 billion switching cycles. This industry-leading achievement in reliability now makes RF MEMS switches from Radant MEMS an attractive alternative to other mechanical and solid-state switches [43]. Radant MEMS switches are an attractive alternative to solid state and electromagnetic relay switches also because they offer several additional advantages. They reduce costs and increase application performance like low power consumption, long life cycle (100 billion cycles), significant form factor reduction, improved RF performance, low loss, high -isolation and an extreme lin-

earity. The RF MEMS microswitches from Radant are 3 terminal devices that employ a cantilever beam and are fabricated using an all-metal surface micromachining process on high-resistive silicon. They operate in a hermetic environment obtained through wafer level packaging process based on a wafer bonding process. This wafer packaging technology is more cost effective than either custom or ceramic packaging. It also provides a more direct connection to the customer's system, thereby reducing complexity and increasing reliability[53].

2.5.3 The FBK RF MEMS Technology

FBK developed a process that is optimized for the fabrication of RF MEMS switches on a high resistivity silicon substrate. The FBK switch process makes use of 8 masks. The process starts with the growth of the field oxide on the wafer. Then, the polysilicon layer is deposited, doped with Boron and covered with a thin Tetraethylorthosilane (TEOS) oxide. After the opening of the via's to the polysilicon, the multimetal layer is deposited and patterned on the wafer. The metal is covered with a thin low temperature oxide (LTO), which is removed, where necessary, for the realization of electrical contacts. The gold floating metal is then deposited and patterned. At this point, a 3 μm thick photoresist is spin-coated on the surface, which serves as a sacrificial layer for the creation of the suspended structures. The photoresist is post-baked at high temperature, in order to round the edges of the photoresist structures and to avoid further deformation during subsequent high temperature steps. The seed layer for the electroplating of the suspended structures and other thick metal parts is then evaporated on the substrate. Evaporation does not guarantee a good coverage of steep edges. This renders the removal of sharp edges from the wafer surface necessary to ensure a complete coverage of the seed layer and thus electrical continuity during the electroplating steps. Afterward, gold

is electroplated on the wafer in two steps with different thicknesses: a first layer of 2 μm, called BRIDGE layer, and a second layer of around 3 μm, called CPW layer. Areas on which the gold has to be electroplated are defined with a photoresist-masking layer, with a thickness higher than the layer to grow. After the electroplating steps, the wafer undergoes a temperature treatment, whose main function is to improve the adhesion of the gold to the wafer. This is especially important for wire bonding process. The suspended structures are then released by dry etching of the spacer with oxygen plasma. The most critical part of the process is the creation of stress-free suspended structures. When thin films are deposited on a sacrificial layer at a temperature lower than its flow temperature, then intrinsic stresses develop in the film-sacrificial layer stack. Both in-plane stress and stress gradients can arise. These stresses not only modify the mechanical behaviour of the materials, but can also cause out of plane bending of the suspended structures after their release. The entity of the effect mainly depends on the temperature treatment which the wafer is exposed to, as well as on the employed materials. In the presented process, the annealing of the wafer after electroplating leads to an in-plane tensile stress in the gold layer. In the past, the diffusion of the seed layer into the electroplated membrane also led to a stress gradient in the thickness of the suspended gold layer. The thicknesses of the thin films used in the seed layer were therefore optimized in order to minimize the effects of this phenomenon. A more detailed process description is given in [28]. The FBK process can be summarized in six phases (Figure 2.7)

I) growth of 1000 nm of insulator oxide, deposition of 630 nm of polysilicon, Boron implantation, defi nition of polysilicon, Boron diffusion at $925°C$, deposition of 300 nm of TEOS and opening of the con tacts.

II) deposition and definition of metal alloy Ti/TiN/Al/Ti/TiN, respectively of 30/50/410/60/80 nm (underpass).

III) deposition of 100 nm of LPCVD oxide (or PECVD Nitride) and VIA definition.

IV) deposition and definition of the spacer based on 3 μm of resist.

V) seed layer of Cr/Au (10/150 nm respectively), area definition of the first electro-deposition and first electro-deposition of Au (1.5 μm for pads and bridges).second electro-deposition of Au 3.5 μm for thick bridges and CPW, seed layer removal.

2.6 Open issues in the Field of RF Switches

As mentioned earlier RF MEMS switches have some advantages like low insertion loss, high isolation, excellent linearity etc. but they suffer also from some disadvantages as there are high switching times, lack of reliability and not yet addressed packaging issues, that significantly limit their practical use at the moment.

2.6.1 Switching Time

Regarding the performance characteristics one of the main disadvantages of RF MEMS switches is their high switching time, which makes them unsuitable for many applications like mobile phones and communication systems, where high commutation speeds are crucial. Even if the intrinsic mechanical limitations will prevent the use of these devices in applications
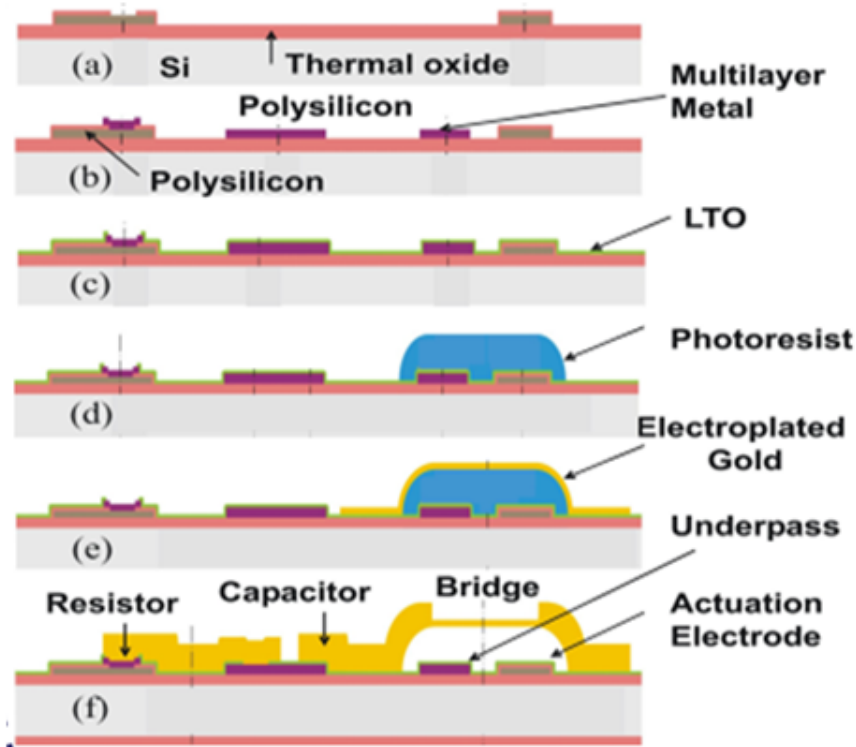
Figure 2.7: Summary of the FBK Process

like active radars, an improvement of the switching speed of an order of magnitude would make them interesting for those applications where the requested commutation speed is high, but not in the nanosecond range. Due to the essentially mechanical nature of RF MEMS switches, the switching time is mainly affected by the mechanical parameters of the device, i.e. the mass and stiffness of the mobile parts and the flow of the air (or gas) surrounding the structure. Mass and stiffness depend mostly on the material used for the fabrication and geometrical parameters like the thickness of the layers. The dynamics of the airflow and therefore the damping characteristics of the structure are strongly influenced by the number and dimensions of the air holes in the structure and the size of the gap between the mobile part and the substrate. The gap influences the switching time

also by cinematic aspects (a higher gap simply requires a longer time for closure) as well as the voltage necessary for the actuation. Also the applied voltage itself has an effect on the switching speed. Finally the packaging of the device can influence its switching characteristics in an indirect way by controlling the atmosphere in which the device operates. Due to the complex relationships between these parameters a good understanding of the static and dynamic behaviour can be helpful in the design of a switch with fast performance.

2.6.2 Reliability

Emerging and future autonomous wireless communication systems require highly reliable electronic components with very low power consumption. Micromachined devices represent a promising technology to meet this demand. RF MEMS switches are specific micromechanical devices designed to operate at RF-to-millimeter-wave frequencies (0.1 to 100 GHz). Such RF switches have been demonstrated with low loss, low power consumption, low distortion, and higher off state isolation as compared to PIN diodes or field effect transistors. However, before such switches can be used in commercial or spatial applications, they must demonstrate the ability to switch reliably over billions of cycles. Alternatively, as in the case of redundancy switches, they should maintain their electrical and RF performances for a very long time and guarantee the switch actuation even after years of storage in harsh environment. In addition the presence of a mechanical contact introduces a whole new class of reliability issues related to both mechanical and electrical phenomena [24, 61]. Cycled mechanical deformations and steady-state vibrations introduce new stress mechanisms on the structural parts of these devices. Mechanical relaxation of residual material stress, plastic deformations under large signal regime, creep formations and fatigue can all impair the stability of electro-mechanical

device behaviour and eventually cause mechanical failure of the device. Finally other surface effects such as oxidation or absorption can also result in changes of effective mass or stress of a moving or vibrating structure, causing stability issues and device failures. The main reliability aspects of RF MEMS switches so far identified can be grouped in three major classes: mechanical, electrical and environmental phenomena, as discussed in some more detail in chapter 3.

Chapter 3

Basic Electro-mechanic Aspects

3.1 Introduction

There are several different aspects that characterize micromachines and microactuators. An important one is the adopted fabrication technique in terms of employed materials, e.g. polysilicon micromachining, silicon bulk micromachining or others. The fabrication techniques contribute in determining the mechanical properties and the type of structure that can be build. Another very important aspect, in some way more general, is the actuation principle, which can be based on electrostatic, magnetostatic, piezoelectric and other mechanisms. As stated earlier most of the MEMS devices are actuated using electrostatic forces because this provides low power consumption and the realization process is compatible with IC fabrication technology. Nevertheless electrostatic actuation has some limitations due to its essential non linear nature. Two basic structures are possible, parallel and lateral plate actuators. Both types are commonly used. Here after a description of these basic configurations is given together with the basic equations describing their electromechanical behaviour and the description of the most important mechanical parameters affecting the behaviour of these structures.

3.2 Mechanical Equations of Motion

Micromechanical structures can be divided into discrete elements that are modelled using rigid body dynamics . Finite-element analysis is used to determine the mechanical modes within the bandwidth of the feedback and external forces, for a first order analysis a mechanical structure can be simply divided into discrete elements, each of which can be modelled by using rigid-body dynamics. Some structural elements can be modelled simply as rigid body masses, while other models may include the effects of bending, torsion, axial and shear forces. In general a mechanical system with n degrees of freedom can be described in terms of n generalized coordinates, $q_1, q_2..., q_n$ and time t. A general method of determining the equation of motion involves the use of Lagrange's Equation [25]:

$$\frac{d}{dt}\left(\frac{\partial L}{\partial q'_i}\right) - \frac{\partial L}{\partial q_i} = Q_{nc,i}, i = 1, ..., n \tag{3.1}$$

 where L = T - V is the Lagrangian operator, T is the total kinetic energy of the system and V is the total potential energy of the system arising from the conservative forces. Non-conservative forces such as dissipative forces, are lumped in the terms $Q_{nc,i}$. If only viscous damping terms (damping proportional to velocity) are present then the Lagrange's equation can be written as

$$\frac{d}{dt}\left(\frac{\partial L}{\partial q'_i}\right) - \frac{\partial L}{\partial q_i} + \frac{\partial F}{\partial q_i} = Q_{ext,i}, i = 1, ..., n \tag{3.2}$$

where F is the Raleigh dissipation function and Q_{ext}, i is an external generalized force associated with the coordinate q_i. In general the kinetic energy, potential energy and the dissipation function have the forms

$$T = \frac{1}{2}\sum_{i=1}^{n}.\sum_{j=1}^{n}m_{ij}q_i'q_j' \tag{3.3}$$

34
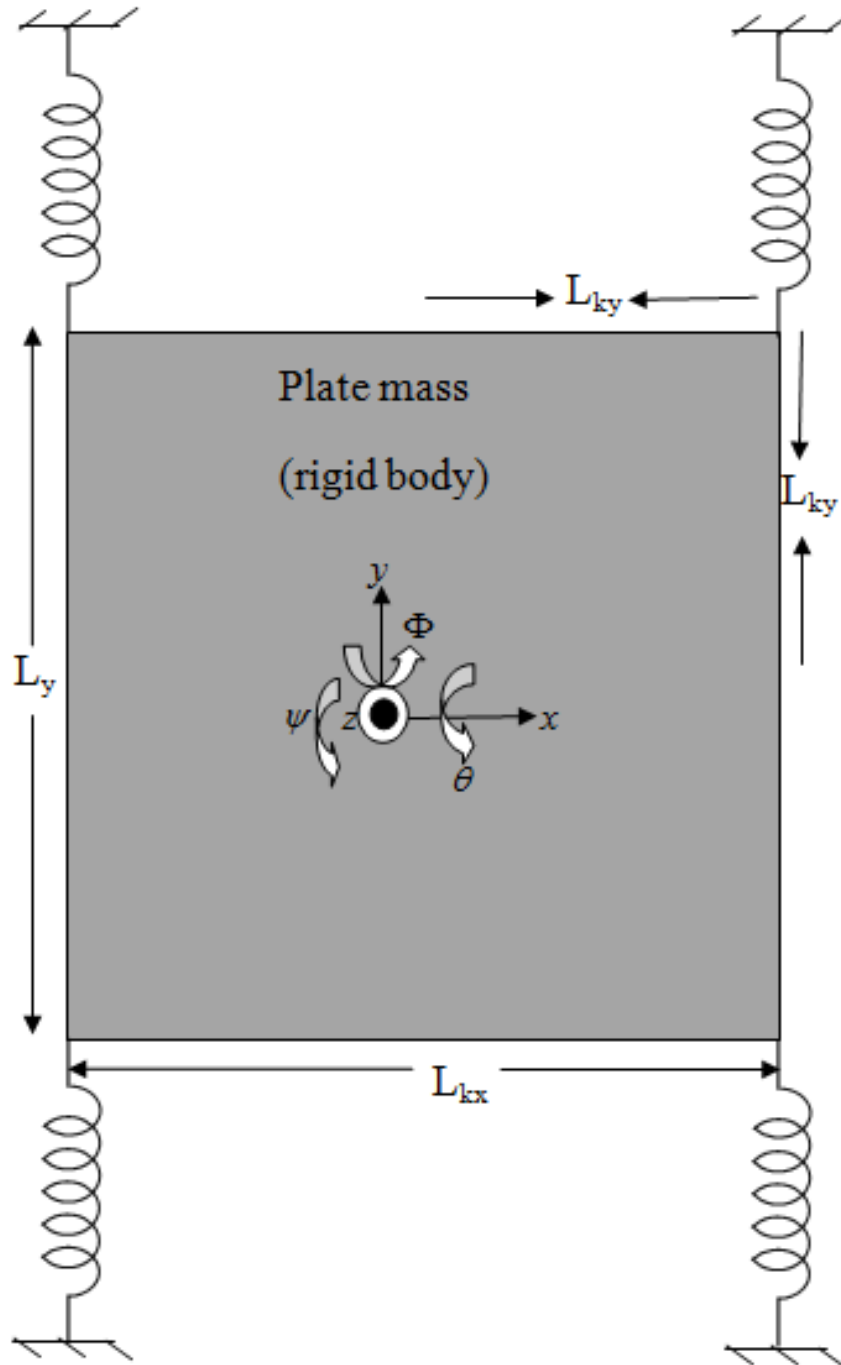
Figure 3.1: Schematic of a rigid plate with dimensions L_x, L_y, springs are attached at distances L_{kx} and L_{ky} along the x-axis and y-axis, respectively from the centroid of the plate.

$$V = \frac{1}{2}\sum_{i=1}^{n} \cdot \sum_{j=1}^{n} k_{ij} q_i q_j \tag{3.4}$$

$$F = \frac{1}{2}\sum_{i=1}^{n} \cdot \sum_{j=1}^{n} B_{ij} q_i' q_j' \tag{3.5}$$

where m_{ij}, k_{ij} and B_{ij} are the inertia, stiffness and damping coefficients respectively.

In this general discussion we apply Lagrange's equation to a rigid rectangular plate suspended by four springs located at the plate's corners shown by Fig.3.1. The Cartesian coordinates x, y, z and three angles of rotation θ, and φ and ψ are chosen to be the generalized coordinates with the plate centre as the origin. However, in specific cases such as bridges and cantilevers, the z-axis origin is chosen to be the substrate below the anchor points. In such case the variable represents the vertical displacement of the plate from its rest (zero mechanical potential) position. The potential energy stored in the springs is determined by the contributions of each spring. Making small angle approximations, we find

$$V = 2\left(k_x x^2 + k_y y^2 + k_z z^2 + k_z L_{ky}{}^2\theta^2 + k_z L_{kx}{}^2\phi^2 + k_y l_{kx}{}^2\psi^2\right) \tag{3.6}$$

where k_x, k_y and k_z are the spring constants in the x, y and z directions respectively. The dimensions L_{kx} and L_{ky} are the distances along the x and y axis from the centroid of the plate to the springs, the springs in Fig.3.1 are located at $L_{kx} = \frac{L_x}{2}$ and $L_{ky} = \frac{L_y}{2}$. The spring force is assumed to vary linearly with the displacement, however nonlinear spring forces can be modelled by introducing into Eqn.3.6 stiffness coefficients that are functions of the position. Assuming massless springs the kinetic energy T is:

$$T = \frac{1}{2}(mx' + my' + mz' + I_\theta\theta' + I_\phi\phi'^2 + I_\psi\psi'^2) \tag{3.7}$$

36

where m is the plate mass and the mass moments of inertia of the plate are:

$$I_\theta = \frac{m}{12}L^2 y \tag{3.8}$$

$$I_\phi = \frac{m}{12}L^2 y \tag{3.9}$$

$$I_\psi = \frac{m}{12}(L_x{}^2 + L_y{}^2) \tag{3.10}$$

The viscous damping of the plate can be expressed by the damping function as:

$$F = \frac{1}{2}(B_x{}^2 + B_y{}^2 + B_z{}^2 + B_\theta\theta^2 + B_\phi\phi^2 + B_\psi\psi^2) \tag{3.11}$$

where $B_x, B_y, B_z, B_\theta, B_\phi, B_\psi$ are the damping coefficients of the six modes. The expression for kinetic energy, potential energy and the dissipation function of the mass-spring-damper system are substituted into Equation (3.1) and then solved for each of the six coordinates resulting in the following equations of motion

$$F_x = mx^{''} + B_x x^{'} + k_x x \tag{3.12}$$

$$F_y = my^{''} + B_y x^{'} + k_y y \tag{3.13}$$

$$F_z = mz^{''} + B_z z^{'} + k_z z \tag{3.14}$$

$$\tau_\theta = I_\theta\theta^{''} + B_\theta\theta^{''} + K_z L_{ky}{}^2\theta \tag{3.15}$$

$$\tau_\phi = I_\phi\phi^{''} + B_\phi\phi^{'} + K_z L_{kx}{}^2\phi \tag{3.16}$$

$$\tau_\psi = I_\psi\psi^{''} + B_\psi\psi^{'} + K_y L_{kx}{}^2\psi \tag{3.17}$$

where $F_x, F_y, F_z, \tau_\theta, \tau_\phi, \tau_\psi$ are the external forces and torques that act on the plate. Values of the stiffness and damping coefficients can be determined numerically using finite element analysis or approximated by analytical formulas, as discussed in the following sections. In general most of the simulations and modelling described in this thesis involves only the

vertical motion of the suspended plate. Therefore, reference is made to the vertical equations of motion, Eqn. (3.14) - (3.16), which can be expressed in the alternative form:

$$F_z = m(z'' + 2\zeta_z w_z z' + w_z{}^2 z^2) \tag{3.18}$$

$$\tau_\theta = I_\theta(\theta'' + 2\zeta_\theta w_\theta \theta' + w_\theta{}^2 \theta^2) \tag{3.19}$$

$$\tau_\theta = I_\theta(\theta'' + 2_\theta w_\theta \theta' + w_\phi{}^2 \phi^2) \tag{3.20}$$

where, w_z, w_θ and w_Φ are the resonant frequencies and ζ_z, ζ_θ and ζ_ϕ the dimensionless damping factors of the z,θ, ϕ and modes, respectively.
In general, the resonant frequency ω_i, and damping factor ζ_i of the mode i are given by:

$$\zeta_i = \frac{B_i}{2\sqrt{k_i m_i}} \tag{3.21}$$

$$\omega_i = \sqrt{\frac{k_i}{m}} \tag{3.22}$$

where k_i is the stiffness coefficient and mi is the inertia coefficient (mass for translational modes or moment of inertia for rotational modes) of mode i. Effects of the spring mass can be included by introducing effective inertia coefficients to adjust the resonant frequency.

3.3   Squeeze-Film Damping

Viscous air damping is the dominant dissipation mechanism for microstructures operating at atmospheric pressure. Squeeze film damping, illustrated in Fig 3.2, arises from the vertical motion of the structure, which creates a pressure buildup in the thin film of air trapped between the moving plate and the substrate. Due to the inertia of the gas flow, reaction forces are generated on the moving part, which depend on the velocity of the moving part. A more detailed description of the mechanism can be found in

[15, 26], while in the next paragraphs some aspects relevant to the work of this thesis are summarized.
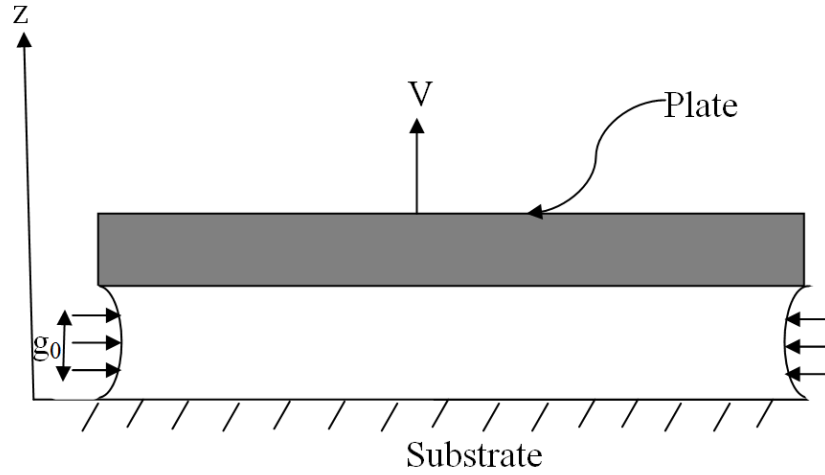
Figure 3.2: Cross section of the plate with an air gap g_0 above the substrate illustrating how squeeze film damping arises from the vertical motion of the plate with velocity v, The pressure induced produces the force which is proportional with velocity.

3.3.1 Viscous Flow

Continuum fluid mechanics can be applied to analyze squeeze-film damping if the air gap is much larger than the mean free path, of the air molecules. The mean free path of a gas is expressed as:

$$\lambda = \frac{1}{\sqrt{2}\pi d_0^2 n} \tag{3.23}$$

Where πd_0^2 is the collision cross section of the gas molecules and n is the molecular density, which for an ideal gas is given by $n = P/(k_B T)$, where P is the pressure of the squeeze film, k_B is the Boltzmann's constant and T is the absolute temperature. For air at atmospheric pressure and T = 300 K, the mean free path is $\sim 65 nm$. The viscous flow regime is described
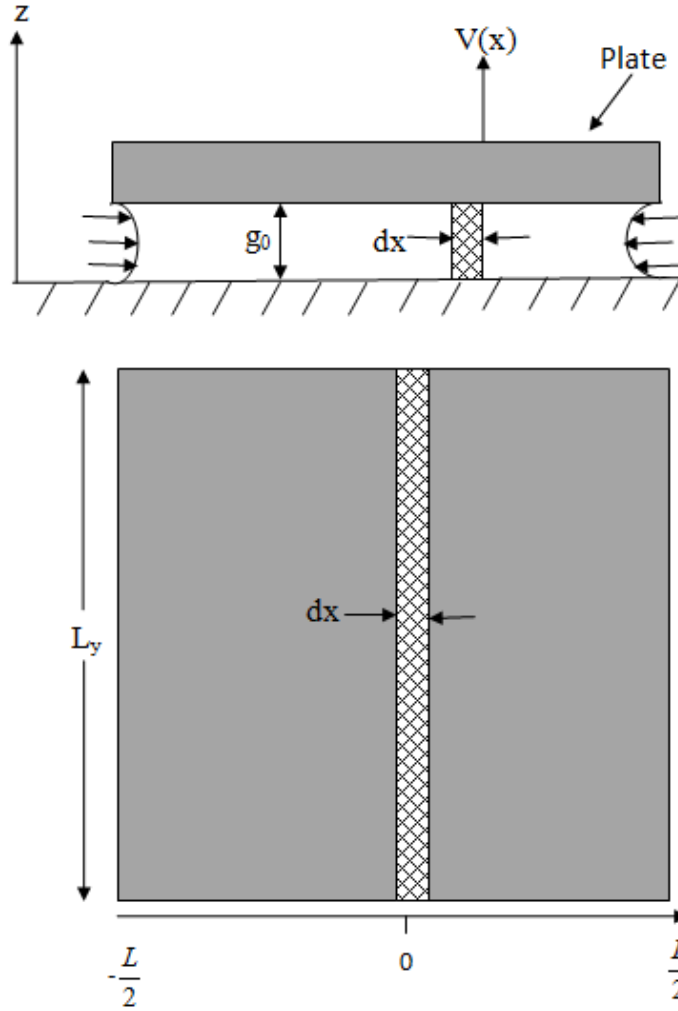
Figure 3.3: Schematic cross section of a plate above the wafer illustrating the squeeze-film damping arising from the vertical motion of the plate with velocity v. Pressure in the squeezed film produces a force, proportional to velocity v.

by the Navier -Stokes equation[45] which under several assumption can be reduced to the following expression as described in the next paragraph:

$$\frac{\partial^2 p}{\partial x^2} + \frac{\partial^2 p}{\partial y^2} = \frac{12\mu\partial(\Delta z)}{g_0{}^3\partial t} \tag{3.24}$$

where p is the pressure of the squeeze film, μ is the viscosity of air, g_0 is the air gap height and $\triangle z$ is the plate displacement. The above equation is valid if the squeeze film is isothermal, small pressure variations and small

displacements with small velocity are considered. Air velocity in the gap can be considered small if the Reynolds number, R_e, is much less than 1, where $R_e = \rho v g_0 / \mu$ and ρ is the density of the air .

3.3.2 One-dimensional Analysis

Let's now consider the squeeze film damping of the plate shown in Figure 3.3, where the plate length L_y in the y direction is much larger than the length L_x in the x direction. In this case the squeeze film damping is modelled with one-dimensional version of equation (3.24).

$$\frac{\partial^2 p}{\partial x^2} = \frac{12 \mu v}{g_0{}^3} \tag{3.25}$$

Double integration of Equation (3.25) and application of the pressure boundary conditions at the edges of the plate gives:

$$\Delta p = \frac{6 \mu v}{g_0{}^3} (x^2 - \frac{L x^2}{4}) \tag{3.26}$$

where Δp is the pressure difference with respect to the ambient pressure. The average pressure difference across the plate is $\frac{\mu L_x v}{g_0{}^3}$ and the total damping force exerted on the plate is:

$$F_B = - \left(\frac{\mu L_y L_x{}^3}{g_0} \right) v \tag{3.27}$$

More in general the squeeze film damping coefficient for a rectangular plate is:

$$B_z = k_{BZ} \left(\frac{L_x}{L_y} \right) \frac{\mu L_y L_x{}^3}{g_0{}^3} \tag{3.28}$$

where $k_{BZ} \left(\frac{L_x}{L_y} \right)$ is introduced to account for the finite plate length. By comparison with Equation 3.27 the case of a very long plate length corresponds to $k_{BZ} = 1$. As an example of the two dimensional flow problem for other geometries let's consider a square plate $L_x = L_y$. In this case it can be shown that k_{BZ} is approximately 0.42.

3.3.3   Damping of the Rotational Mode

The one dimensional analysis of the preceding section can be repeated for the rotational mode shown in fig 3.4 where again $L_y \gg L_x$. In this case the velocity is a function of the distance x from the plate centroid. Substituting for the velocity we can write Equation (3.26) as :

$$\frac{\partial P}{\partial x^2} = -\frac{12\mu\phi' x}{g_0{}^3} \tag{3.29}$$

where small angular displacement are assumed. Equation (3.26) is then integrated twice to obtain the differential pressure:

$$P = \frac{2\mu\phi'}{g_0{}^3}\left(\frac{Lx^2}{4} - x^2\right)x \tag{3.30}$$

The total moment generated by the damping is:

$$M_B = -L_y \int_{-\frac{Lx}{2}}^{\frac{Lx}{2}} p_x d_x = -\frac{L_y L_x{}^5 \mu}{60 g_0{}^3}\Phi' \tag{3.31}$$

We can now define the rotational mode squeeze film damping coefficient B_ϕ in an analogue manner to the vertical mode coefficient damping. Thus for the rectangular plate we have:

$$B_\phi = k_{B_\phi}\left(\frac{L_x}{L_y}\right)\frac{\mu L_y L_x{}^5}{g_0{}^3} = K_{B\phi}\left(\frac{L_x}{L_y}\right)B_z L_x{}^2 \tag{3.32}$$

where $k_{B\phi}\left(\frac{L_x}{L_y}\right)$ is the two dimensional form factor. For $L_y \gg L_x$, $K_{B\phi}$ is 0.017. A similar damping coefficient $K_{b\phi}$ can be defined for the rotational mode about the x axis where:

$$B_\theta = k_{B\theta}\left(\frac{L_x}{L_y}\right)B_z L_y{}^2 \tag{3.33}$$

The corresponding damping factors for rotational mode are:

$$\zeta_\theta = \frac{B_\theta}{2\sqrt{I_\theta k_z L_{ky}{}^2}} = \sqrt{12 k_B}\left(\frac{L_y}{L_{ky}}\right)\zeta_z \tag{3.34}$$
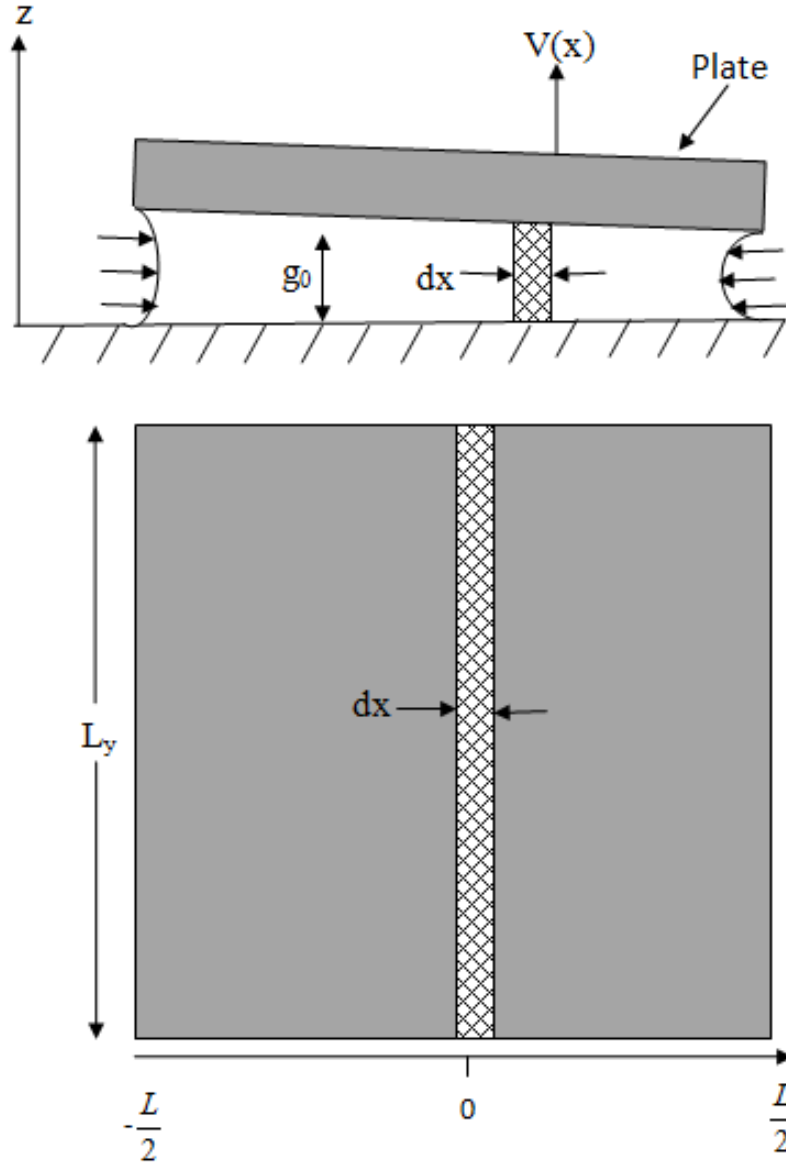
Figure 3.4: Schematic of the plate for one dimensional analysis of squeeze film damping of the rotational mode about the y axis .

$$\zeta_\theta = \frac{B_\theta}{2\sqrt{I_\theta k_z L_{kx}}^2} = \sqrt{12k_B}\left(\frac{L_x}{L_{kx}}\right)\zeta_z \qquad (3.35)$$

where the constant k_{B0} describes the springs connected to the plate's corner. For the solid plate with springs attached at the corners, the rotational mode damping is around 17 times smaller than vertical mode damping.

From a more complex analysis not reported here it can be shown that for the practical case where a square perforated plate with many holes is substituted for the continuous plate assumed up to now the rotational mode damping is found approximately two times smaller than the vertical mode damping.

3.4 Spring Constants for Simple Beam Geometries

Cantilever, guided-end and fixed-fixed beams are shown in Fig.3.5. We consider that a concentrated force $F(N)$ is applied to the free end of the cantilever beam (a), to the free end of the guided-end beam (b) and to the centre of the fixed-fixed beam in (c), while a uniform distributed load $f[\frac{N}{M}]$ (force per unit length) is applied to the surface of each beam in Fig.3.5 $(d - f)$. In these cases the axial displacement is derived from Hooke's law: $stress = E$ strain, where E is the Young Modulus of elasticity. The displacement equations for the different cases are summarized in Table 3.1, assuming a beam with small angles of rotation, no axial loading and no shear deformation [57]. The beams with rectangular cross section have width w, thickness t and length L. For cases where concentrated loads are applied to the beam, linear spring constants are defined as a measure of the beam's stiffness:

$$k_x = \frac{F_x}{x}; k_y = \frac{F_y}{y}; k_z = \frac{F_z}{z} \tag{3.36}$$

3.4.1 Nonlinear Effects

The equations for the beam deflection listed in Table 3.1, are derived from differential equations assuming small deflections and small angles of rotation. A precise solution for a cantilever beam can be found in [25] where
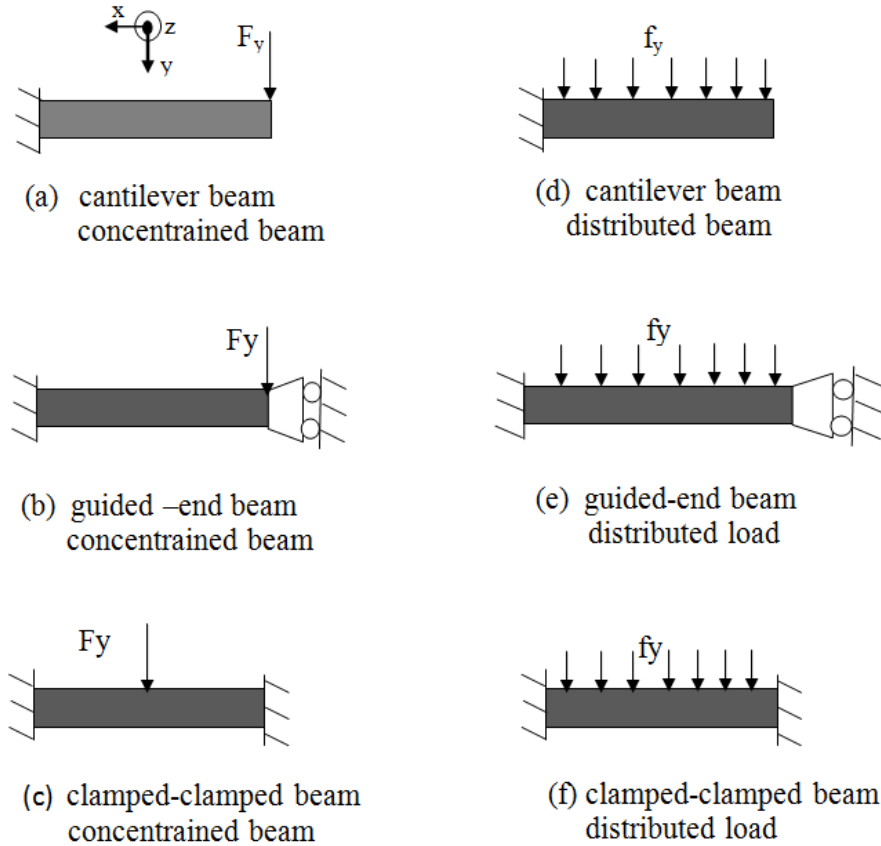
Figure 3.5: Various beam geometries with concentrated load, F or distributed load f. In all cases only the y-component is considered [28].

it is compared with the approximate theory based on the assumption of small deflections.

Normally the model based on small deflections is 10% in error for deflections greater than 30% of the beam lenght. Shear deformation, which is neglected in Table 3.1, is small if:

$$w \ll \sqrt{\frac{4}{3(1+\nu)}} L \approx L \tag{3.37}$$

where ν is the Poisson's ratio. Typical values for Au is 0.42 and 0.3 for polysilicon [25]. Most mechanical mechanical structures undergoing flexure are long and narrow, thereby satisfying Eqn.3.26. If axial ten-

Cantilever	Guided-End	Fixed-Fixed
$x = \dfrac{F_x L}{Ehw}$	$x = \dfrac{F_x L}{Ehw}$	$x = \dfrac{F_x L}{4Ehw}$
$y = \dfrac{4F_y l^3}{Ehw^3}$	$y = \dfrac{F_y}{E_h}\dfrac{l^3}{w^3}$	$y = \dfrac{1}{16}\dfrac{F_y}{E_h}\dfrac{l^3}{w^3}$
$z = 4\dfrac{F_z}{Ew}\dfrac{l^3}{h^3}$	$z = \dfrac{F_z}{Ew}\dfrac{l^3}{h^3}$	$z = \dfrac{1}{16}\dfrac{F_x}{Ew}\dfrac{l^3}{h^3}$

$$a : Concetrated \quad load$$

Cantilever	Guided-End	Fixed-Fixed
$x = \dfrac{f_x l}{E}$	$x = \dfrac{f_x l}{E}$	$x = \dfrac{f_y l}{E}$
$y = \dfrac{3}{2}\dfrac{f_y}{Eh}\dfrac{l^4}{w^3}$	$y = \dfrac{1}{2}\dfrac{f_y}{Eh}\dfrac{l^4}{w^3}$	$y = \dfrac{1}{32}\dfrac{f_y}{Eh}\dfrac{l^4}{w^3}$
$z = \dfrac{3}{2}\dfrac{f_z}{Ew}\dfrac{l^4}{h^3}$	$z = \dfrac{1}{2}\dfrac{f_z}{Ew}\dfrac{l^4}{h^3}$	$z = \dfrac{1}{32}\dfrac{f_z}{Ew}\dfrac{L^4}{h^3}$

$$b : Distributed \quad load$$

Table 3.1: Displacement equations for the different geometries as derived from the small displacement theory.
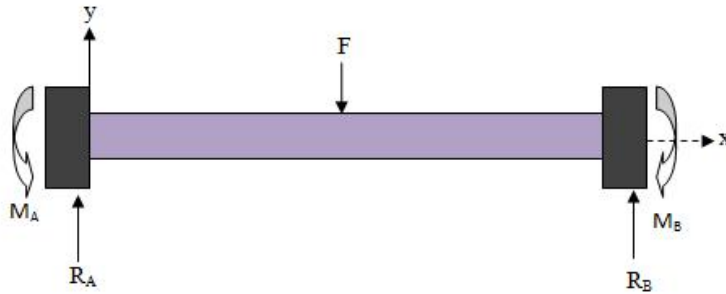
Figure 3.6: Fixed - Fixed beam with concentrated vertical load F.

sile stress is present in laterally deflected fixed-fixed beams, a nonlinear force-displacement results from the axial stress, where the effective spring constant increases with increasing load.

3.5   Spring Constants for typical structures of MEMS devices

In this section we discuss in briefly about the prime mechanical parameter characterizing a RF MEMS switch, i.e. the spring constant and how the stresses originating from the fabrication process in case of a common switch configuration, the fixed-fixed beam and its variants, impact on this parameter. The fixed-fixed beams are widely used because of the ease of fabrication and their high spring constant. In MEMS switching devices the operation of the structure is limited to small deflections e.g. 0.2 - 0.5 % of the beam length, therefore the behaviour is modelled by using a linear spring constant as mentioned in the section above. In order to account for the biaxial residual stress arising from the fabrication process, the spring constant can be modelled in two parts: (1) stiffness of the structure which accounts for the material properties (Young modulus E, and Poisson's ratio v) and (2) stress σ which is induced by the fabrication process.

In case of a beam with rectangular cross section (w x t) and length L subjected to concentrated load F, as shown in Fig.3.6, the deflection is given by:

$$y = \frac{M_A x^2}{2EI} + \frac{R_A x^2}{6EI}, I = \frac{wt^3}{L_2} \tag{3.38}$$

$$M_A = -\frac{F.a}{L^2}(L-a)^2 \tag{3.39}$$

$$R_A = \frac{F}{L}(L-a)^2(1+2a), \tag{3.40}$$

where M_A is the reaction moment at the left end and R_A is the vertical reaction to the applied load F. Deflection for a beam with concentrated load applied at the centre can be expressed in terms of its dimensions by substituting $x = L/2$ in Eqn.3.31 and is given by:

$$y = \frac{1}{EI}\left[\frac{F}{48}\left(L^3 - 6L_a{}^2 + 9L_a{}^2 - 4a^3\right)\right] \tag{3.41}$$

In MEMS applications typically the load corresponds to the actuation force and is distributed across the beam. The deflection at the centre is used to determine the spring constant. In electrostatically actuated MEMS switches, the load distribution depends on the location of the actuation electrodes. We present here a comparison of three cases, two of which are extensively used in electrostatically actuated RF MEMS switches and one of which has been implemented in the present work.

3.5.1 Deflection of a Uniformly Loaded Beam

The deflection for a beam where the load is distributed across the whole beam is found by integrating the deflection given by Eqn.3.41 over the entire beam length (from $-\frac{L}{2}$ to $\frac{L}{2}$). The spring constant for a distributed load f, the load per unit length (F = fL) is given by:

$$k = -\frac{F}{y} = 32EW\left(\frac{t}{L}\right)^3 \tag{3.42}$$

3.5.2 Spring Constant of a Beam with Residual Stress

MEMS components such as beams and cantilevers are realized in metals (Au, Al, Ni and Cu) either by sputter deposition or electroplating techniques, in polysilicon and/or dielectrics. The different processes employed to deposit/grow those materials are responsible for the so called intrinsic stress of these materials, that may vary from compressive to tensile depending upon the specific material and process. For a beam with cross section w x t the biaxial residual stress generates a force $S = \sigma(1 - \nu)$ on the both ends. In this case the beam can be modelled as a stretched wire with some flexural contributions. Considering the following load cases, the contribution of residual stress to the spring constant can be expressed as

[39]

$$k_{rs} = 8\sigma\left(1 - \nu\right)W\left(\frac{t}{L}\right) \quad uniform \quad load \tag{3.43}$$

$$k_{rs} = 8\sigma\left(1 - \nu\right)W\left[\frac{t}{L}\right]\frac{1}{3 - 2\left(\frac{x}{L}\right)} \quad load \quad at \quad center \tag{3.44}$$

$$k_{rs} = 4\sigma\left(1 - \nu\right)W\left[\frac{t}{L}\right]\frac{1}{1 - \left[\frac{x}{L}\right]} \quad load \quad near \quad the \quad center \tag{3.45}$$

The total spring constant is the sum of the contributions from beam stiffness and the biaxial residual stress. E.g. For a beam using CPW central conductor as actuation electrode with length one third of the total beam length, the total spring constant is:

$$k_t = (32)\, EW\left(\frac{t}{L}\right)^3\left(\frac{27}{49}\right) + \left[8\sigma\left(1 - \nu\right)w\left(\frac{t}{L}\right)\left(\frac{3}{5}\right)\right] \tag{3.46}$$

3.5.3 Critical Stress

The amount of compressive stress that a beam can withstand before buckling is called critical stress and is given by:

$$\sigma_{cr} = \frac{\pi^2 E t^2}{3L^2\left(1 - \nu\right)} \tag{3.47}$$

From eqn. 3.47 one can easily see that, considering that the micromechanical structures are in general very slender, the critical stress is very low compared to the typical values of the intrinsic stress that can be controlled. For this reason materials with tensile stress are favoured.

3.5.4 Spring Constants of Different Support Beam Shapes

In Fig 3.7 different type of support beam shapes, typically used to lower the effective spring constant of a MEMS devices are shown. Here we report
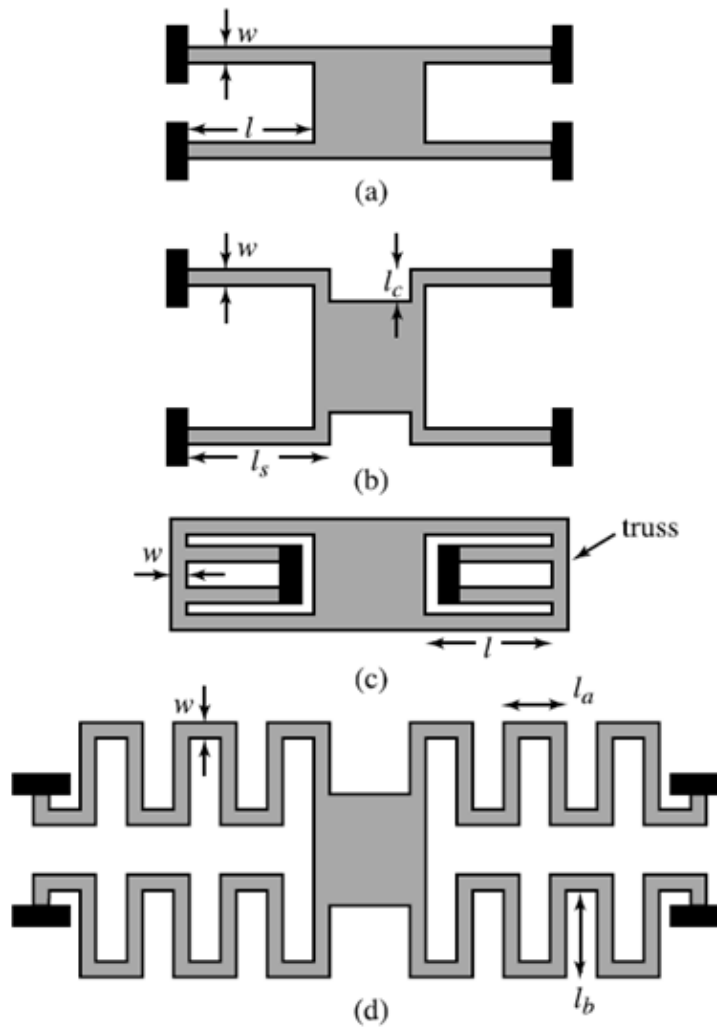
Figure 3.7: shows respectively a) fixed-fixed, b)crab leg, c)folded flexure and d) serpentine flexure spring shapes.

the expression of the spring constant for each of them. Details about how they can be derived can be found in [24]. Fixed-Fixed beam

$$k = 4EW\left(\frac{t}{l}\right)^3 \tag{3.48}$$

Crab leg beam

$$k = \frac{4EW\left(\frac{t}{l_c}\right)^3}{1 + \frac{L_s}{L_c}\left[\left(\frac{L_s}{l_c}\right)^2 + L_2\frac{1+\nu}{1+\left(\frac{w}{t}\right)^2}\right]} \tag{3.49}$$

Folded flexure beam

$$k \approx 2EW\left(\frac{t}{L}\right)^3 \tag{3.50}$$

Serpentine flexure beam

$$k_2 \approx \frac{48GJ}{La^2\left(\frac{GJ}{EI_x}L_a + L_b\right)n^3} \tag{3.51}$$

where n is the number of meanders in the serpentine, $G = \frac{E}{2(1+\nu)}$ the torsion modulus, $I_x = \frac{wt^3}{l_2}$ is the moment of inertia, while the torsion constant is given by

$$J = \frac{1}{3}t^3w\left(1 - \frac{192}{\pi^2} \times tw \sum_{i=1,odd} \frac{1}{i^2}tanh\left(\frac{i\pi w}{t^5}\right)\right) \tag{3.52}$$

3.6   Parallel Plate Electrostatic Actuator

The actuation or pull-in voltage is one of the most important parameters of an electrostatically actu-ated MEMS switch. This section briefly recalls the electromechanical model and provides a closed form analytical expression for the parallel plate geometry. The treatment is mainly based on the analysis provided in [39, 50]. When a voltage is applied between the beam and pull-down electrode a capacitive switch can be modelled by a lumped spring mass system as shown in Fig.3.8. The system consists of a moving plate of area A and mass m suspended by a spring with constant k, at gap height g above a fixed plate. The electrostatic actuator can be represented by a two port capacitor with voltage V and current I as effort and flow variables in the electrical domain, and force F and displacement z in the mechanical domain. Displacement of the plate attached to the spring and

the gap height variations are in opposite direction and are the flow variables in series as they share the same displacement corresponding to the applied voltage. The stored potential energy for a capacitor is given by $w(q_1) = \int_0^{q_1} e(q)dq$ where e represents the effort (voltage) and q is the displacement . For a parallel plate capacitor with capacitance $C = \frac{\epsilon A}{g}$ and $Q = CV$ the stored energy is $W(Q) = \frac{Q^2}{2C}$ and the coenergy is $W'(Q) = \frac{CV^2}{2}$ [41, 39] . For a spring attached to a fixed support, the effort (force) is F = kx, where x (displacement) is the flow variable. The stored energy for displacement x_1 is

$$W(x_1) = \int_0^{x_1} F(x)\,dx = \frac{1}{2}kx_1{}^2 \tag{3.53}$$

Thus, assuming a generalized displacement Q for the capacitor and x for the spring, this leads to the same stored energy function and we can represent the spring with a capacitance $C_{spring} = 1/k$. In a similar way the mass of the moving plate can be represented by an inductor and the damping by a resistor to arrive at an equivalent circuit for the mechanical domain as shown in Fig. 3.9. In the static analysis we ignore the mass and damping. In the spring model in Fig. 3.8 we have to consider both the electrical and the mechanical stored energy. Considering the gap as an independent variable the co-energy is given by:

$$W(V,g) = QV - W(Q,g), Q = \frac{\partial W'(V,g)}{\partial V} \tag{3.54}$$

$$F = \frac{\partial W'(V,g)}{\partial g}, W'(V,g) = \int_0^V \frac{\varepsilon A V^2}{2g} \tag{3.55}$$

From which we find $Q = \frac{\varepsilon A V_{in}{}^2}{2g}$, $g = g_0 - z$ $and z = \frac{F}{K}$ Using above equations the gap can be expressed as :

$$g = g_0 - \frac{\varepsilon A V_{in}{}^2}{2kg^2} \tag{3.56}$$
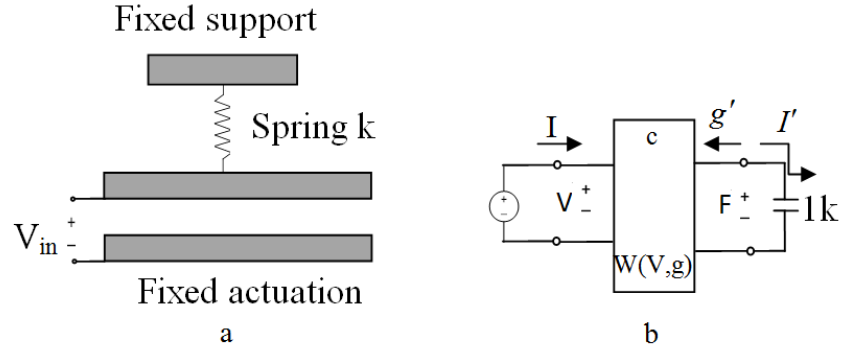
Figure 3.8: The massless spring model and the electromechanical equivalent circuit model
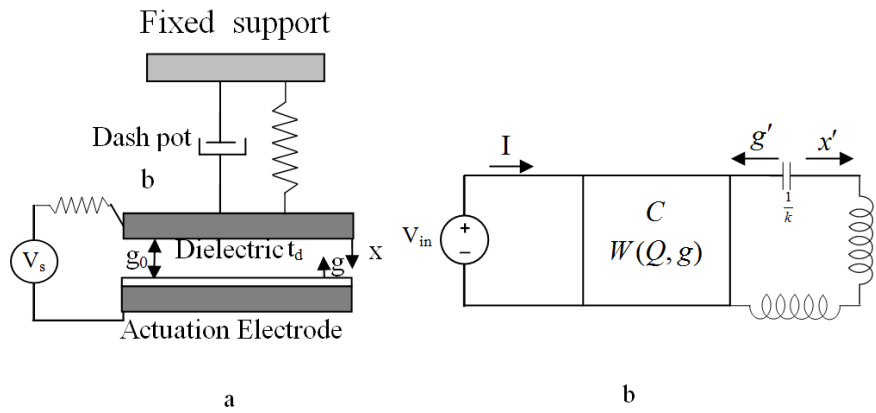
Figure 3.9: Electrostatic actuator (a) with elements representing the inertia of the movable beam, mechanical damping and source resistance of the electrical network. (b) shows the equivalent circuit model in the electrical and mechanical domain.

3.6.1 The Pull-in Voltage

A voltage-controlled parallel plate actuator exhibits an important behaviour called pull-in (Fig.3.10). Considering the position of the upper plate subjected to spring force in the upward direction and electrostatic attraction in the downward direction, the net force is[39]:

$$F_{net} = \frac{-\varepsilon A V^2}{2g^2} + k\left(g - g_0\right) \tag{3.57}$$
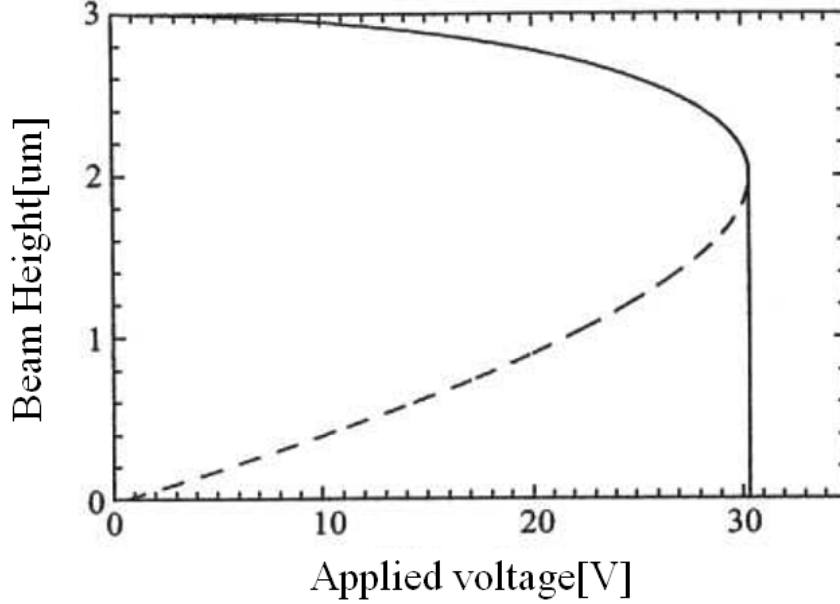
Figure 3.10: Beam height vs applied voltage for a parallel plate capacitor with mobile plate: the structure shows an instability at $(\frac{2}{3})g_0$ hat leads the MEMS bridge to collapse on the bottom electrode for higher voltages.

For a small perturbation in the position we have

$$\delta F_{net} = \left(\frac{\varepsilon A V^2}{g^3} - k\right)\delta_g \tag{3.58}$$

where δF_{net} is the gap at zero voltage and no spring extension. For a stable equilibrium δF_{net} should be negative in $Eqn.3.58 \Rightarrow k \geq \frac{\varepsilon A V_{pi}^2}{g_{pi}^3}$ Since the equilibrium gap decreases with increasing voltage, there is a specific voltage at which stability is lost. This voltage value is called pull-in voltage and denoted by V_{pi} at pull-in , $F_{net} = 0$ and

$$k = \frac{\varepsilon A V_{pi}^2}{g_{pi}^3} \tag{3.59}$$

From Eqn.3.58 and 3.59 we find that pull-in occurs at $g_{Pi} = \left(\frac{2}{3}\right)g_0$ and the voltage is:

$$V_{Pi} = \sqrt{\frac{8kg_0{}^3}{27\varepsilon A}} \tag{3.60}$$

3.6.2 The Pull-out Voltage

The minimum voltage required to keep the switch in 'on-state' is called pull- out (Vpo) or the threshold voltage. If the applied actuation voltage is decreased below Vpo the beam restores back to its original position at zero bias. In capacitive MEMS switches with a 0.01 - 0.02 μm thick isolation layer of SiO2 or Si3N4 between the beam and actuation electrode, the electrostatic force is :

$$F_e = \frac{V^2 \varepsilon \varepsilon_0 A}{2\left(g + \left(\frac{t_d}{\varepsilon_r}\right)\right)^2} \qquad (3.61)$$

where $(\varepsilon = 1 \quad for \quad g \neq 0 \quad and \quad 0.4 - 0.8 \quad for \quad g = 0)$ and accounts for parallel plate capacitance reduction due to roughness of the metal-dielectric interface. The mechanical restoring force acting on the beam is:

$$F_r = k_{es}\left(g - g_0\right) \qquad (3.62)$$

where the spring constant also includes the effect of beam stretching, which makes it also applicable to bridge structures. For the switch to stay in down position the electrostatic force (Eqn.3.62) must be larger than the restoring force given by Eqn.3.61 and this is achieved when the applied voltage is:

$$V_{po} = \sqrt{\frac{2f}{\varepsilon \varepsilon_0 A}\left(g + \left[\frac{t_d}{\varepsilon r}\right]\right)^2} = \sqrt{\frac{2k_{es}}{\varepsilon \varepsilon_0 A}\left(g_0 - g\right)\left(g + \left[\frac{t_d}{\varepsilon_r}\right]\right)^2} \qquad (3.63)$$

3.7 Comb-Drive Electrostatic Actuators

As outlined above voltage-controlled parallel plate actuators suffer from some problems like snap down and limited range of operation. An electrostatic actuator that avoids these type of problems is the so called electrostatic comb drive actuator. The operation of a electrostatic comb drive actuator is very similar to that of a parallel plate actuator. Just like in the case of the parallel plate actuator, the comb drive actuator has two

electrodes, a stationary one and a suspended one (by a mechanical spring) so that it can move under an applied force. The force required to move the suspended electrode is created by an electrostatic field between the two electrodes. This can be accomplished either by controlling the charge on the electrodes or by applying a voltage between them, as with the parallel plate actuator . The obvious difference between the comb drive and the parallel plate actuator is the geometry of the electrodes as shown in Fig 3.11, which is responsible for the characteristic of the device. As the two electrodes of a comb drive actuator are pulled together the increase in the capacitance is mostly due to the increased overlap of the teeth of the two combs. This capacitance increase is a linear function of the relative position of the electrodes. This is different from the case of a parallel plate actuator, where the capacitance is inversely proportional to the electrode spacing, i.e. the capacitance is a nonlinear function of the relative electrode positions. Therefore the comb drive is sometimes referred to as the linear electrostatic comb drive. In order to calculate the electrostatic force developed in a comb drive actuator, we consider the electric field distribution shown in Fig 3.12. We write the capacitance as a sum of two parts, one corresponding to the fringing fields and one corresponding to the field in the region of overlap between the two electrodes[46].

$$C_{tot} = C_0 + C\left(x\right) \tag{3.64}$$

The force can be written as:

$$F = \frac{\partial w^*}{\partial x}|v = \frac{\partial}{\partial x}\left(\frac{1}{2}CV^2\right)|v = \frac{V^2\partial C}{2\partial x} \tag{3.65}$$

Using the same uniform field approximation employed for the parallel plate actuator we can write:

$$F = \frac{1}{2}V^2\frac{\partial C}{\partial x} = \frac{1}{2}V^2\frac{2N\varepsilon h}{g} = V^2\frac{N\varepsilon h}{g} \tag{3.66}$$

where N is the number of comb fingers, h is the thickness of the comb
fingers (perpendicular to the plane in Fig 3.12) and g is the width of the
gap between the comb fingers. In many practical implementations of the
electrostatic comb drive the thickness h of the comb teeth is comparable
to the electrode gap g. Under these conditions the parallel plate approxi-
mation is relatively inaccurate. The most accurate representations of the
fringing field are obtained by numerical techniques, but for many purposes
this may be difficult to accomplish and therefore tabulated correction fac-
tors are used to compensate for the effects of the finite electrode thickness.
The force can then be expressed as:

$$F = V^2 N \left(\frac{\alpha \varepsilon h}{g^B} \right) \eta \qquad (3.67)$$

where α, β, η are fitting parameters extracted from simulations.
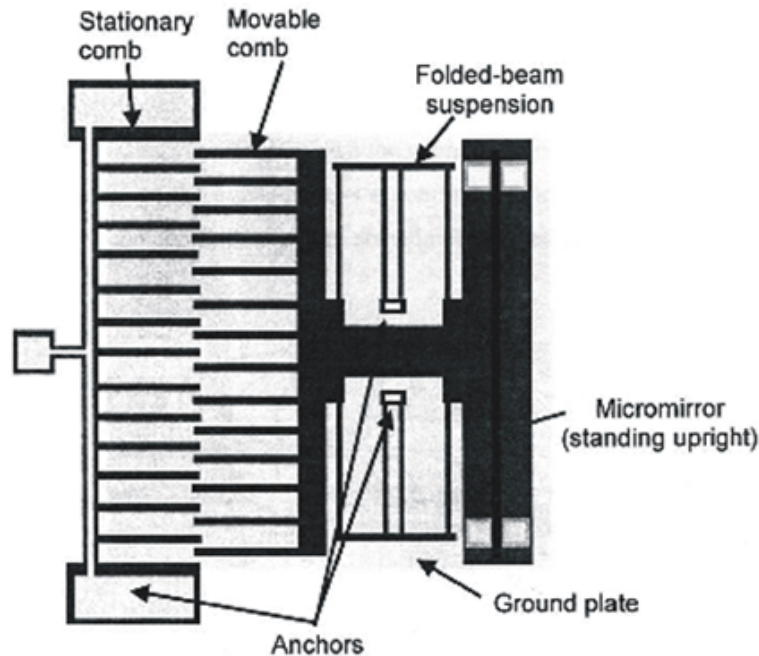
Figure 3.11: Electrostatic combdrive actuator. The voltage across the interdigited elec-
trodes creates a force that is balanced by the spring force in the crab leg suspension.

From the above expression it can be easily seen that the force in the voltage controlled comb drive actuators is not a function of the displacement.

The voltage-controlled comb drive actuator is however susceptible to snap-down in the transversal direction. Fig 3.12 shows clearly that each tooth of the movable comb is attracted sideways towards its nearest neighbor on both sides. In an ideal case the gaps on both sides are equal so that the sideways forces exactly balance. In reality however the two gaps will not be exactly equal and therefore there will develop a net sideway force in one direction or the other. It is also important to be aware that even in the ideal case the comb drive actuator will be unstable if the voltage and the overlap between the comb teeth are too large. This happens when the created sideway forces are so big that an infinitesimal offset from the perfectly centered position makes the comb electrode snap sideways.

In order to analyze the stability of a comb drive actuator, an expression for the potential energy is needed. This is derived by generalizing the expression for the capacitance of the comb drive actuator to the situation where the movable teeth are asymmetrically placed between the stationary teeth :

$$C = N\varepsilon h x \left(\frac{1}{g-y} + \frac{1}{g+y} \right) \tag{3.68}$$

The force can been expressed :

$$F_x = \frac{1}{2} V^2 \frac{\partial C}{\partial x} = \frac{1}{2} V^2 N\varepsilon h \left(\frac{1}{g-y} + \frac{1}{g+y} \right) = k_x x \tag{3.69}$$

therefore

$$V = \sqrt{\frac{2k_x x}{N\varepsilon h \left(\frac{1}{g-y} + \frac{1}{g+y} \right)}} \tag{3.70}$$

In the transversal direction a similar expression for the force balance can be written:

$$F_y = \frac{1}{2} V^2 \frac{\partial C}{\partial y} = \frac{1}{2} V^2 N\varepsilon h \left(\frac{1}{(g-y)^2} - \frac{1}{(g+y)^2} \right) = k_y y \tag{3.71}$$
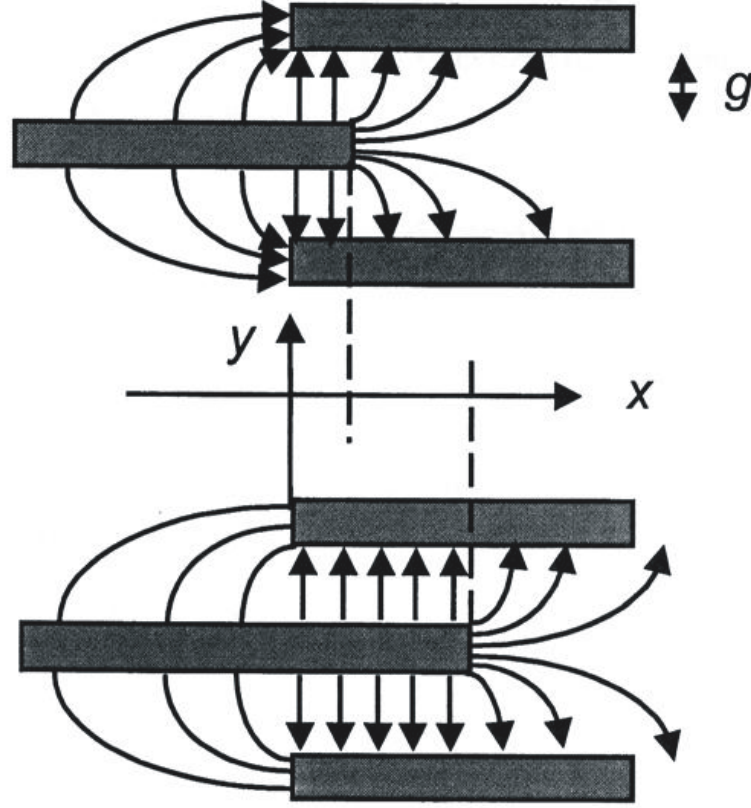
Figure 3.12: Electric field distribution in the comb-finger gaps. The direction of the x coordinate is chosen opposite of the parameter g in the parallel plate actuator.

Finally an equation for the total potential energy in the actuator can be obtained:

$$PE = \frac{1}{2}k_x x^2 + \frac{1}{2}k_y y^2 - \frac{1}{2}CV^2 \tag{3.72}$$

$$PE = \frac{1}{2}k_x x^2 + \frac{1}{2}k_y y^2 - \frac{1}{2}Nhx\left(\frac{1}{g-y} + \frac{1}{g+y}\right)V^2 \tag{3.73}$$

Values of y where $\frac{\partial PE}{\partial y} = 0$ are all possible equilibrium position, but only those that have $\frac{\partial^2 PE}{\partial y^2} > 0$ are stable, where $\frac{\partial^2 PE}{\partial y^2}$ are expressed as :

$$\frac{\partial PE}{\partial y^2} = k_y - \left(\frac{1}{(g-y)^3} + \frac{1}{(g+y)^3}\right)\frac{2k_x x^2}{\left(\frac{1}{g-y} + \frac{1}{g+y}\right)} \tag{3.74}$$

$$\frac{\partial^2 PE}{\partial y^2} = k_y - 2k_x x^2 \left(\frac{(g+y)^3 + (g-y)^3}{(g-y)^3(g+y)^3} \right) \frac{g^2 - y^2}{2g} \qquad (3.75)$$

$$\frac{\partial^2 PE}{\partial y^2} = k_y - 2k_x x^2 \frac{g^2 + 3y^2}{(g^2 - y^2)^2} \qquad (3.76)$$

For $y = 0$ this expression simplifies to:

$$y = 0 \Rightarrow \frac{\partial^2 PE}{\partial y^2} = k_y - \frac{2k_x x^2}{g^2} \qquad (3.77)$$

In the ideal case ($y = 0$) the stability criterion is:

$$k_y - \frac{2k_x x^2}{g^2} > 0 \Rightarrow \frac{x}{y} < \sqrt{\frac{k_y}{2k_x}} \qquad (3.78)$$

From this expression it can be seen that sideway snap down limits the deflection of the electrostatic comb drive actuator. For best performance the ratio of the transversal (y direction) to the longitudinal (x direction) spring constant should be as large as possible.

3.8 Comparison of the Two Actuation Mechanisms

Now the force developed in parallel plate and comb drive actuators can be compared. The first order expressions for the force in these two actuators are see Fig 3.13:

$$Comb - drive : F_{cd} = \frac{N\varepsilon h V^2}{d} \qquad (3.79)$$

$$Parallel \quad plate \quad actuator : F_{pp} = \frac{A\varepsilon V^2}{2g^2} \qquad (3.80)$$

In order to compare these two expressions, we write the area of the comb drive acuators as:

$$A_{cd} = 4Ndh \qquad (3.81)$$
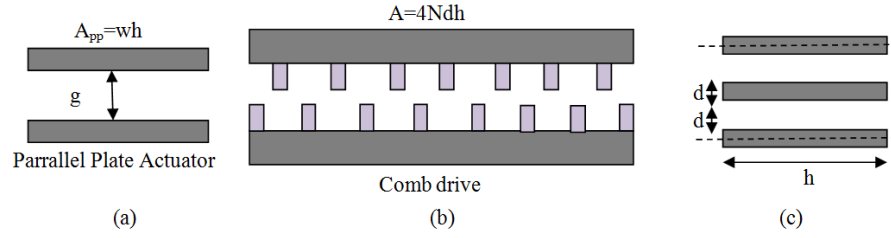
Figure 3.13: Schematic of a)the parallel-plate and the comb drive actuator and b) shows one unit cell of a periodic comb drive actuator[46].

Given these definitions the ratio of the force produced by a comb drive and a parallel plate actuator of the same cross-sectional area is found to be:

$$\frac{F_{cd}}{F_{pp}} = \frac{g^2}{2d^2} \qquad (3.82)$$

This expression shows that the comb drive actuator can generate substantially larger forces than the parallel plate actuator. In the assumption that the parallel plate actuator is voltage controlled and can be operated over one third of its gap ($\frac{g}{3}$) and the gap in the combdrive is determined by the lithographic resolution, we find:

$$\frac{F_{cd}}{F_{pp}} = \frac{9(range)^2}{2(line \quad width)^2} \qquad (3.83)$$

In many applications the total range of travel of the actuator might be wanted one or two orders of magnitude larger than the lithographic line-width resolution. In all these applications the comb drive actuator is clearly largely superior to the parallel plate actuator, at least if the maximum available force is important. It should be remembered however that the range of the comb drive actuator is also limited by snap down as discussed above. By using the expression found for the deflection of the comb drive actuator ($x_{max} = d\sqrt{\frac{k_y}{2k_x}}$), we can rewrite the force ratio as:

$$\frac{F_{cd}}{F_{dd}} = \frac{9}{2}\frac{d^2\frac{k_y}{2k_x}}{d^2} = \frac{9k_y}{4k_x} \qquad (3.84)$$

Of course this equation is valid for the situation where the parallel plate actuator and the comb drive actuator have the same range of motion, given by the maximum range of motion possible in the comb drive actuator. This is not necessarily the most fair way to compare these two actuators. Often it is better to use average to trade off force and range such that their product is constant . In many applications it is therefore found that the force x range product is a better figure of merit than the force ratio:

$$\frac{F_{cd} \times range_{cd}}{F_{pp} \times range_{pp}} = \frac{g^2 \sqrt{\frac{k_y}{2k_x}} g}{2d^2 \frac{g}{3}} = \frac{3g^2}{2d^2} \sqrt{\frac{k_y}{2k_x}} \approx \frac{3}{2} \sqrt{\frac{k_y}{2k_x}} \tag{3.85}$$

It can be seen from this equation that now the comb drive actuator is not as much favored as in the case derived earlier. If the mechanical springs are well designed $k_y \gg k_x$ however the comb drive actuator is still superior to the parallel plate actuator with a substantial margin.

3.9 Basic Dynamic Response of RF MEMS Switches

The derived expressions for pull-in and pull-out voltage of a beam describe the static response of the switch. In order to describe the dynamic behaviour of the switch in terms of resonant frequency and switching time it is necessary to include the finite mass of the mobile structures together with the mechanical damping forces that arise from the viscous air flow generated by the up and down movement of the mobile electrode.
In the particular case of a parallel plate with vertical movement it can be shown [2] that the damping coefficient is:

$$b = \frac{3}{2\pi} \frac{\mu A^2}{g_0^3} \tag{3.86}$$

where A is the area of the device. Damping can be decreased substantially by the use of holes in the top membrane. The effect of holes on damping

coefficient is described in [3] and can be estimated by:

$$b = \frac{12}{N\pi} \frac{\mu A^2}{g_0^3} \left(\frac{p}{2} - \frac{p^2}{8} - \frac{ln(p)}{4} - \frac{3}{8}\right) \tag{3.87}$$

where N is the total number of holes per unit area and p is the fraction of open area on the plate. An approximate formula for a quality factor ($Q = \frac{k}{\omega_0 b}$) of a cantilever is given by :

$$Q_{cantilver} = \frac{\sqrt{E\rho t^2}}{\mu(\omega l)^2} \tag{3.88}$$

where ω and l is the width and length of the cantilever ,Q factor of the fixed-fied beam is the Q of a cantilever beam of haf its length[11].

$$Q_{fixed-fixed} = \frac{\sqrt{E\rho t^2}}{\mu(\frac{\omega l}{2})^2} g_0^3 \tag{3.89}$$

In practice it turns out that the Q-factor does not affect the switching speed of structures as long as $Q \geq 3$. However it has an impact on the release time in case of large displacement the corresponding Q using the equation above is:

$$Q_e = Q(1.1 - (\frac{x}{g_0})^2)^{\frac{3}{2}}(1 + 9.638(\frac{\lambda}{g})^{1.159}) \tag{3.90}$$

where in (eq.3.89) Q is the nominal small displacement quality factor at $g = g_0$, and the second term is a correction factor introduced by [61] to account for large displacement. This results in $Q \neq 0$ for $x = g_0$ when the beam touches the pull down electrode.

3.10 First Order Estimation of the Switching Time

The dynamic behaviour of the beams is modelled by considering a beam of mass m suspended by a spring with constant k and squeeze film effects

represented by the damping coefficient b. The resulting one-dimensional model is shown in Fig.3.14 and the governing equation is:

$$m\frac{d^2x}{dt^2} + b\frac{dx}{dt} + kx + k_sx^3 = F_e + F_c \tag{3.91}$$

where k includes the bending and the intrinsic stress and k_s the stretching effects of the beam. The damping factor is $b = \frac{k}{\omega_0 Q}$
and F_e and F_c are two forces as described below. The voltage applied to the switch and the external forces acting on the switch (for $x = g_0 - g$) are given by:

$$V = V_s - i(t)R_s = V_s - (C\frac{dV}{dt} + V\frac{dc}{dt})R_s, \quad C = \frac{\epsilon_0 A}{g_0 + \frac{t_d}{\epsilon_r} - x} \tag{3.92}$$

$$F_e = \frac{1}{2}\frac{\epsilon_0 AV^2}{(g_0 + \frac{t_d}{\epsilon_r} - x)^2}, F_c = \frac{C_1 A}{(g_0 - x)^3} - \frac{C_2 A}{(g_0 - x)^{10}} \tag{3.93}$$

where V_s is the source voltage , F_e is the electrostatic pull-down force and F_c represents the attractive van der Waals forces (first term) and repulsive nuclear forces (second term) between the metal and dielectric layer [62]. The constants $C_1 = 10^{-80}Nm$ and $C_2 = 10^{-75}Nm^8$ determine the surface energy due to the van der Waals attraction and the equilibrium distance from the surface respectively. The switching time is obtained using Eqn.3.92 at $x = g_0$. It has been shown that this closed form agrees well with numerical modelling and the measurements [39]. In a similar way the equation for a damping-limited system $Q < 0.5$ can be derived with the assumption of constant damping with height and neglecting the acceleration and the spring constant [39]. For the electrostatic pull-in force we have $F_e = b\frac{dx}{dt}$. The solution using integral methods gives the following expression for the switching time t_s:

$$t_s = \frac{2bg_0^3}{3\epsilon_0 AV_s^2} \simeq \frac{9V_{pi}^2}{4\omega_0 QV_s^2}, \quad V_s \gg V_{pi} \tag{3.94}$$

64
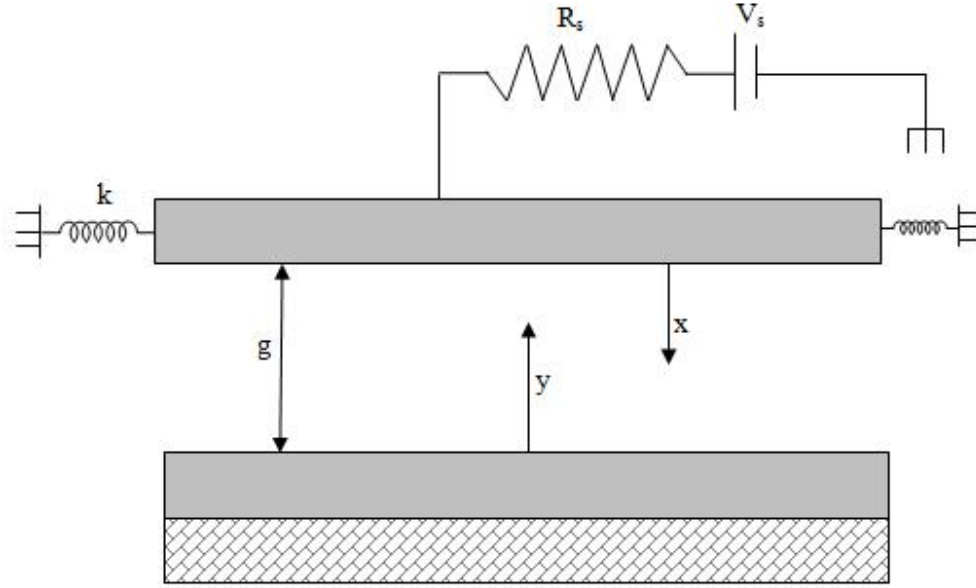
Figure 3.14: The 1-D MEMS beam model and its coordinate system.

Another estimate can be made by assuming a constant Fe and constant velocity approximation $\dfrac{dx}{dt} = \dfrac{g_0}{t_s}$. In this case the switching time can be estimated by

$$t_s = \frac{2bg_0^3}{\epsilon_0 V_s^2} \simeq \frac{27V_{pi}^2}{4\omega_0 Q V_s^2}, \quad V_s \gg V_{pi} \tag{3.95}$$

For the damping-limited case the Eqn.3.95 tends to overestimate the switching time while Eqn.3.94 tends to underestimate it. Clearly, a trade-off has to be found between the switching response and the actuation voltage. In the case of a real switch one has to distinguish between the pull-in time, that is the time necessary to close the switch, and the release time, i.e the time required for the switch to move from the down-state to its original height (or within 5% from this value). From these simple expressions it is evident that the main device parameters affecting the switching time are

the air gap, the mass of the mobile structure, the damping force generated by the viscous air flow and the restoring force generated by the spring. Among these the damping coefficient requires a more detailed description.

3.11 The Squeeze Film Model

There are several energy dissipation mechanisms that are common in MEMS devices [32]:

- Losses to surrounding fluid/air due to acoustic radiation

- Losses into microstructure supports due to local deformation and micro slip

- Intrinsic damping due to losses that are generated by the molecular interactions in the material during deformation of a microstructure

- Losses due to viscous friction (viscous air damping)

Among the presented damping sources, viscous air damping is the most significant source of energy dissipation in MEMS at atmospheric pressure. Therefore we assumed air (or gas in general) as the most important working fluid for the devices analyzed in our work. Viscous air damping can be subdivided in two subsections:

- Slide film damping, which dominates in laterally moving devices. e.g. comb drive actuators.

- Squeeze film damping, which dominates when the device moves vertically or bends towards a nearby rigid surface with a thin air film in between, e.g. microswitches and torsional micromirrors.

Fig 3.15 shows the schematic diagram of the moving parallel plate.Both slide and squeeze film damping are studied in many works. As the squeeze

film damping originates from the fluid flow around the microstructure, its description requires the use of the fluid dynamic equations. The continuous field regim squeeze film damping of a microstructure vibrating in a fluid is governed by Navier-Stokes equations, which, due to their intrinsic complexity, are solved using computational fluid dynamic methods that are one of the most demanding tasks for FEM solvers. One of the most common methods to avoid the use of the Navier-Stokes equations for modelling squeeze film damping in MEMS consists in applying the Reynolds equation, which is used in lubrication theory to describe the behaviour of a thin fluid film between two moving surface, and is expressed by

$$\frac{\partial}{\partial x}\left(\frac{\rho g^3}{\mu}\frac{\partial p}{\partial x}\right) + \frac{\partial}{\partial y}\left(\frac{\rho g^3}{\mu}\frac{\partial p}{\partial y}\right) = 12\frac{\partial(\rho g)}{\partial t} \tag{3.96}$$

where the gas density ρ, the gas pressure in the gap , and the gap thickness are functions of time and position (x,y) and μ is the dynamic viscosity of the gas. The Reynolds equation is a nonlinear partial differential equation which is derived from Navier-Stokes equation, which includes the conservation of mass and assumes:

- the fluid is Newtonian, i.e. the shear stress is directly proportional to the velocity;

- The fluid obeys the ideal gas law;

- The inertia and body forces are negligible compared to the viscous and pressure forces;

- The variation of pressure across the fluid film is negligibly small;

- The flow is laminar;

- The thickness of the fluid film is very small compared to the lateral extent of the moving and stationary plates;
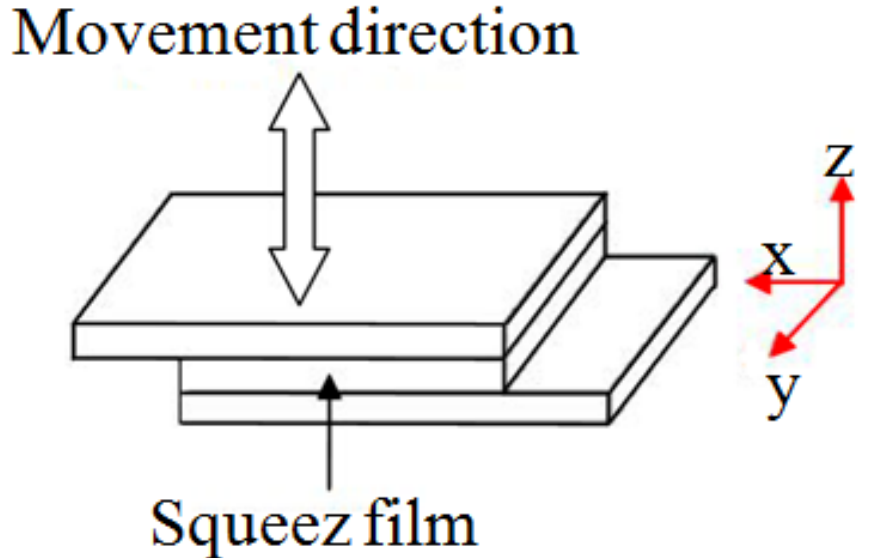
Figure 3.15: Shows the schematic diagram of the moving parallel plate.

- The fluid can be treated as a continuum that does not slip at the boundaries [32] .

A general measure of validity of these assumptions is the Knudsen number K_n :

$$K_n = \frac{\lambda_0 Patm}{P_0 g_0} \tag{3.97}$$

where p_0 is the working pressure in the gap, λ_0 is the mean free path of the air particles at ambient pressure P_{atm} and equal to 101.325 kPa and g is the nominal gap height.

- $K_n < 0.001$ cotinuum flow.

- $0.001 < K_n < 0.1$ slip flow.

- $0.1 < K_n < 10$ trasitional flow.

- $K_n > 10$ free molecular flow.

Many MEMS devices may be designed to operate at a very low pressure with a very small gap be-tween the electrodes. Under such conditions the Knudsen number does not belong to the continuum regime.Fortunately extensive research has extended the validity of Reynolds equation beyond the continuum regim, thereby enabling the description of the flow using a single model. A convenient way to account for gas rarefaction is to modify the dynamic viscosity . Veijola et al introduced the following expression for the so-called effective viscosity μ_{eff} , which is valid over a wided range of K_n, i.e. $0 \leq K_n \leq 880$[32] :

$$\mu_{eff} = \frac{\mu}{1+9.638 K_n^{1.159}} \quad (3.98)$$

3.12 Short Notions on Electrical Degradation Phenomena

3.12.1 Charging

One of the first degradation mechanisms identified in RF MEM switches is dielectric charging, caused by charge injection into the dielectric layers covering the actuation electrodes due to the high applied voltages. The injected charges accumulate in the dielectric, which in turn induces a measurable voltage shift in the actuation characteristics of the device. Even though this phenomenon has been studied extensively the exact mechanisms for the transfer and trapping of charges are not yet fully understood. What is known is that as the charges get trapped within the dielectric, they screen the applied electric fields that are used to control the actuation and release of the switch. The end result is that a screening field builds up within the dielectric opposite to the field applied to operate the switch. A voltage is associated to this screening field, which is opposite to the applied voltage. As the charge builds up, this screening voltage detracts

from the actuation voltage until it becomes equal to the applied voltage. At this point the pulling force on the membrane is totally compensated and the switch cannot be operated anymore. Conversely, when the applied electric field is removed, the electric potential of the trapped charges keeps on attracting the membrane. Since the hold-down voltage for a switch is much smaller than its actuation voltage, the trapped charges may provide enough potential to keep the membrane down still after the bias voltage has been removed. This results in a switch being stuck down. Experience shows that stuck switches are the most common cause of failure. Given the high electric field responsible for tunnelling, trapping and the resulting failure (sticking) of the MEMS switch, we anticipate that the lifetime of the switch is related to the magnitude of the applied electric field. One physical mechanism that is thought to be involved in the dielectric charging is the Frenkel Pool conduction. The equation for Frenkel-Poole conduction [42, 59]is:

$$J \approx V_e \;{}^{+2a}\sqrt{\dfrac{V}{T}} - \dfrac{q\Phi_B}{k_T} \tag{3.99}$$

where J is the current density due to Frenkel-Poole conduction, V is the applied voltage, T is temperature in Kelvin, Φ_B is the barrier height, k is Boltzman's constant and a is a constant composed of electron charge, insulator dynamic permittivity and film thickness. This equation represents an exponential relationship between the current and the applied electric field. As such one might expect that the lifetime of MEMS switches is exponentially related to the applied voltage. A straightforward experiment is to measure the switch lifetime (number of actuations until failure) as a function of applied electric field. This provides valuable insight into the mechanisms of charging and switch failure, yielding information on how the applied actuation voltage affects switch lifetime. In practice the dielectric charging can have two consequences i.e. stiction and screening as

described above [30, 40]see Fig 3.16.

3.12.2   Power Handling Capability

The power associated with the RF signal flowing through the switch (of micro scale) can be the origin of device self-actuated even if the actuation signal is not applied. These events can be classified as follows:

- Self-actuation: A strong enough RF signal can have a DC component sufficient to accidentally actuate the device.

- Latching: A strong enough RF signal can have a DC component equal to the hold-down voltage. In this case the bridge will be not more released[4].
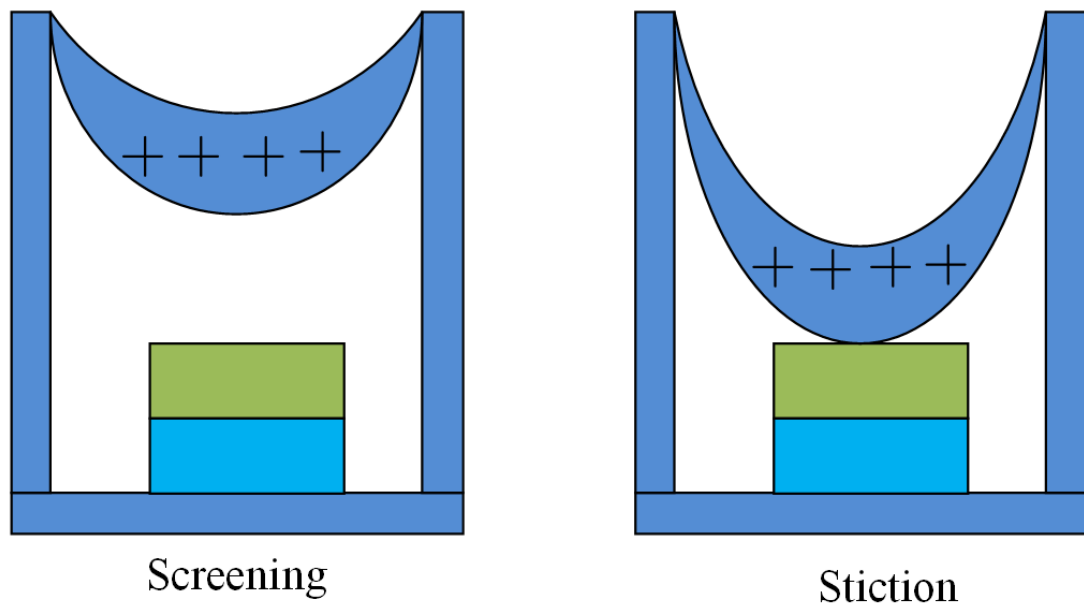
Figure 3.16: a) schematic view of the charge distribution causing the partial screening of the actuation voltage b) the stiction of the suspended gold membrane.

Theoretical analysis

As shown earlier the actuation voltage of a suspended membrane can be approximated with equation (3.60). If an RF signal with V_0 amplitude is applied to the switch membrane, a DC component will be generated. This will be equal to:

$$V_{DC} = \frac{V_0}{\sqrt{2}} \tag{3.100}$$

and the equivalent power at the switch input port will be:

$$P_{IN} = \frac{V_0^2}{Z_0} \tag{3.101}$$

Two situations can occur: if the actuation voltage V_{Act} is lower that the DC component generated by the RF signal, the switch will suddenly actuate itself, i.e. self actuation happens, while in case the voltage associated the DC component of the RF signal is higher than the pull-out voltage the switch once actuated will not release as long as the RF signal is applied, i.e. latching occurs. Typically the necessary power to actuate a capacitive switch is about 4 W, while on the contrary, for the latching phenomena, the RF power to keep a device actuated is in the order of 500 mW.

3.12.3 Contact Resistance Variation

This reliability issue is mainly related to resistive switches. The aging of the switch can cause a gradual increase of the contact resistance. This in turn can then lead to an increase of the temperature at the contact point and finally to a failure of the switch by contact welding or simply by increased RF insertion losses (depending on the criteria adopted for a failure). In extremis the increased resistance in the closed state can become comparable to the resistance exhibited by the switch in the open state, impairing so definitively the function of the switch. In Figure 3.17 it is possible to see the comparison between apparent contact area and

the real contact area in a gold-gold metal contact. The reduced size of the contact point increases the series resistance of the device degrading its electrical performances [23, 22].

Theoretical Analysis

One of the prime sources of contact resistance is the roughness of two surfaces that get in contact. In fact, when two surfaces come into contact, at microscopic level only a finite number of points get really in contact. This leads to a geometrical reduction of the effective surface for the current flow, which increases the resistance of the electrical path. Moreover, for a contact with a radius similar to the electron mean free path (10 nm) or smaller, the current flowing is constricted by scattering around the contact (boundary scattering). Taking into account these phenomena, the contact resistance can be approximated with:

$$R_s = \frac{1 + 0.83(\frac{l}{a})\rho}{1 + 0.33(\frac{l}{a})2a} + \frac{4\rho l}{3\pi a^2} \tag{3.102}$$

where R_s is the contact resistance, l is the mean free path, a is the contact radius and ρ is the electrical resistivity. The order of magnitude of the radius of the contact area for two adhering materials is:

$$a = \sqrt{\frac{F_c}{\pi H}} \tag{3.103}$$

where F_c is the contact force and $H\,[Pa]$ is the material hardness, which can be obtained with standard tests, e.g. the Knoop method [14]. Due to the Joule law, a current flowing through a contact tends to heat it up to a temperature level called "supertemperature". This temperature can be hundreds of degrees higher than the surrounding material one. If we assume that the Widemann-Franz law is valid for metals and that the current and the thermal flow have the same direction, the super temperature T_s is given

by:

$$T_s{}^2 = \frac{V^2}{4L} + \frac{(T_b{}^2 - T_0{}^2)^2}{4V^2} + \frac{T_b{}^2 + T_0{}^2}{2} \tag{3.104}$$

where V the voltage drop on the contact, $L = 2.47 * 10^{-8} \frac{V^2}{K^2}$ is the Lorentz constant, T_b is the membrane temperature near to the contact zone and T_0 is the substrate temperature. Tests carried out at macroscopic scale have shown that the contact resistance grows with the supertemperature. However, above the supertempreture, a softening of the contact happens with a consequentially increase of the contact radius and a reduction of the electrical path resistance. The contact area variation can be approximated by:

$$\frac{A}{A_0} = \frac{R_0{}^2}{R^2} \left[1 + \frac{2L}{3K}(T_s - T_0) \right]^2 \tag{3.105}$$

where A is the softened contact area, A_0 is the contact area before the softening, R is the softened contact resistance and R_0 is the contact resistance before the softening.

3.13 Short Notions on Mechanical Degradation Phenomena

Due to the mechanical nature of the MEMS devices in addition the electrical degradation phenomena there exist also many mechanical degradation phenomena and processes that can impair the reliability of the MEMS devices. These degradation processes depend strongly on the materials used, the design and the type of load applied to the devices. Here after the most relevant to RF MEMS switches are shortly presented.

3.13.1 Stray Stress

This is a endemic source of failure always present in thin film structures. Stray stresses are defined as stresses in films that exists even in the absence

Apparent Contact Area
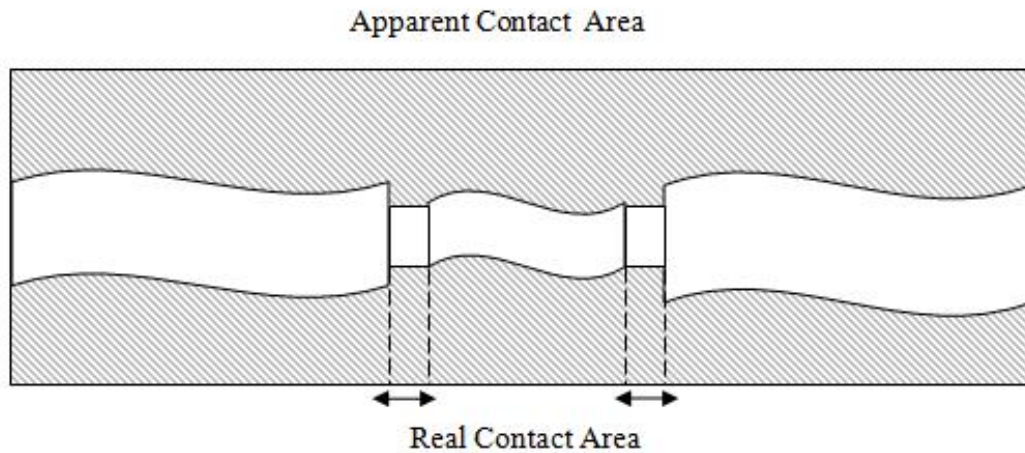
Figure 3.17: Comparison between apparent contact area and real contact area in a gold-gold metal contact.

of external forces applied. In MEMS small stresses cause noise in the sensor output, while large stresses lead to mechanical deformation. This mechanical deformation can impair the device functionality changing the nominal working condition [44].

3.13.2 Creep

When a load is applied to a material its strain response consists of an instantaneous elastic elongation related to the Young modulus and a time dependent term. The latter is due to creep. The classical definition of creep is "a time-dependent deformation of a sample caused by external mechanical loads, even constant over time". A possible way to observe creep generation is by looking at the time depending stress relaxation. Most metals exhibit creep at temperatures higher than 2/3 of its melting point. In the MEMS devices creep can be observed as a slow deformation of movable metal parts, while related to the package it shows up as fractures in the solder joints. The later one can sometimes be detected by

scanning acoustic microscopy, microscopy or SEM microscopy on a cross-section. Creep is caused by high stresses or stress gradients especially in metals that are creep sensitive (e.g. Al and solder alloys) combined with high temperatures (e.g. with high RF power applied and large CTE difference between the materials). Creep can also be detected in the shift of electrical parameters (pull-in voltage, capacitance swing, resonance frequency,...). In practice it is evident only in devices and packages with metal parts(such as Al bridges, solder joints) that are creep sensitive in the above mentioned load conditions or in devices working in an high temperature environment. Creep is a non-reversible process that results in a permanent non recoverable damage [44].

3.13.3 Fatigue

Fatigue is a failure mechanism consisting in the decrease of material strength due to cyclic loads. Fatigue can occur in all MEMS device. The cyclic loading leads to the formation of surface microcracks that cause the slow weakening of the material over time and create localized plastic deformations. Fatigue causes thereby a gradual change in the properties of a material After a first nucleation of the damage crack initiation occurs and propagates through the structure till final collapse caused by brittle rupture occurs. From this qualitative picture it is evident that fatigue is a time dependent phenomenon that affects the mechanical behavior of the MEMS devices. Fatigue can develop in different ways, the cracks can start at the surface (local high stress location points e.g. at rough surfaces) or in the bulk (defect growing). It can further grow because of stress changes at the crack tip (where high local stress is present) during cyclic loading or because of stress corrosion cracking, e.g. in crystalline Si a crack can grow because of faster oxide growth in the high tensile stress regions near the crack tip. Sometimes the origin is a large motion that induces stress changes near stress

concentration points. Such points are typically found at sharp edges, rough surfaces or inside non-uniform material. Therefore fatigue is mainly seen in the fracture of beams or hinges, cracks at places where motion takes place and high stress is present (e.g. sharp edges of moving hinges). In presence of fatigue a shift of electrical parameters (pull-in voltage, resonance frequency.) can be observed.Due to their inherent nature MEMS devices where a lot of cyclic motion is present may be more susceptible to fatigue. This is a non-reversible process, resulting in permanent damage [44].

3.14 Short Notions on Environmental Degradation Phenomena

3.14.1 Capillarity stiction

Surface micromachined devices, for reasons related to processing, are extremely hydrophilic. A hydrophilic surface in a humid atmosphere will experience both, condensation, which can create bending moments in structures and capillary forces, which will create stronger adhesive bonds than Van der Waals forces alone [11, 8, 58]. Water or fluid that is present in the small cavity between two moving parts or a moving and a fixed part can keep them together due to its liquid surface tension [11, 8, 58]. The stiction force depend on the roughness of the surfaces (the rougher the smaller the force), on the temperature and on the pressure of the environment. Stiction can be best observed using an optical microscope, motion analysis instrumentation (the stuck part will of course not move) optical or a profilometer. Stiction can also be observed in a SEM but a low-vacuum instrument that works at low voltage is required as a high vacuum can remove the fluid from the sample and the high voltage electron beam of the SEM can induce charging which could also result in stiction. The main

occurrence of capillary stiction is after the release etch, i.e. during the drying of the MEMS due to the water left under the structure that can pull down the structure by capillary forces. The use of an appropriate release method can prevent this problem. However it might also occur during use of the MEMS device in a humid environment. This can be prevented by protecting the MEMS by a hermetic package with a low internal humidity. In addition the following factors should be taken into account:

- MEMS with a large restoring force (stiff structures) will be less sensitive to capillary stiction than a MEMS with weak and slender structures.

- a smoother surface can be more easily affected by stiction.

Capillary stiction can occur in all MEMS. Due to its nature this is a failure that in can be avoided in general by good processing practice (taking care during etch of the sacrificial layer), optimal design (stiff moving parts) and/or protection of the MEMS against high humidity(packaging). In Oya et al.[58],reported on capacitive switches that kept functioning even at humidity levels as high as 95% RH. This indicates that if the restoring forces of the switches are large enough (stiff bridge), capillary stiction will not be an issue. As an additional precaution anti-stiction coatings can be used to produce hydrophobic surfaces, although those currently under investigation are only applicable to certain types of devices and not yet "industry-ready".

3.14.2 Electro-static Discharge and Electrical Over-stress

Electrical over-stress (EOS) is a common term referring to voltage / current beyond the nominal values of the device. Electro-static discharge (ESD) typically occurs when a device is improperly handled or gets in contact with a charged body. These effects are known to have catastrophic effects

in traditional solid state circuits and also in MEMS [47, 48]. Typically the application of high voltages can cause breakdown in dielectrics and even arching and subsequent melt of part of the structures. The only possible countermeasures lay in the robust design and the strict respect of the isolation distances (according to the electrical rigidity of the materials, i.e. dielectrics and air) as in MEMS devices it is in general not possible to include active discharge and protection devices.

3.14.3 Temperature Stress

Due to the fact that MEMS devices are built out of many different materials which have different thermal expansion coefficients they can have internal stresses which are in general quite temperature dependent. This is due to their inherent mechanical design, which through the substrate induces changes in the stress state of the mechanical membrane as the device experiences a temperature variation.

Temperature Induced Elastic Deformation

Differences in the coefficient of thermal expansion (CTE) between two connected materials can lead to temperature induced elastic deformation or non-uniform temperature differences within the bridge of a switch or within a beam. This will cause anomalous buckling of a MEMS structure during temperature changes or during functioning. This effect is mainly found when materials with very different CTE are used, if inhomogeneous heating of a device during functioning occurs or in designs that do not take into account thermal expansion. From a functional point of view changes in the pull-in/pull-out voltage of switches or changes of the resonant frequency and Q-factor in resonators are observed [18].

Temperature Induced Plastic Deformation

A permanent temperature induced change in a material (annealing) may be caused by plastic deformation. These changes include stress alteration, softness, ductility, toughness, electrical or magnetic or other physical properties changes. The deformation goes together with changes in crystallinity and micro-structure. All materials have a critical temperature above which the material properties change (grain growth, dislocation motion, etc.). If this temperature is exceeded during functioning or processing or packaging, the device will deform in a irreversible way, similar to the anomalous and irreversible deformation of a MEMS structure when submitted to a high temperature step. Plastic deformation is of particular concern in materials with low melting temperatures such as Al or most Al-alloys.

Chapter 4

Modelling Approach and Design Aspects for the Optimization of the Dynamic Characteristics of RF MEM Switches

4.1 Introduction

Accurate modelling of the electromechanical behaviour of RF-MEMS devices is an essential step in order to predict not only their mechanical characteristics, but also to guide the design of optimized devices by taking into account the trade-offs arising from device specifications both in the mechanical and electrical/electromagnetic physical domain. The numerical modelling work performed in this thesis had the main goal to provide a modelling procedure, able to perform static, modal and dynamic simulations. In addition we focussed on the identification of the main parameters influencing the dynamic behaviour of the devices.

4.2 The Numerical Modelling Process

In order to perform a complete numerical simulation of an RF MEMS device, such as switches or a varactor, a combined analysis in the mecahnical and electrical fields as well as time and frequency domains has to be performed. Typically the complete modelling of a RF MEMS device is performed in three steps, starting with a static analysis, followed by a modal analysis and finally by a dynamic analysis. To perform this type of simulations a multi physics domain approach is necessary. All the numerical analyses presented in this thesis have been obtained with ANSYS Multiphysics (version 11), which is an extremely powerful software tool for performing Finite-Elements -Model (FEM) simulations in multiple physical domains.

4.2.1 Example structure

In the following description of the numerical modelling process a RF MEM shunt switch fabricated with the FBK technology will be used as an example case. Details on the fabrication process can be found in the previous chapter. Fig 4.1 shows the layout of the shunt switch, characterized by a central square plate stiffened with a thicker frame through CPW layer and suspended with meander type springs in order to mitigate the effects of residual stress on the effective stiffness of the suspensions [5]. The size of the centeral plate structure is 220x220 μm, the thickness of the meander springs is about 1.8 μm while the central part reinforced with the CPW frame is around 4.8 μm thick. The dimensions of the vent/release holes are 20x20 μm^2.
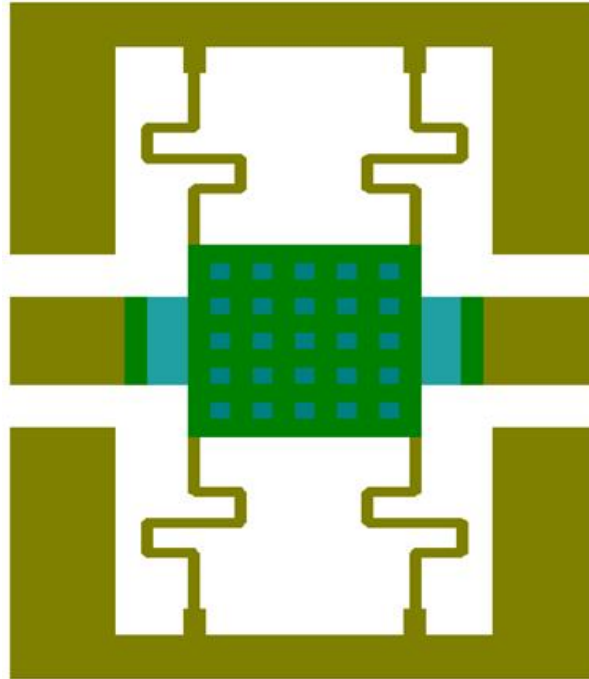
Figure 4.1: Layout of the RF MEM shunt switch used as example for the description of the numerical approach.

4.2.2 Material Properties and Fabrication Process Parameters

The first step in the model construction consists in the definition of the material parameters used by ANSYS.

A wide range of materials are typically used for the construction of MEMS devices. Since their mechanical properties strongly influence the characteristics of the devices, an accurate evaluation and selection of the materials and their compatibility is necessary, both for optimum dynamic performance of the switch design and for higher reliability of the device.

Monocrystalline silicon, one of the most used material for MEMS devices, is a mechanically strong material that does not show creep or plastic deformation and is well-suited for mechanical elements undergoing bending. Polysilicon has similar properties and like silicon it is compatible with most micromachining processes. Other commonly used materials are sputtered

thin films of various metals, such as aluminum, tungsten, platinum and gold. These are mainly used as electrical conductors.

Also dielectric layers like silicon dioxide and silicon nitride are extensivley used in the fabrication of MEMS. Both of them have traditionally been used for electrical and thermal isolation, masking, and encapsulation. Because of its chemical inertness and low intrinsic stress , silicon nitride is generally preferred over silicon dioxide. Silica glass is also increasingly used in MEMS technology. Other materials used primarily for electrical isolation are aluminum oxide and polyimide.

The diversity of materials usually integrated together in MEMS devices is also likely to generate different failure modes from traditional micro-electronics or from mechanical systems, due to matching problems between their different mechanical properties. Only a few studies have been conducted on the long-term mechanical stability of the materials used in MEMS devices, a crucial issue as the materials and the processes that are widely used in micro electronics technologies are now required to fulfill different functions for MEMS devices. As an example one can take the case of polysilicon, a material commonly used for MEMS devices, but for which reliable mechanical data are not available for devices that have dimensions on the order of microns. Properties such as Young modulus and yield strength are uncertain because the device size often approaches the grain size of the material. There are simply insufficient grains in the substrate for random orientation to cause the material to be isotropic. The mechanical properties of micron-size polysilicon largely depend on the individual production lot and any test measurements would result in material properties data with large deviations. The actuator types found in optical MEMS components, such as lenses, mirrors, optical switches, beam splitters, gratings, etc. often rely upon the electrostatic deformation of a mechanical membrane, beam, or cantilever to manipulate the optical beams. Micromirrors

designed to be used as optical switches, displays and scanners are examples
of this. They are made with thin metal films of aluminum and polysili-
con. The main problem associated with fabricating membrane, beam or
cantilever mirror structures with metal or dielectric thin films has been
the magnitude and variance of the stress generated in the materials during
fabrication. When the mirrors are released, the internal stress causes them
to bend in a concave or convex manner, depending upon the stress state
(whether it is tensile or compressive) within the material. For micro opti-
cal applications where surface flatness and uniformity are paramount, this
problem is a severe impediment to the development of these devices. Non-
theless Al is an intersting material for MEMS devices including switches
because of its low density. By using Al instead of gold the switches could
be intrinsecally faster just because a smaller mass accelerates faster. While
this may sound very intersting one has still to keep in mind that materials
cannot easily be substituted in a process due to the many compatibility
issues involved in the architecture of a process. In addition to the struc-
tural materials mentioned there has been an increasing interest in the use
of amorphous and diamond-like carbon films and diamond structures in
MEMS devices. The large wetting angles, low surface energies and small
adhesion forces of carbon films make them good candidate materials for
reducing stiction and friction forces at MEMS interfaces. In addition there
is some ongoing research activity investigating the application of carbon
nanotubes in the fabrication of MEMS. These could be useful in improving
the RF performance of the switches as well. It has been shown [28] that a
Au surface coupled with a Au/MWCNT (gold coated multi-walled carbon
nanotube structure) has the ability to sustain millions of switching cycles
under typical electrical loads for current MEMS switch devices, e.g. 4V,
1 to 10 mA, with a low contact force in the order of 1mN. This is an im-
portant observation and lays the foundation for the application of carbon

nanotube structures for electrical contact applications. The surfaces developed in these works used an approximate 500 nm thick gold coating on a stainless steel ball surface and a MWCNT surface. The contact resistance across the interface was used as the parameter for determining the failure modes of these surfaces. This and other works show that the contact force has an important effect on the reliability of the switches. As far as this thesis is concerned, only a limited consideration could be given to these sugges tionsbecause the inclusion of exotic layers like MWCNT in the in house technology is impossible at the moment.

As an alternative to gold, aluminum or copper instead of gold could be helpful in reducing the switching time because of their lower density [39]. While Aluminum would provide the strongest reduction in weight it is difficult to use it as structural materila in FBK fabrication process. the other side Copper is still 2.2 times more lightweight than gold, therefore providing a substantial mass reduction, which could improve the switching times (for the same design and material thicknesses) in the order of a factor 1.5 (this is the amount of reduction of the natural frequency of the structure, which is $\sqrt{\frac{m}{k}}$, see chapter 3). The advantage in this case would be the fact that a substitution of the gold layer with a copper layer is much simpler as both can be deposited with the same process, i.e. the electrochemical deposition. Anyway even if this case seems simpler to be implemented, still a new material poses new challenges, for example in the fabrication of contacts, since copper, unlike gold, is not a noble material.

The main structural material of the FBK MEMS switch process is gold. Most simulation runs have been done with this material. In addition also Copper, as an alternative material, has been considered. Table 4.1 summarizes the material properties that have been used for the simulations.

The material properties were defined within ANSYS preprocessor, by choosing a linear isotropic material model. Inside this model, the values of Young

modulus, Poisson's ratio and density were provided for each material composing the structure to be simulated.

In this thesis we used, where available, measured data of the materials used in the process and refined them in order to achieve a good matching with experimental data on a large variety of devices and structures.

4.2.3   Model Construction and Meshing

Once the material properties have been introduced the next step is to construct the model:

- one very straight forward way consists in importing the 3-D model of the device with the help of the software MEMS PRO. MEMS PRO is a layout editor tool that allows the transfer of the layout data of a particular device to ANSYS. As the layout data contain only the 2D information of a given layer, the thickness has to be added in order to obtain a full 3D model in MEMS PRO. This was done for each layer , i.e. the thin gold layer, the CPW layer and the spacer.With these additional data a 3-D model is created and and saved into a MAC format file, which is imported in ANSYS. The advantage of this approach lies not only in the time saving offered by an automatic procedure, but also in the perfect match between the designed device and the simulated one.

- The second possibility to generate the device geometry, used in this thesis work in particular circumstances, consists in creating the geometrical model directly in ANSYS. This can be done manually with the commands available in the model construction window of AN-SYS or by using the machine commands. In the latter case simply a

command list can be written in a Wordpad or Notpad file and then imported into ANSYS. Even if this method is more time consuming and requires a good knowledge of the building commands of ANSYS it offers a much higher control on the device geometry and can be mandatory in particular circumstances.

Once the device geometry has been defined a suitable mesh has to be defined. In a FEM analysis the mesh defines the elementary basic elements cells on which the equation's are discretized and therefore the meshing has a strong influence on the precision of the solution provided. ANSYS provides different ways to mesh a structure, which depend also on the particular domain used. It is intrinsic to the FEM approach that the more refined the mesh is the more accurate will be the solution obtained. The next step in the preparation of the simulation consists in the definition of the appropriate boundary conditions. In applying the boundary conditions also the symmetry planes of the structure must be considered and can be exploited to contain the computing effort. If during the geometry definition it has been decided to exploit the symmetry conditions of the structure and only a quarter or a half of the structure has been designed, now these symmetries have to be considered very carefully during the application of the boundary conditions, because a wrong definition at this step can invalidate the whole simulation.

4.2.4 Static Electromechanic Model; Determination of the Pull-in / Pull-out Voltages

As discussed in chapter 3 in the case of electrostatic actuators, when a voltage is applied to the actuation pad, an electrical field is created be-
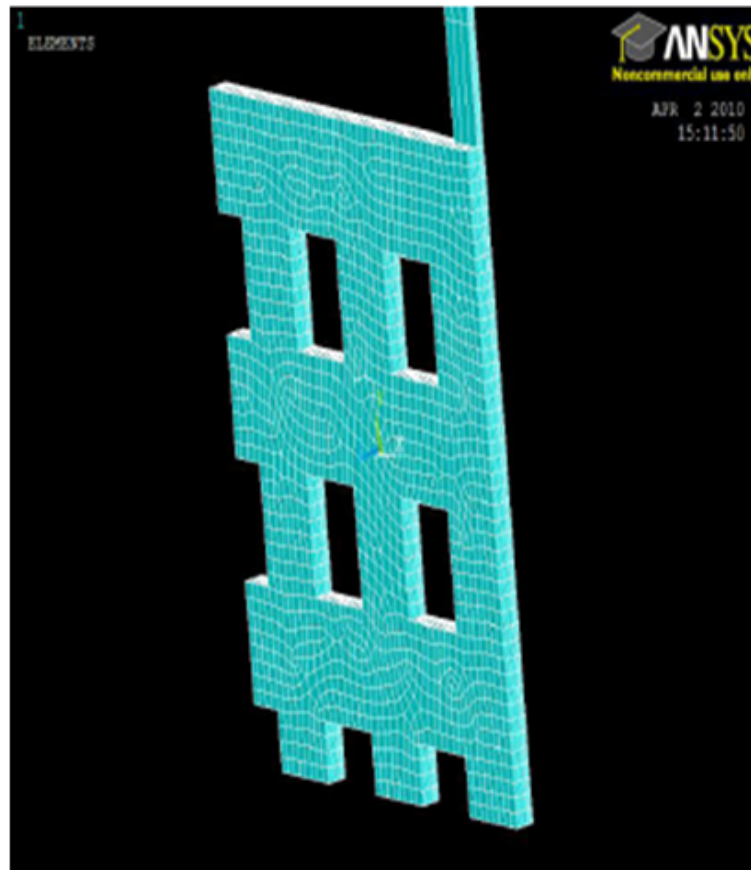
Figure 4.2: Meshed device with symmetric conditions applied and fixed domain defined.

tween the upper electrode and the pad at the bottom, which attracts the mobile electrode till the instability point is reached and pull-in occurs. The electromechanical model is used in order to estimate pull in voltage and pull out characterestics of the device under investigation. In this kind of simulation the 3D models were typically meshed with a 2-um triangle mesh element is used. In order to save machine resources and computation time all possible symmetry conditions were normally exploited, e.g. in most cases only half of the structure if not only one quarter was modeled. The electric field is introduced with the TRANS126 element, which in ANSYS represents a transducer element that converts energy from the electrostatic domain into the structural domain (and vice versa), while also allowing for

energy storage. This element fully couples the electromechanical domains and represents a reduced order model suitable to be used in structural finite element analysis as well as electromechanical circuit simulation. The TRANS126 element has up to four degrees of freedom at each node: three degree in translation in the x, y, or z direction and one degree for the electric potential (VOLT). Fig 4.2 shows the meshed domain and the symmetry planes. In addition the boundary condition for the TRANS126 element must be considered. These TRANS126 elements are created by issuing the proper ANSYS command (EMTGEN) after selecting the nodes at the bottom side of the mobile electrode see Fig 4.3. The proper selection of these nodes is crucial for the accuracy of the model. By using suitable commands able to select the nodes based on their coordinates, this step can be programmed in ANSYS as a function of the geometry parameters defining the solid model. After creating the TRANS elements at the bottom part of the mobile electrode, the solver can be launched. The computing time strongly depends on the number of elements that have been created. One has to keep in mind that for the smaller load steps the longer the computational time. Therefore it is advisable to check if the model construction is correct by making a test run using a larger load step, before reducing the load step in order to obtain a more precise result. During the first static simulations of different structures using the nominal geometrical values and the material properties of gold found in the literature it was found that the extracted pull-in voltage resulted in much lower values than the expected/measured one. There are different possible uncertainties that contribute in various ways to this discrepancy and all of these have been addressed in the attempt to refine the simulation model:

- The value of the Young modulus: clearly higher E values generate higher pull-in values. As a first tentative a value of the Young modulus of gold taken from the literature has been used. This value is the one
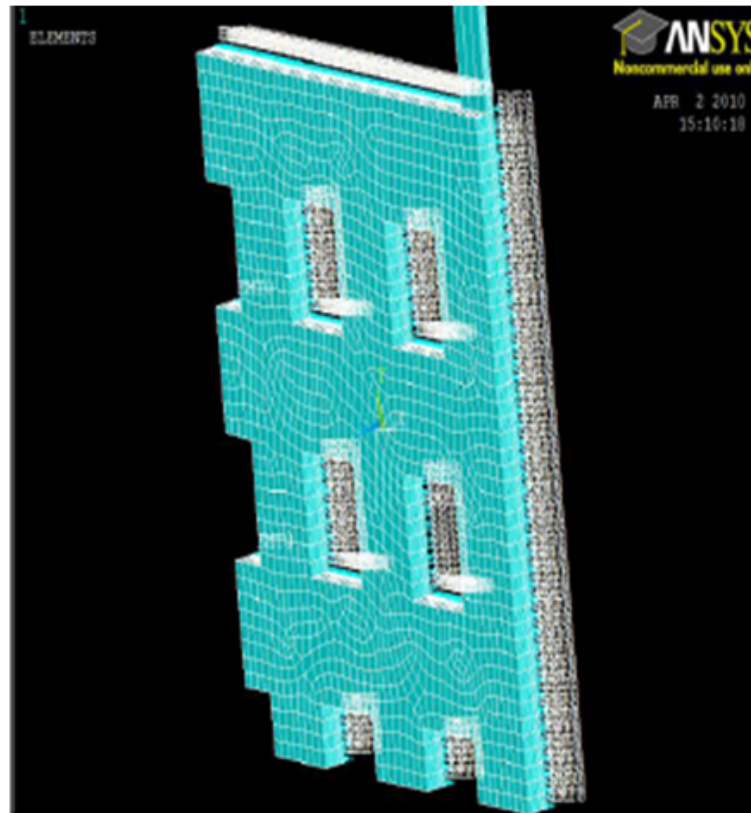
Figure 4.3: Screenshot of the view of the TRANS126 elements of a structure.

found for pure gold and may be in defect both because a thin film generally exhibits a higher Young modulus and because FBK thin film is not actually made of pure gold but is very likely an alloy with low traces of chromium, which enhances the mechanical properties of the layer. Hardness measurements performed later on showed that the Young modulus of the plated gold layer of the FBK process is roughly 20% higher then pure gold. Of course this increase alone cannot account totally for the discrepancies observed, as the pull-in voltage is roughly proportional to the square root of the Young modulus, see chapter 3.

- The value of the initial gap: from chapter 3 it is clear that by decreas-

ing the initial gap, the pull-in voltage decreases. With respect to this the main difficulty is that the accurate estimation of the value of the gap with no bias is not a simple task. It is known that the nominal value of the gap that corresponds to the spacer height on a blank wafer is an overestimation because the finite height of the actuation pad reduces the actual spacer height in the gap. If the photo resist used as a spacer would behave as a perfect liquid the gap height would be the nominal value minus the actuation pad height. In practice things are not so simple as the photo resist to a certain extend tends to be more conformal. Unfortunately there is no simple and obvious method to measure the actual value on a finished device. An indirect estimate, based on height measurements during the fabrication of the devices, indicates that the actual gap height is half way between the nominal value and the value obtained by subtracting the actuation pad height. As in the case of the Young modulus at first order the pull-in voltage is proportional to the square root of the gap height, which makes this parameter less sensitive to errors even if the absolute uncertainties on the parameter may be high.

- The thickness of the gold layer: The actual value of the thin gold layer thickness determines the mechanical stiffness of the structures. This value is particular important for those structures which undergo flexure as the stiffness to flexure of a beam is very sensitive to thickness variations. Therefore this is an issue in case of cantilever beams, while it affects much less the clamped clamped beam structures.

- The intrinsic stress: it is well known that most MEMS fabrication techniques induce a high internal stress in the materials, which finally produces high pre-stress values in the final mechanical structures. The internal stress is mainly due to temperature variations during the fab-

rication, especially in case of several layers of materials with different coefficients of thermal expansion. This pre-stress strongly affects the behavior of the system and must therefore be included in the model. In case of the gold structures built by FBK an initial stress value of 150MPa has shown to be in good agreement with most experimental findings.

All the above mentioned corrections have been included in the parameter definition file and the material properties file. The thickness of gold layers used for simulation are respectively 1.8 and 3.8 μm BRIDGE and CPW respectively. Table 4.1 shows the material properties that have been used for the last simulations, while Fig 4.4 and Fig 4.5 show the deformation map of the structure after pull-in and the displacement vs voltage curve of the central point of the structure. Before including the appropriate pre-stress and the corrected thickness of the structure taken from the inline measurements performed during device fabrication, the simulated pull-in voltage was about 3 V. After including these, the pull-in voltage increased up to 4.6 V, i.e. a value 53% higher.

Young modulus of Gold [GPa]	Density of Gold [gcm^3]	Poisson ratio of gold
80	19.3	0.44

Table 4.1: Principle material properties used for in the numerical simulations.

4.2.5 Modal Analysis

A prerequisite for a full transient dynamic simulation is the knowledge of the Eigen frequency spectrum of the structure. This is obtained with a so called modal analysis, which allows ANSYS to calculate the natural frequencies and mode shapes of the structure under investigation. This simulation essentially calculates the response of the structure to an external
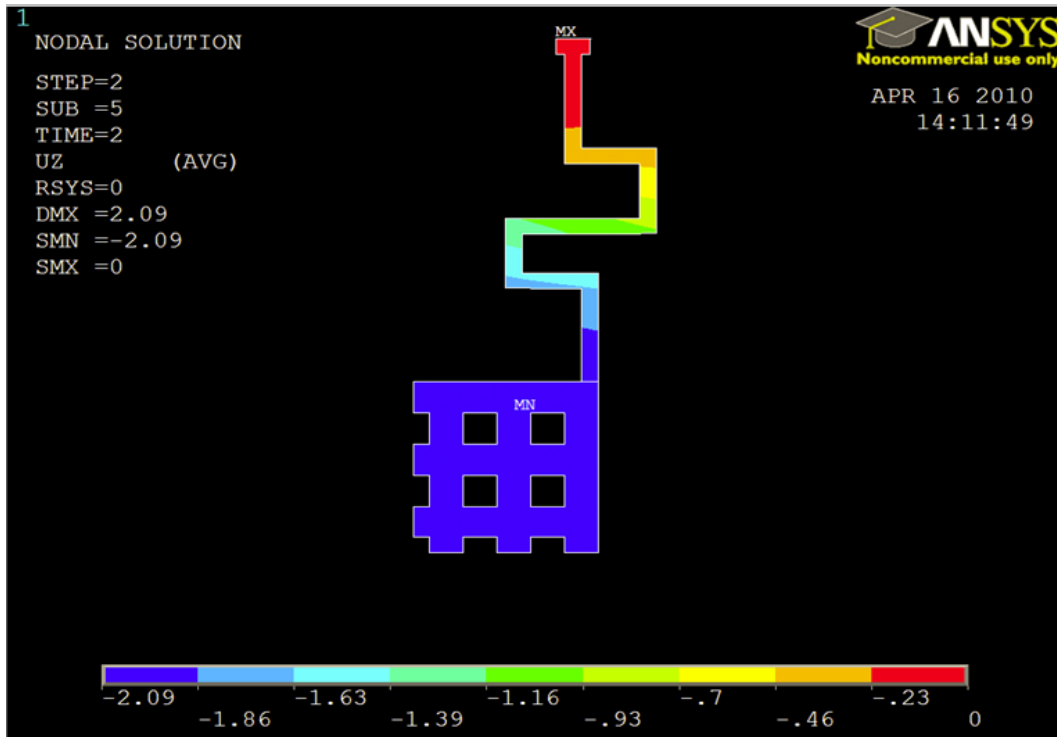
Figure 4.4: ANSYS plot showing the deformation of the structure after reaching pull-in.
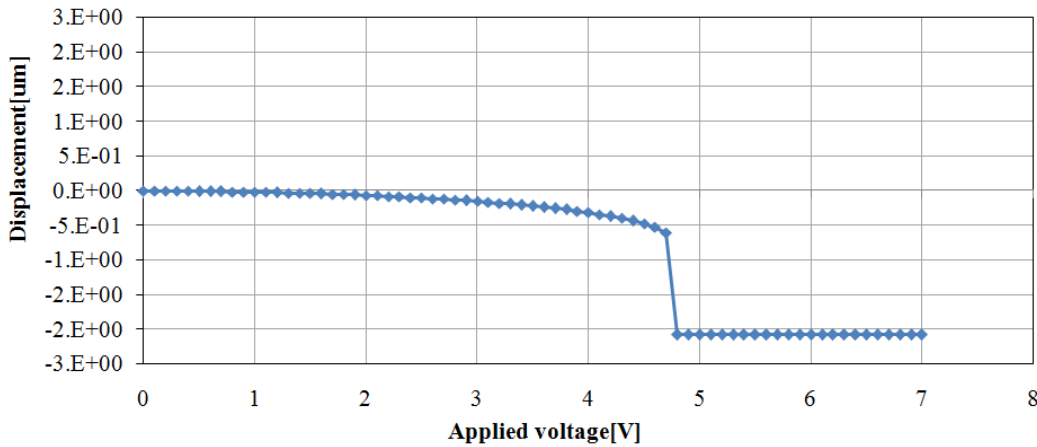

Figure 4.5: Central point displacement vs. applied voltage obtained by ANSYS simulations. An abrupt change of displacement occurs at the pull-in voltage.

periodic excitation.

Typical outputs of a modal analysis performed by ANSYS are shown in

Fig. 4.6 and Fig.4.7. The first image shows the first mode of vibration of the structure, which corresponds to an up and down movement of the central plate. The second mode, i.e. the one with an resonant frequency immediately higher than the fundamental mode, corresponds to a bending-like movement.

4.2.6 Dynamic Model Based on the Squeeze Film Method of ANSYS

For the full transient dynamic simulation also the air flow around the structure must be considered. This implies the setting up and the solution of the Navier-Stokes equations, which results quite demanding in terms of computation power. Fortunately in addition to the possibility of a complete solution of the Navier-Stokes equations the ANSYS FEM tool offers a simple and compact model for fluidodynamic problems based on the linearized Reynolds equations that avoids simulating the whole FLUID 3D domain as in case of the Navier-Stokes equations and is suitable for problems like those related to the air damping. This simplified approach is included in the FLUID136 element, which allows modelling the viscous fluid flow that occurs in the gap of MEMS switches. The element is essentially based on the linearized Reynolds equation familiar from lubrication technology and previously recalled in chapter 3 . However it is not in the suitable form for FEM discretization yet.

$$\frac{g_0{}^3}{12\mu_{eff},gap}\left(\frac{\partial^2 P}{\partial x^2}+\frac{\partial^2 P}{\partial y^2}\right)=\frac{h}{P_0}\cdot\frac{\partial P}{\partial t}+v \tag{4.1}$$

Here g_0 is the gap thickness and μ_{eff} is the effective viscosity for the air gap, P is the pressure,P_0 is the operating pressure , and v is the vertical plate velocity that can be the expressed as a function of x and y.

As the FLUID136 element models the viscous fluid flow behavior in small gaps between fixed surfaces and structures moving perpendicular to
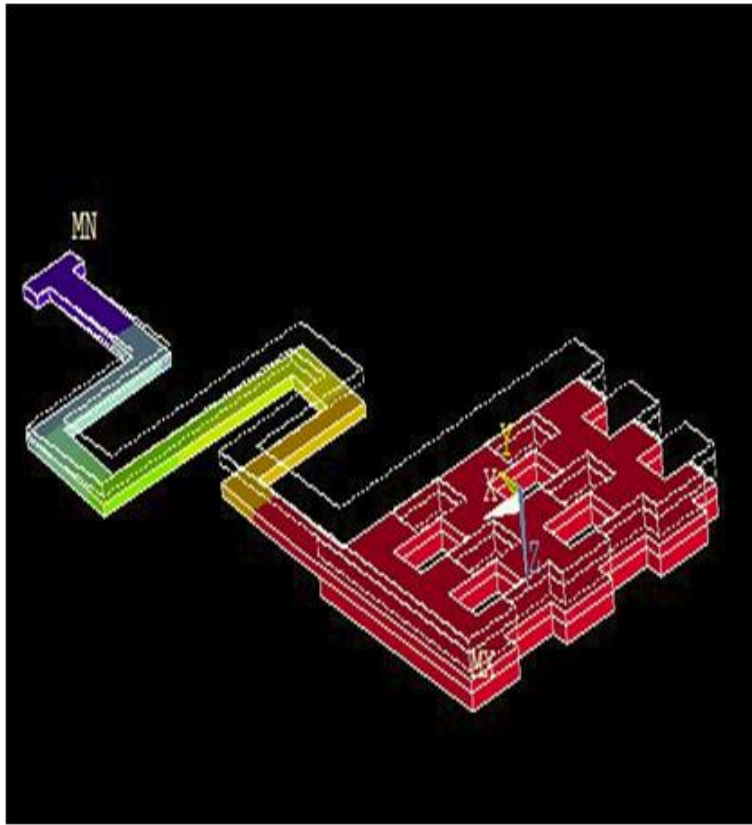
Figure 4.6: Deformation corresponding to the first mode vibration.

the fixed surfaces, the element can be used to determine the stiffening and damping effects that the fluid exerts on the moving structure. The element behavior is based on the Reynolds squeeze film theory and the theory of rarefied gases. As such, it is limited to structures with lateral dimensions much greater than the gap size. In addition, the pressure change must be small relative to the ambient pressure and any viscous heating is neglected. Therefore the FLUID136 element is particularly suitable for modeling squeeze-film effects in microstructures.

The FLUID138 element models the viscous fluid flow behavior through short channels (i.e., holes) in microstructures moving perpendicular to a fixed surface. The FLUID138 element can be used in conjunction with the FLUID136 element to determine the stiffening and damping effects that
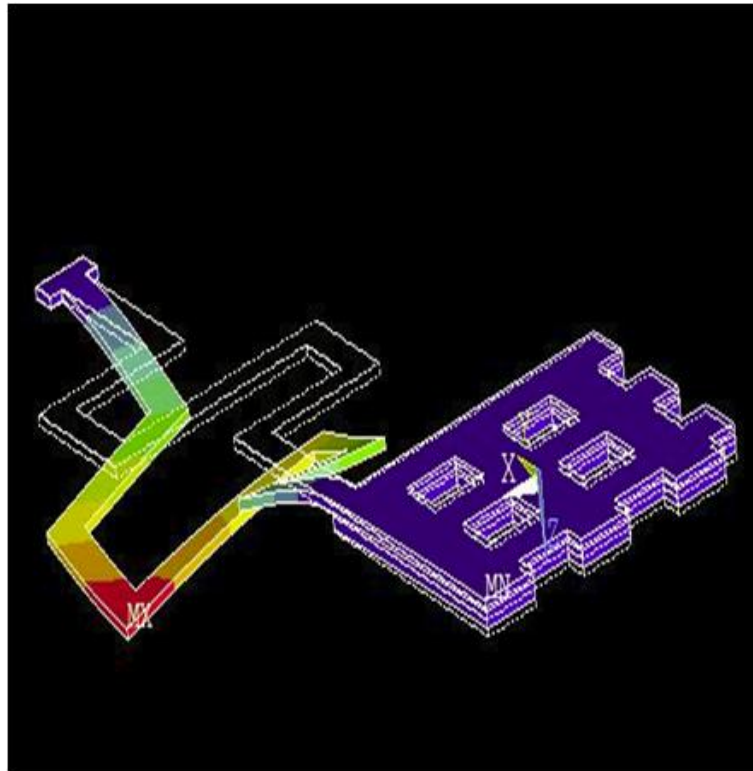
Figure 4.7: Deformation of the structure corresponding to the second mode of vibration as obtained by ANYSY modal analysis.

the fluid exerts on a moving perforated microstructure. The FLUID138 element assumes isothermal flow at low Reynolds numbers. The channel length must be small relative to the acoustic wavelength, and the pressure change must be small relative to the ambient pressure. The FLUID138 element accounts for gas rarefaction effects and fringe effects due to the short channel length as well.

For most of the simulations performed in this thesis work the pressure used was equal to the atmospheric pressure (0.1 MPa) in which case the mean free path is equal to 65 nm and the viscosity is equal to $1.854*10^{-5}Pas$. For the transient dynamic simulation both fluid elements are used for the description of the thin air film in the gap and in the vent holes, while the structure is modeled with the solid elements cited above. In addition the
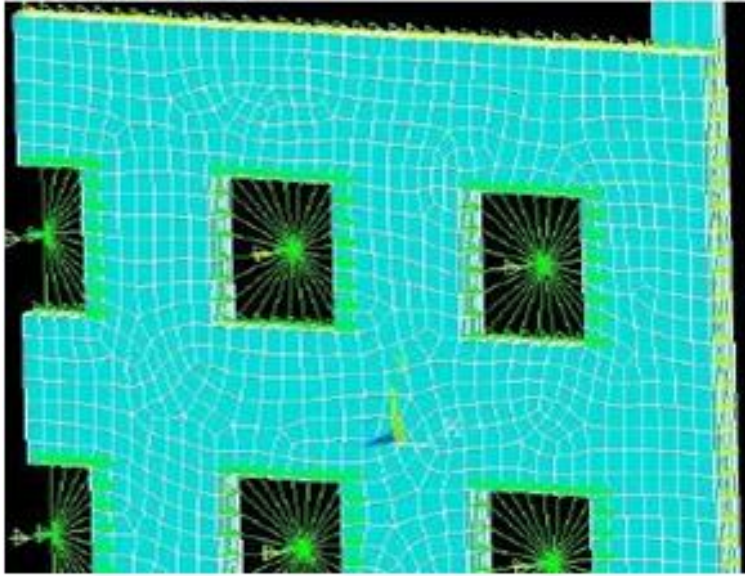
Figure 4.8: Screenshot of the ANSYS graphical interface showing the fluidic domain and the pressure as applied at the edge of the sample structure.

extracted Raleigh damping coefficients α and β , respectively mass damping and stiffness damping, are necessary too.

Regarding the boundary conditions the pressure is considered equal to the ambient pressure and the viscosity and the Knudsen number are equal to the values mentioned above. The pressure is applied at the edge of the structure as shown in Fig 4.8 together with the voltage.

After extracting all the parameters necessary for the transient dynamic simulation the simulation has been performed assuming a 4 V pulse applied. From the computational point of view a transient dynamic simulation is a much more complex simulation, which makes use of far more computer resources. These kind of simulations can also suffer of convergence problems. These issues have been overcome by explicitely setting the convergence thresholds and the maximum number of iterations. Sometimes it was also necessary to include large-deflection effects in both static and full transient analysis. Fig 4.9 and Fig. 4.10 show the applied voltage

pulse and the displacement versus time obtained by the transient dynamic simulation for a 4 V pulse applied.

4.3 Specific Case Studies

Here after six case studies are presented that have been performed with the final aim to improve the dynamic behavior of RF MEM switches. To this purpose various parameters influencing more or less the dynamic characteristics have been studied separately either on realized devices or on model structures. The parameters taken into account are:

- Gap height;

- Applied voltage;

- Building material;

- Gas pressure;

- Shape effects;

- Constrained movement by mechanical stoppers.

4.3.1 The Dependence on the Gap Height

The air gap height, between the multi-layer silicon membrane and the lower electrode, determines the capacitance of an non actuated RF MEMS switch. As discussed in chapter 3 this capacitance determines also the actuation voltage. The air gap height is therefore one of the key factors in RF MEMS switch design. Reducing the gap height, will increase the speed of the switch simply because the travel distance of the mobile electrode is shorter and at constant acceleration, i.e. at constant bias voltage, less
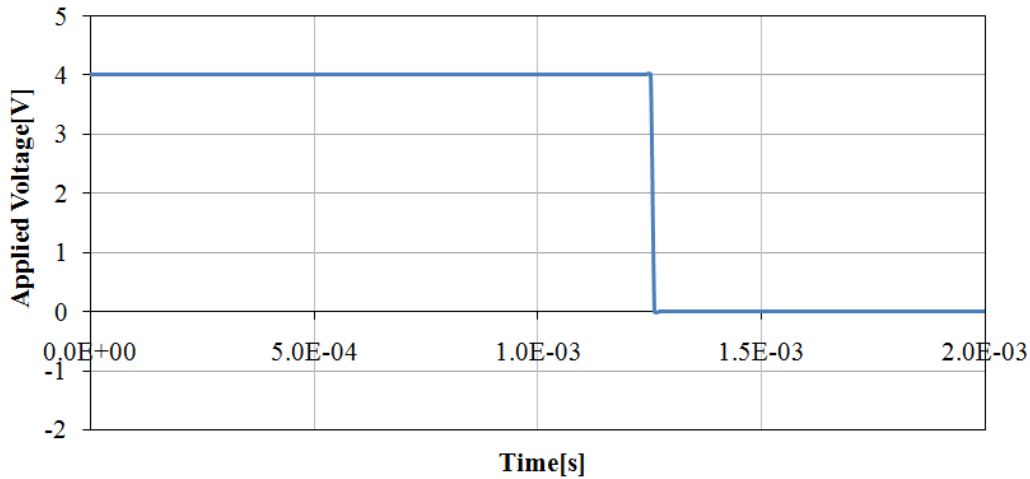
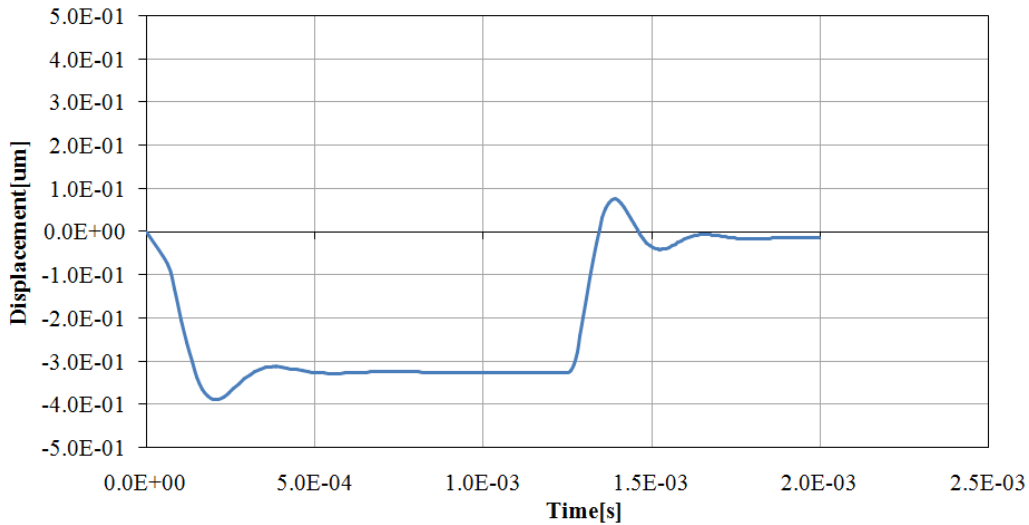Figure 4.9: The voltage pulse applied for the simulation of the transient behavior.

Figure 4.10: Displacement versus time obtained by the transient dynamic simulation of the sample structure with 4 volt applied voltage pulse lower than pull in.

time is necessary to cover the shorter distance. The simulation presented next has been done on the layout of Fig 4.1. As suggested by the basic mechanical considerations also the numerical simulation shows this dependence.

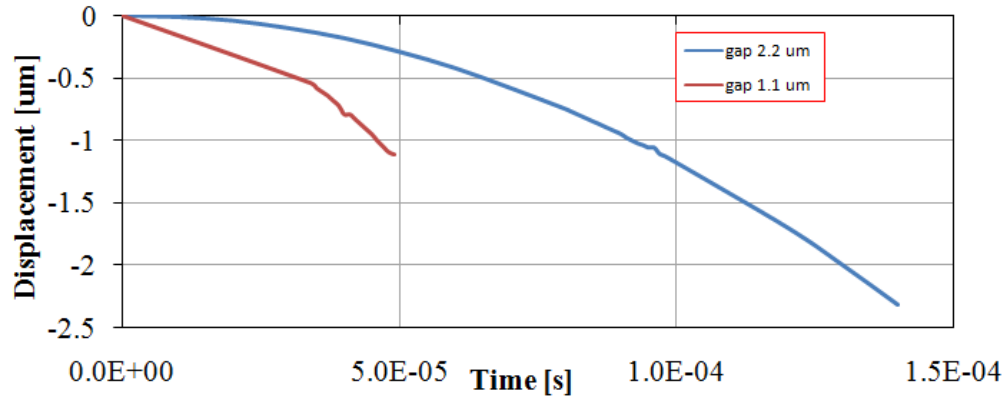Fig 4.11 shows the graph of the analytical calculation for different gap

Figure 4.11: Transient dynamic behavior of the displacement obtained by analytical calculation in case of two different gap heights for an applied voltage of 5 volt without considering the damping effect.
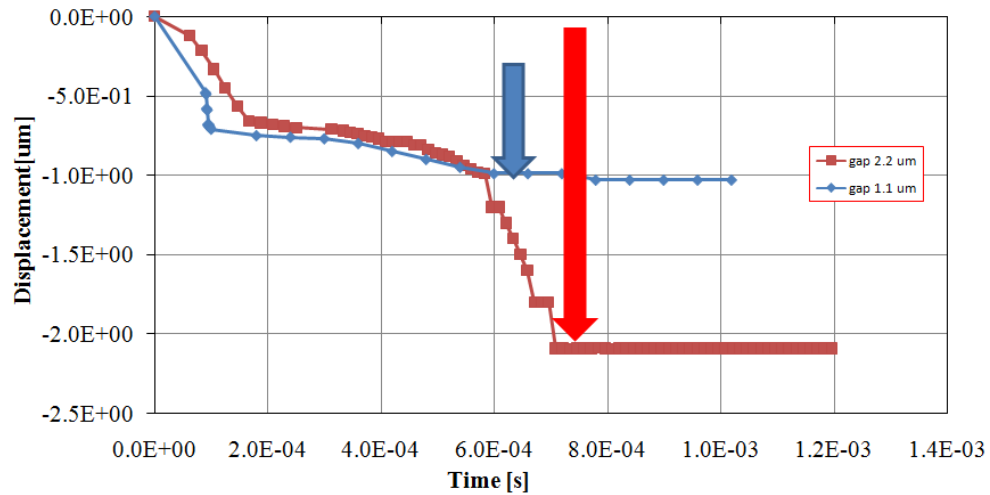

Figure 4.12: Simulated transient dynamic behavior of the displacement with two different gap heights with an applied voltage of 5 volt.

height and Fig 4.12 shows the result of the numerical simulation with two different gap heights with an applied voltage 5 V. A comparison between analytical and numerical results is shown in Fig 4.13 in case of one gap height. The analytical calculation has been based on the equation of motion for a body subjected to a constant acceleration $x = \frac{1}{2}at^2 + v_0 t$,here
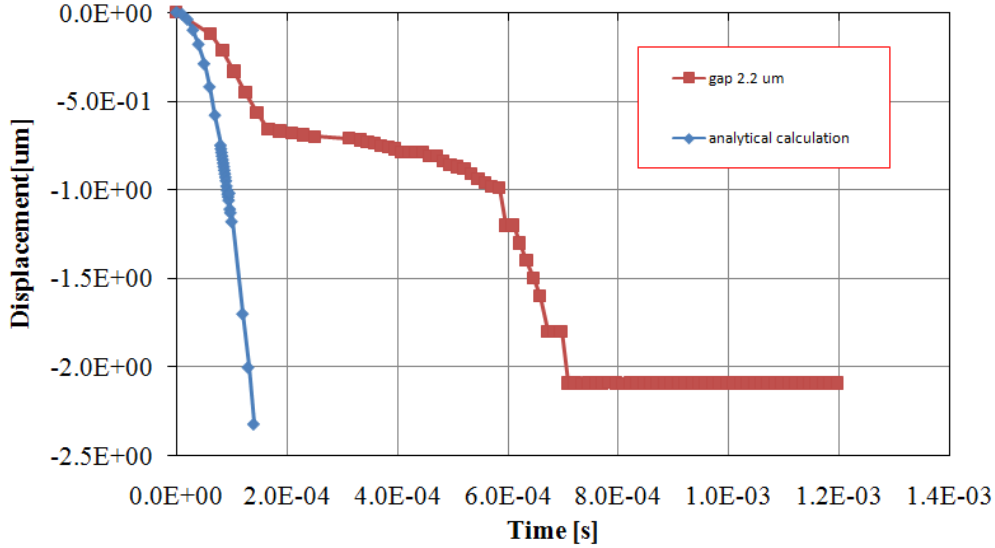
Figure 4.13: Comparison between simulated and calculated dynamic behavior of the displacement in case of a 2.2 μm thick gap.

v_0 is the initial velocity, t is the time, is the displacement and α is the acceleration,which in turn can be expressed by the $a = \frac{\varepsilon_r \varepsilon_0 A V^2}{2mg^2}$ [8], where A is the area, V is the applied voltage , m the mass , ε_0 is the free space permittivity , and g is the gap thickness . In case of a 2.2 μm gap height it is clear that the simulated displacement versus time curve (Fig. 4.12) is characterized by two regimes: in the first part of the transient the displacement has a parabolic shape, as expected for a body subjected to constant acceleration, while in the second part the displacement is strongly delayed by the squeeze film effect. This general aspect of the curve is present also in the case of the 1.1 μm gap height , but in this case both the transition point from the motion under constant acceleration to the strongly damped motion and the time when the electrodes come at rest are reached earlier. The transition point between the two regimes happens at laest 50 μs , while the endpoint of the motion is reached about 350 μs earlier.

4.3.2 The Dependence on the Applied Voltage

Another mean to reduce the switching times of RF switches is the use of higher applied voltages. According to the discussion of chapter 3, if voltages significantly higher than the pull-in voltage are applied a proportional reduction of the switching time is achieved, because in this case the mobile parts of the switch accelerate faster and therefore close the gap faster. Of course this applies only in the closure cycle, while the opening of the switch is still governed by the spring force alone.

A much higher velocity of the mobile electrode has also some potential drawbacks. One of these is the contact bouncing that results from the elastic behavior of the switch and which prevents a stable closure until the oscillations have been damped. Applying two voltage pulses can mitigate this inconvenience. In practice by lowering the applied voltage some time before closure is reached the impact velocity of the mobile electrode is reduced. An even more effective way to control this phenomenon is to operate the switch in charge control mode instead of voltage control mode. The charge control mode allows for full control of the movement of the switch throughout the whole gap.

Both these methods require a more complex control electronic, but could be effective not only in reducing the switching time but also in reducing the impact damage on the electrical contacts. Again, simulations with different applied voltages have been done on the same device structure of Fig 4.1. Fig 4.14 shows the results of the simulations with different applied voltages, while Fig 4.15 and Fig 4.16 respectively compare the results of the simulations with those obtained by analytical calculation. It can be clearly seen that all curves have a first very steep part that corresponds to a constant acceleration motion where the damping doesn't play a significant role and a second part where squeeze film damping clearly manifests.
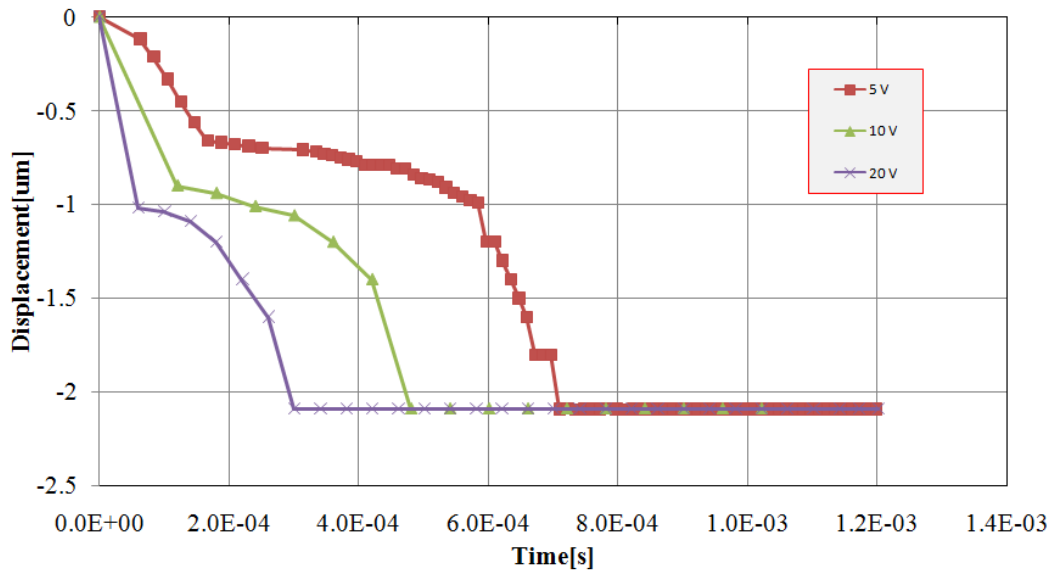
Figure 4.14: Displacement vs time for different applied volatge as obtained by numerical modelling.

The time necessary to close roughly scales according to the ratio of the pull-in voltage and the applied voltage. These curves also show that the squeeze film effect lengthens the closure time of a switch approximately by a factor 2.5, which implies that a careful design of the damping of the structure, e.g. optimized size and placement of the vent holes, can reduce the switching time by a considerable amount.

4.3.3 The Influence of the Building Material

As discussed in section 4.2.1 the material can impact on the dynamic behavior of a switch.Considering as instance gold and copper, a comparison of the simulated dynamic behaviours is shown in Fig 4.17, while in table 4.2 the main material properties of copper are reported (to be compared with those of gold, shown in table 4.1). By looking at the transient one immediately notices the big difference in the oscillation frequency of the
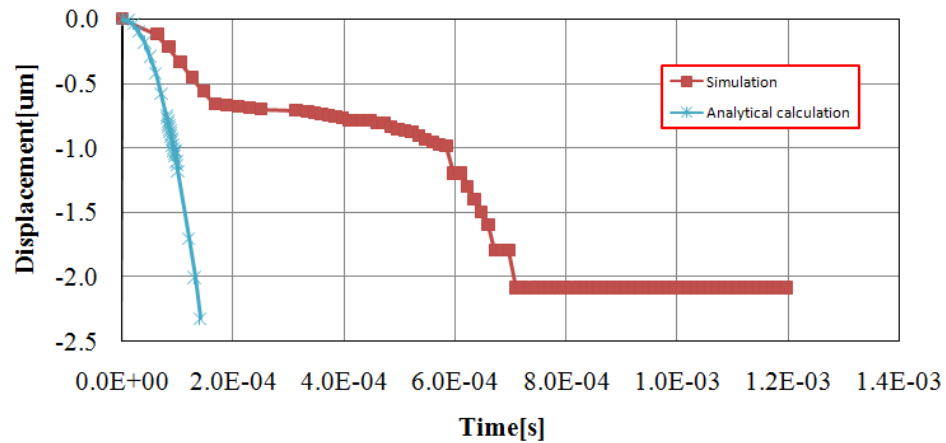
Figure 4.15: Comparison between simulated and calculated dyanmic behavior of the displacement for an applied voltage of 5 V.
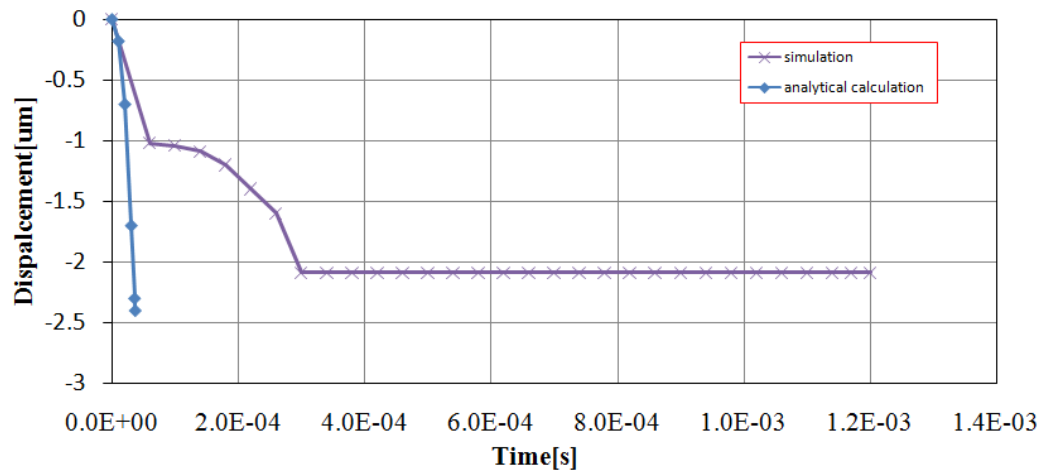

Figure 4.16: Comparison between simulated and calculated dyanmic behavior of the displacement for an applied voltage of 20 V.

damped oscillations of the structure. This reduction of the natural frequency of the structure by a factor of 1.5 is very close to the square root of the ratio of the densities of both materials, as expected from the simple cinematic calculations presented in chapter 3.

Young modulus of Copper $[GPa]$	Density of Copper $[gcm^3]$	Poisson ratio of Copper
128	8.94	0.34

Table 4.2: Principle material properties used for in the numerical simulations.
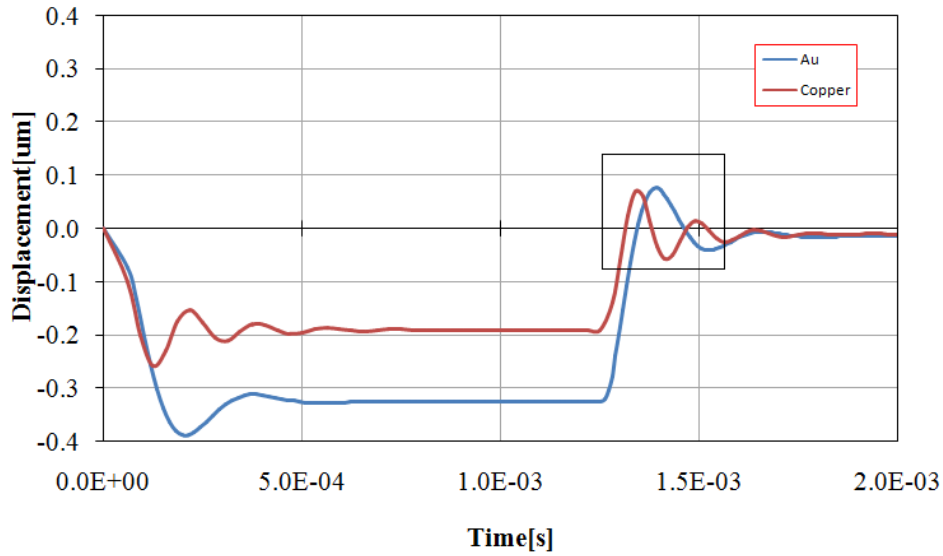

Figure 4.17: Graph of the vertical displacement obtained by the transient dynamic simulation of the same structure with two different materials.

4.3.4 The Dependence of the Switching Time on the Background Gas Pressure

As we have seen above for a given geometry the switching time is strongly influenced by the damping. The damping itself depends mainly on the type of gas and the gas pressure. The latter parameter strongly influences the viscosity of the gas and can therefore be a valuable means to modify the damping for a given design or to fine-tune it.

In order to have a first idea of the influence of the backpressure of the air on the dynamic behaviour two simulations are compared, one with air at standard temperature and pressure and one in vacuum, again performed on the structure described above. In Fig 4.18 the results of the two simulations

are compared. The simulations show that the system in the vacuum has a limited decrease in the response time if one looks at the first closure, while on the other hand the absence of a significant damping has the bad effect to introduce a very long ringing of the structure which in practice prevents its use as a switch.

From this rough result it is clear that a certain amount of damping is needed in order to have a fully functional device. From this simple test it is also likely that, as for most mechanical mass-spring systems or oscillators, there will exist an optimum degree of damping, i.e. the so called critical damping, where the best compromise between unhindered movement and suppression of unwanted oscillation is achieved.
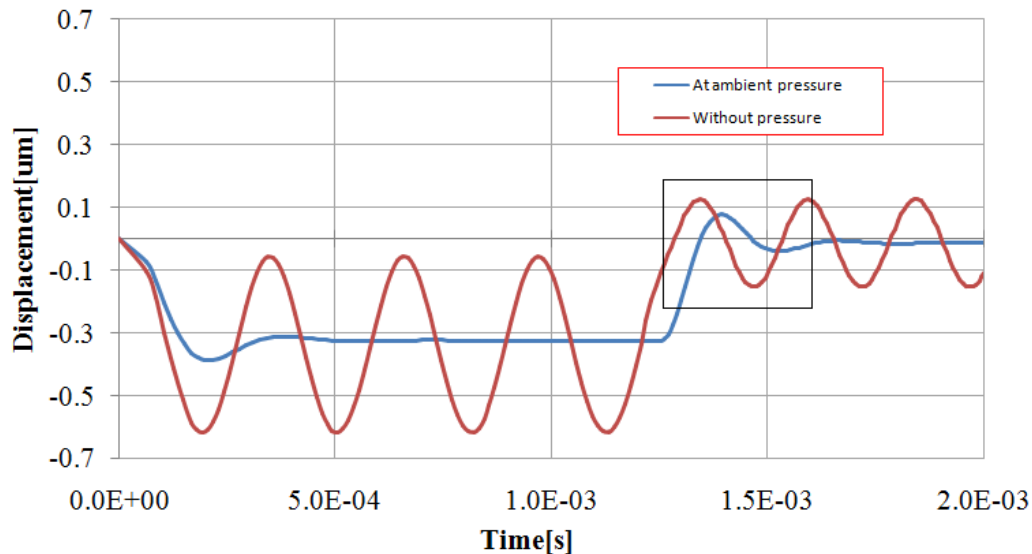

Figure 4.18: Displacement vs time of the actuation and deactuation transient simulated with 1 bar background pressure and without background pressure.

4.3.5 The Influence of Mechanical Stoppers

As shown in section 4.3.2 the squeeze film effect dominates the dynamic behaviour of the switch when the mobile electrode has covered roughly one third to one half of the initial gap height, depending on the applied voltage, because the air trapped in the gap cannot vent fast enough and due to its compressible nature hinders the free movement of the electrode. Therefore limiting the extend of the movement of the mobile electrode by stopping pillars that prevent the complete closure of the gap between the mobile electrode and the fixed electrode can be a mean to reduce the switching times. The main effect of the pillars is to guarantee a minimum size channel for the airflow and to reduce the excursion of the mobile electrode. The first aspect reduces the damping of the squeeze film and the second aspect reduces simply the travel length. In order to explore this approach, pillars have been added to the actuation pad in the layout shown in Fig 4.1. Fig 4.19 and Fig 4.20 show the structure without pillars and with pillars, while Fig 4.21 compares the displacement vs time curves obtained for the two situations for short time scale. In this circumstance two other devices made at FBK, one without pillar and the other with pillars (respectively labelled BO.0 and BO.7)have been studied. Both devices are capacitive shunt switches characterized by a stiff central plate suspended with straight suspension springs. The central plate is made of two 190x110 μm^2 symmetrical parts, connected to each other with very stiff beams. The pillars are obtained by isolating small squares of the polysilicon layer from the rest of the actuation electrode and adding on top of them even smaller squares in multimetal. In this way the pillar is twice as high as the actuation pad, thus creating a residual gap of 630 nm. The effect on the device performance is not only confined to the control of the gas dynamics during the closure cycle but it has also a distinct impact on other aspects
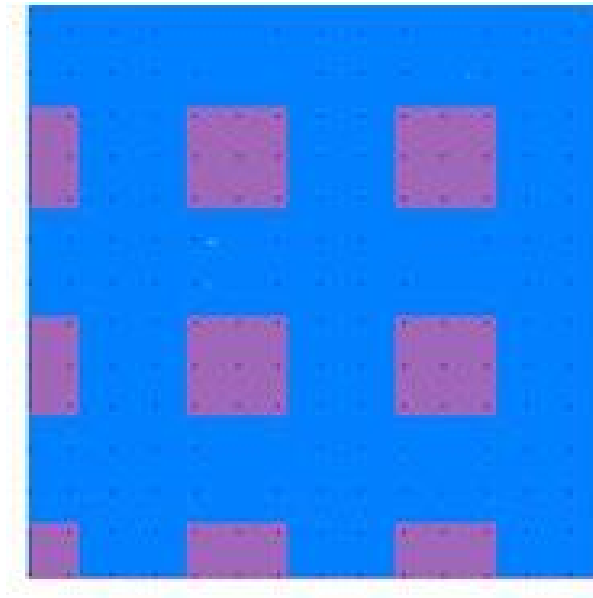
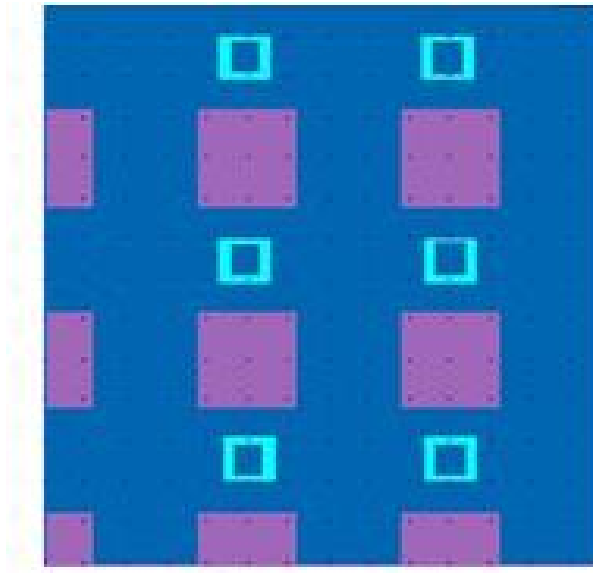Figure 4.19: Layout of the actuation pad witout pillars.

Figure 4.20: Layout of the actuation pad with the pillars added.

like charging and stiction, for which it was originally introduced. Fig 4.22 shows the micrograph of a finished device (BO.0) , while Fig 4.23 reports the layout of the two designs in order to show the difference in the actua-
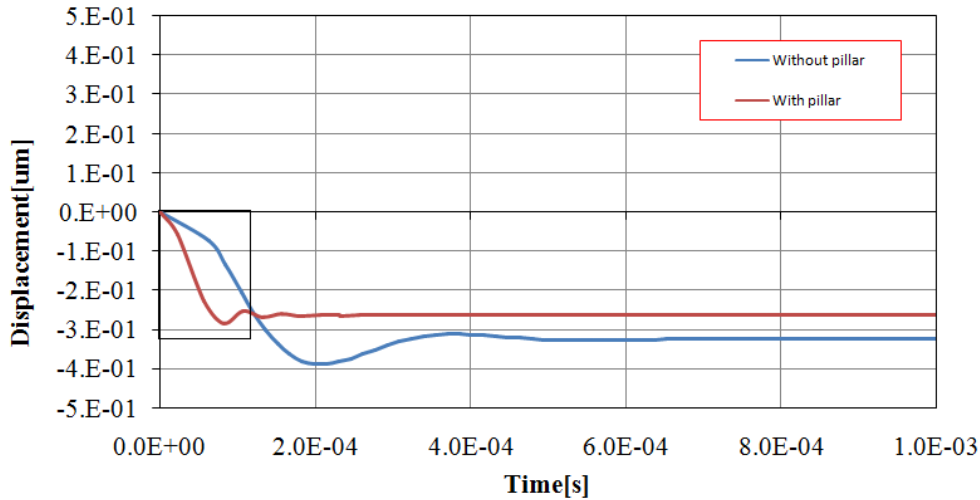
Figure 4.21: Comparison of the displacement curves obtained with pillar and without pillar for an applied voltage of 4 V (red line without pillars , blue line with pillars).Only the pull-in transient is shown. The difference in height of the rest position after pull-in is due to the pillar height.

tion pad layout. The fabrication process of the BO.0 switch is the same as described in the previous chapter. The simulated CV (capacitance voltage) characteristics is shown in Fig 4.24 as extracted from a static simulation. Fig 4.25 shows the result of a transient simulation for the structure without pillar and in Fig 4.26 this curve is compared with the response of the structure with pillars.

4.3.6 The Dependence on the Shape

The factors considered up to now impact on the dynamic behaviour of devices independently form the topology of the devices. In order to evaluate the influence of the bi-dimensional shape of the mobile parts of the device, starting from the sample layout presented at the beginning of the chapter, some small modifications have been introduced. As can be seen in Fig.4.1 the central structure of the mobile electrode is a simple square.
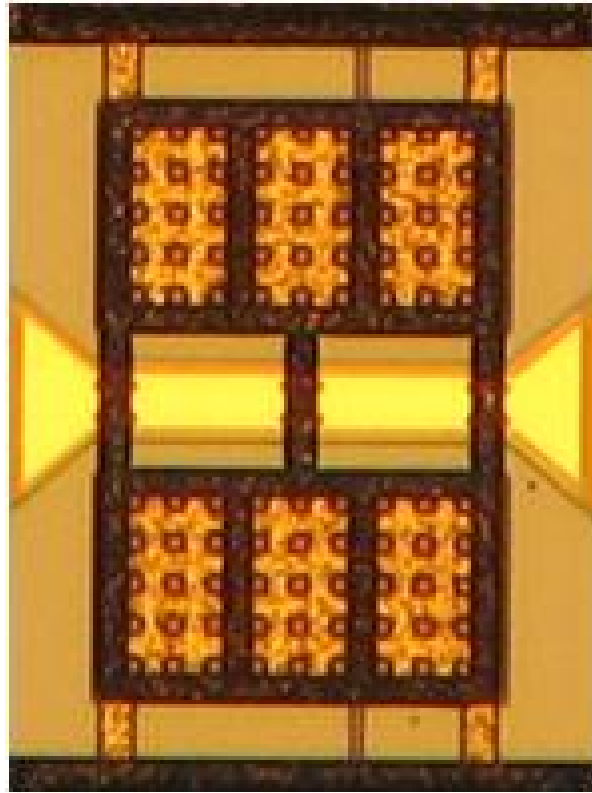
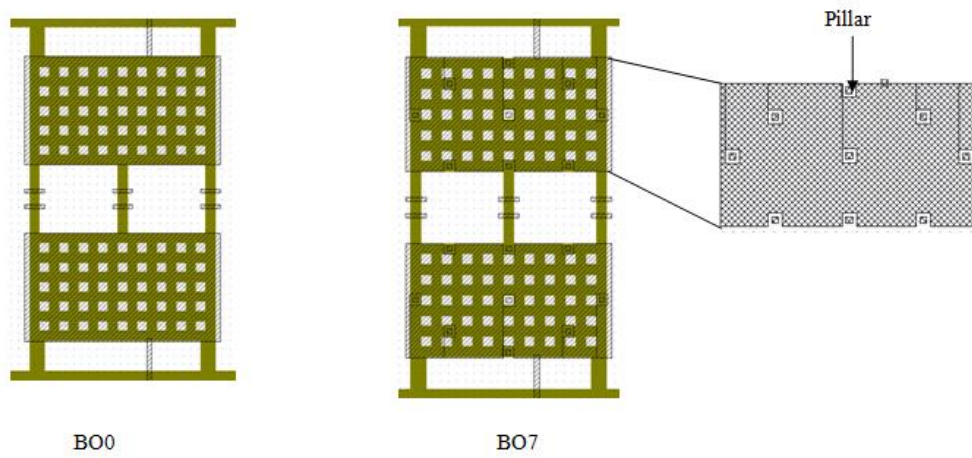Figure 4.22: The Capacitive Shunt switch Bo.0.

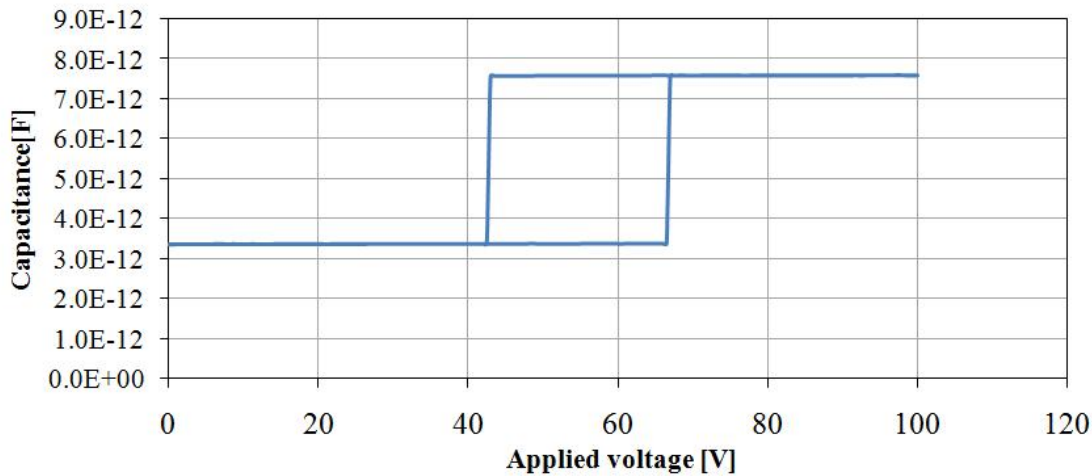Figure 4.23: Layout of the two capacitive shunt switches.

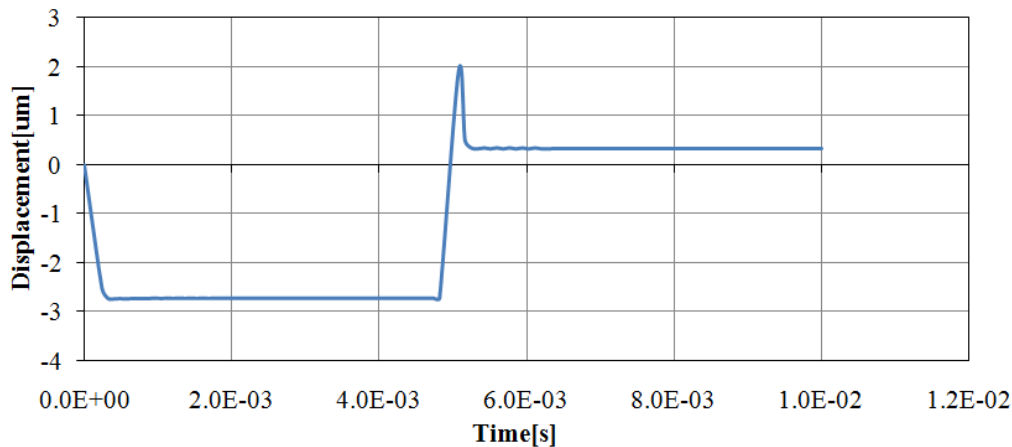Figure 4.24: Simulated CV characteristics for the BO.0 device.

Figure 4.25: Displacement versus time characteristics of the device BO.0 for 70V applied.

Starting from this, two slightly different forms have been created, simply by adding or subtracting half circular areas. For both shapes transient dynamic simulations have been preformed as outlined above. Fig 4.27 shows the shape of the three variants of the layout (including the unchanged sample structure). Fig 4.28 compares the results of the transient simulations of all three shapes. This numerical experiment has provided contradictory
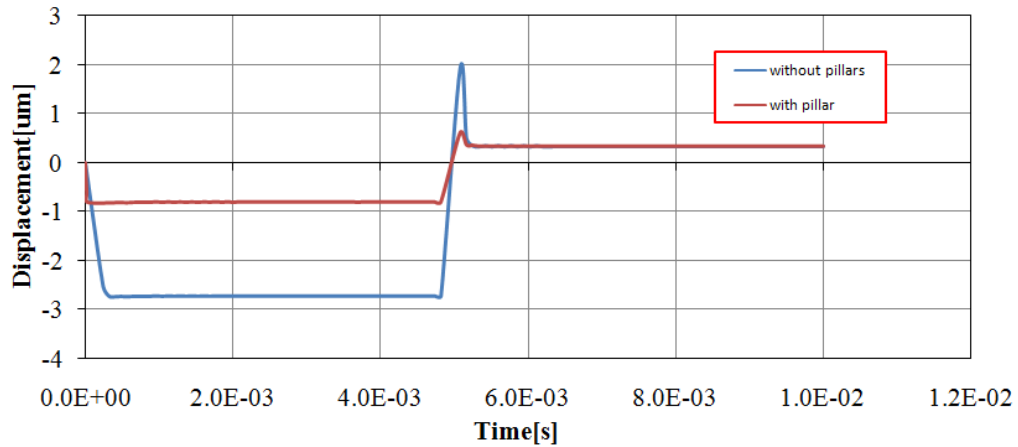
Figure 4.26: Comparison of the two displacement voltage characteristics.

results. On one side the behaviour of both modified geometries differs significantly from the unchanged structure, on the other side they don't differ much from each other. Even if this could be in relation to the complex air dynamics around the structure no definite conclusion can be taken from this preliminary test.

4.4 Discussion

In this chapter different parameter affecting devices made with FBK technology have been studied with the help of numerical modelling. The effects produced by factors like material properties, gap height, different applied voltage and finally the effect produced by stopping pillars are have been discussed. While most of the studied factors can contribute in reducing the switching time, the use of stopping pillars probably produces the most interesting results. Other factors like mass or gap size reduction have either a minor influence on the switching time or require changes in the technology not always easy to implement. Also the use of higher voltages is of limited applicability, as it applies only on the closure cycle of the switch
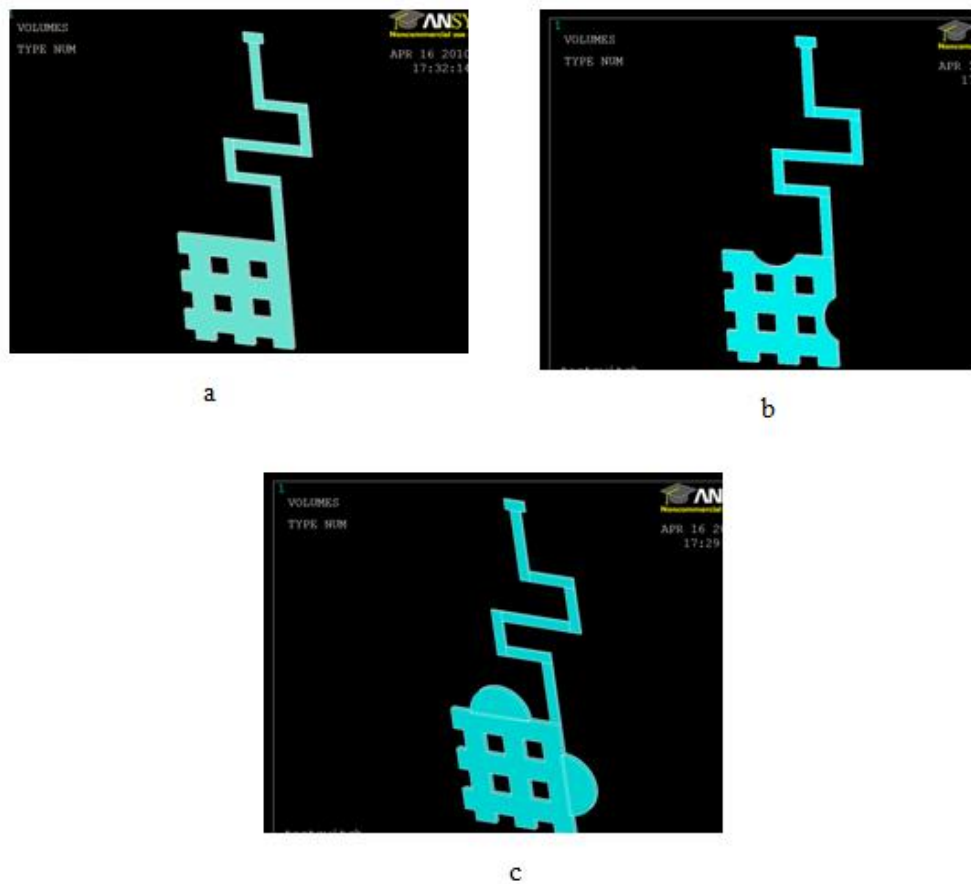
Figure 4.27: Layout variants to evaluate the influence of the shape of the mobile electrode. a) Shape of the unchanged sample structure, b) shape of the structure resulting from the subtraction of small half circle areas and c) shape of the structure resulting from the addition of small half circle areas.

and is in principle limited by the breakdown in air, even if this could be likely pushed beyond the limits encountered in the actual devices with a careful design.

From this semi-quantitative and clearly not exhaustive investigation it seems that the easiest way to reduce the switching times is the use of stopping pillars. The pillars not only guarantee the presence of a minimum gap which always allows the air flow but also shortens the travel
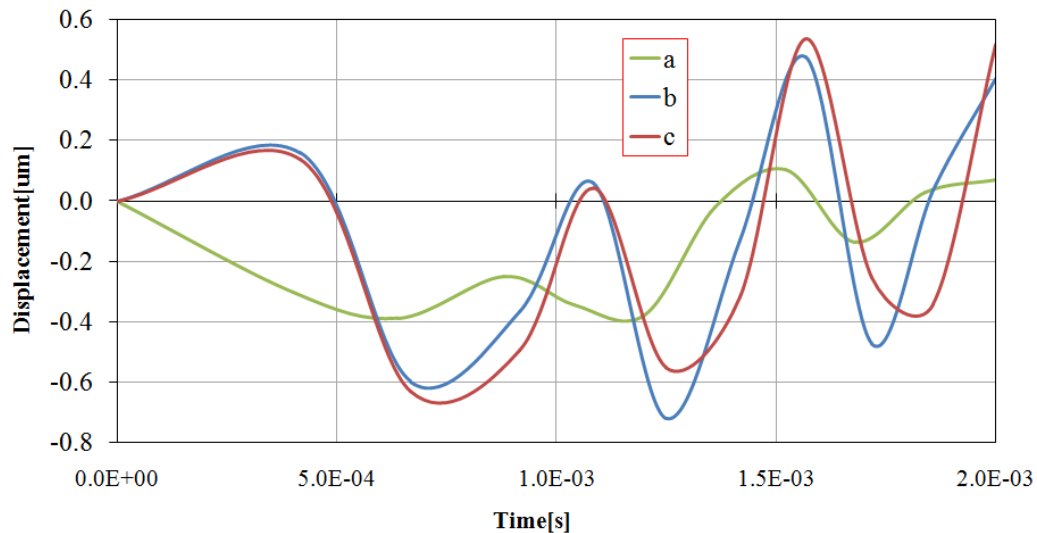
Figure 4.28: Comparison of the displacement vs. time curves of the three design variants. a) Unchanged sample structure, b) structure resulting from the subtraction of small half circle areas and c) structure resulting from the addition of small half circle areas.

range of the mobile structure. Of course dimension and position of the pillars will have to be carefully studied in an optimized switch design. In addition also the overall dimension and shape of the mobile structure very likely influences the switching time, which again could be exploited in an optimized design especially in the case of small devices.

It seems therefore that a not yet fully exploited potential of improvement exists with regard to the switching time of RF MEM switches, as well as for the impact damage and stiction, which can be addressed by the designer. Further improvements can come from changes in the technology itself, but these are much more difficult to implement because even minor changes in the technology have many implications on the rest of the process and on the overall performance of the devices.

Chapter 5

Static and Dynamic Electro-Mechanical Characterization of the RF MEM Switches

5.1 Introduction

In order to verify the results obtained by numerical simulations and determine their accuracy, different series of measurements have been performed on selected device geometries. For this validation process three capacitive shunt switches, devices BO0, BO7a and BO7b , have been selected for their regular and similar design. Three additional device geometries, BATS, BATM and BATL from different fabrication lots ,have been characterized in order to complete the picture. In all cases the characterization proceeded in order of complexity. After device fabrication a first measurement of the device topology with a 3-D profilometer was performed in order to ascertain the structural integrity of the device and the non-idealities eventually affecting the device. Next the primary electro-mechanical parameters were measured with a quasi static CV measurement and finally the transient dynamic properties of the devices were investigated with the aid of an optical profilometer equipped with a laser Doppler vibrometer.

5.2 Device geometries

The three shunt switches, BO0, BO7a and BO7b are characterized by a mobile electrode build out of two rectangular plates linked together with three strong beams. The central electrode is connected at the two anchor posts with two flexible beams at each side. Both switches have a floating electrode, which is contacted by the three beams connecting the two plates through dimples placed on the central line of the signal line once the mobile electrode is pulled down. The two devices differ from each other by the geometry of the actuation electrode: BO0 has a conventional actuation electrode design based on two rectangular polysilicon plates matched in size to the two main rectangular plates forming the mobile electrode, while BO7 has a modified actuation electrode that includes mechanical stoppers or pillars. These pillars are created by stacking small multimetal squares of on top of similar polysilicon shapes. The pillars introduce a step height of 630 nm, which prevents the mobile electrode from touching the actuation electrode. Fig. 5.1 a) shows the general layout and Fig. 5.1 b), c) and d) show the geometry variations of the actuation pad of these devices. The only difference between B07a and BO7b is in the height of the pillar , that in the case of the BO7 b the height of the pillars is higher than BO7a. The area of the pillars reduces the total nominal area of the actuation electrode by about 3,7%. Due to the small size of the pillars ($10x10$ μm^2), comparable in size with the gap height, the effective area reduction of the actuation pad is even more negligible. An oxide layer of 300 nm covers both versions of electrodes. Originally these pillars were intended for the prevention of the charging of the oxide layer covering the actuation electrode. The three devices BAT-S, BAT-M and BAT-L, are series ohmic switches with wing shaped contacting electrodes. The mobile electrode, identical for all three devices, consists in two rectangles connected with a central beam,
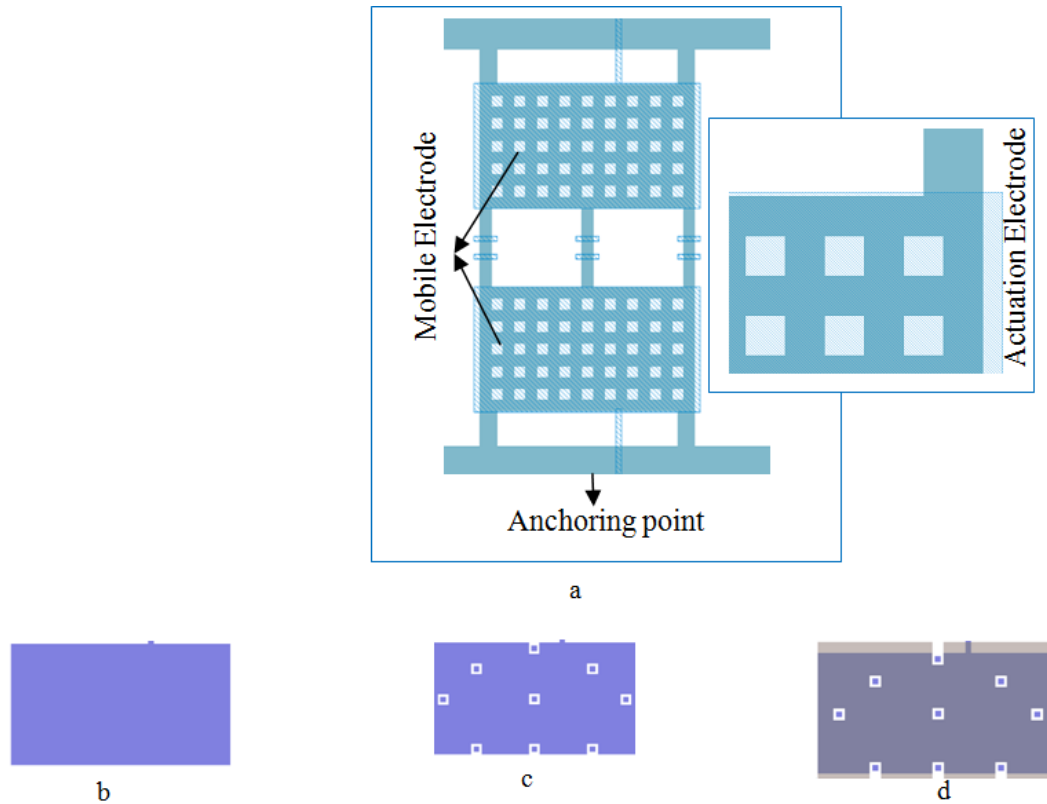
Figure 5.1: a) Layout of devices BO0 , and geometry of the actuation electrodes of b) BO0, c) BO7a and d) BO7b .

all made in 2 μm thick gold. Some parts of these rectangles and the connecting beam are stiffened by a 3.8 μm thick gold. Short but flexible wings are attached at both sides of the central connection beam. In the closed position these two wings realize the DC electric contact to small dimples created in the transmission line. Fig 5.2 shows the general layout of each device with equivalent actuation pad. The three designs differ for the suspension springs and for the shape of the actuation pad. All three devices feature meander type springs in 5.4 μm thick gold. BAT-S has a long meander type spring, while the other two devices feature a meander spring with shorter legs, which makes them much stiffer. The actuation pads are different for all devices. BAT-S has the largest actuation electrode, which

in this case has the same overall dimensions of the mobile electrode. BAT-M has a smaller actuation electrode. In this case the actuation electrode covers only about half of the two rectangles at the extremes of the mobile electrode. BAT-L features the smallest actuation electrode. In this case the area of the actuation electrode covers the connecting beam and part of the two wing elements. All devices have stopping pillars and they are not covered with oxide as these devices are intended to be dielectric free in order to reduce or eliminate the possibility of charging during actuation.
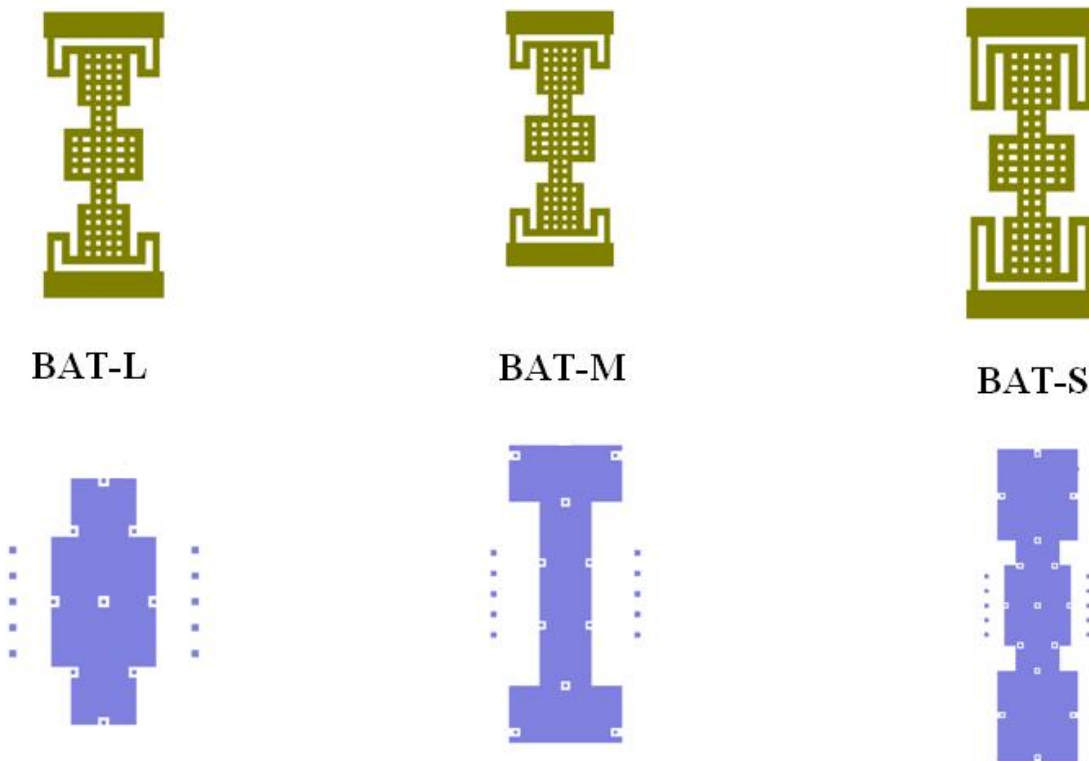

Figure 5.2: General layout of devices BAT-S,BAT-M, BAT-L, associated with the specific geometry of the actuation pad.

5.3 Geometrical Characterization by 3-D Optical Profilometer

A 3-D profilometer uses white light interferometry for characterizing and quantifying surface roughness, step heights, critical dimensions, and other topographical features with excellent precision and accuracy. Optical profilometry is nondestructive, fast and requires no sample preparation. FBK employs a NewView 6300 profilometer from ZYGO, together with the analysis and image processing software MetroPro, which provides extensive 2D and 3D data analysis, visualization and data processing options. In addition to basic features a number of advanced application modules are available to extend the capabilities of the instrument such as dynamic metrology, segmentation analysis, field stitching, and thin film analysis. Fig 5.3 shows the set up for optical 3-D measurements and Fig. 5.4 and Fig. 5.5 show an example map and height profile of a BO0 and BAT-S. The instrument at FBK can be only used for static measurements. In this thesis it has been employed to establish the height map and height profiles of the studied samples. This allowed us to have a qualitative assessment of the devices and to obtain a quantitative measurement of the thickness of the layers. In addition the height maps provide the out-of-plane displacements of the mobile electrodes, which in turn allow the determination of the stress gradient affecting the single device.

5.4 Quasi-Static Capacitance-Voltage Measurements

In order to determine basic electromechanical parameters like actuation voltage, C_{on} and C_{off} capacitances and to ascertain the full mechanical functionality of the devices, capacitance-voltage (CV) measurements have been done on all the samples. The characterization consists in the measure-
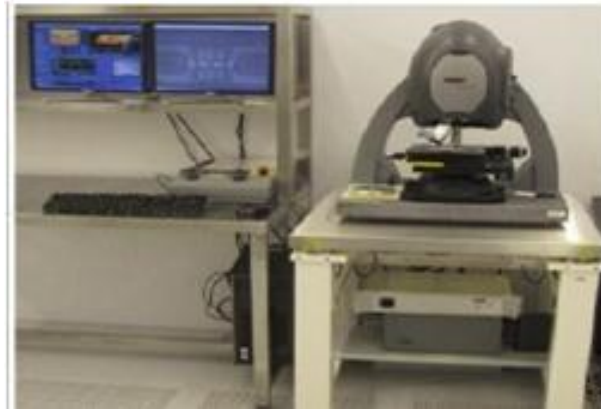
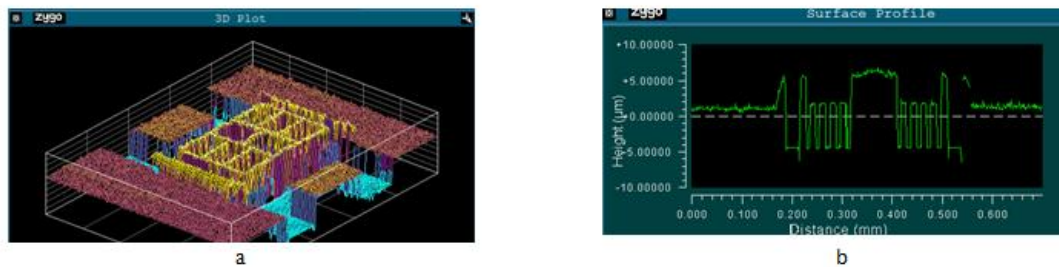Figure 5.3: The optical 3-D profilometer NewView 6300 from ZYGO.

Figure 5.4: Height map of device BO0 obtained by the 3-D optical profilometer together with a height profile of each sample taken along the central axis.

ment of the capacitance of the mobile electrode with respect to the signal line while a slow voltage sweep is applied to the actuation electrodes. The measurement is performed directly at wafer level by contacting the devices with needle probes in a manual probe station. The capacitance is measured with an LC[4285A] meter from HP and the voltage sweep is generated by a HP 4136C multiparameter tester. Fig. 5.6 shows the set up of the static CV measurement. In detail the measurement procedure is as follows: a) first a LABView routine is started on the PC that controls the instruments of the probe station and properly initialized by providing the parameters for the measurement, b) next the LC meter is powered up,
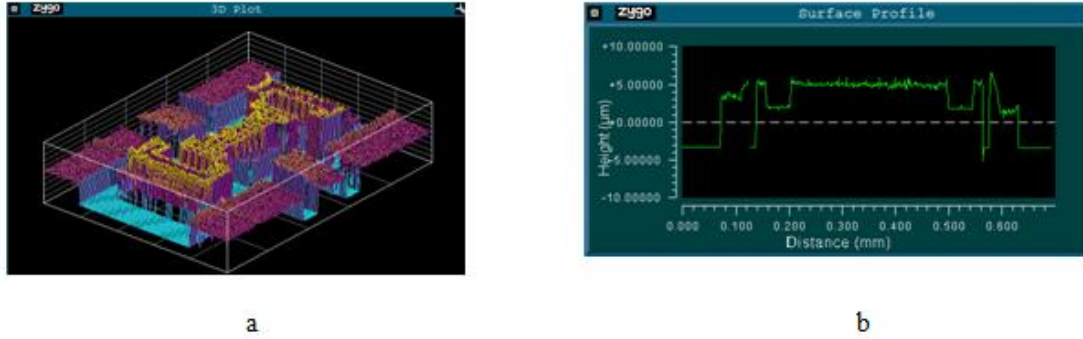
Figure 5.5: Height map of device BAT-S obtained by the 3-D optical profilometer together with a height profile of each sample taken along the central axis.

c) then the wafer is placed on the chuck of the probe station and fixed with the vacuum (d) and the needles are placed in order to contact the actuation pad, the ground and the two branches of the signal line, in case of a series switch, or the signal line in case of a shunt switch (e). At this point the LC meter has to be calibrated in order to correctly detract the impedance of the connecting cables. To this purpose the needles must be first pulled up to create an open circuit situation. Once the calibration is finished the needles are lowered again and the measurement can start. Typically in the first measurement a voltage sweep with a low maximum voltage is performed. In the following sweeps the amplitude of the voltage sweep is then increased. Typically three to five measurements with increasing voltage amplitudes are performed to fully characterize the mechanical behaviour of a switch. Fig 5.7 shows schematically the position of the needles during a CV measurement of a shunt switch and Fig 5.8, 5.9 and 5.10 show respectively the CV curves obtained in case of device BO0, BO7a and BO7b. From the CV curves it is possible to extract the pull-in voltage and the pull-out voltage of the switch as well as the C_{on}

and C_{off} capacitance. A more detailed analysis of the CV curve branch below the pull-in can also provide a measure of the spring constant of the structure. Table 5.1 summarizes pull-in and pull-out voltages, as well as C_{on} and C_{off}. In the case of the series ohmic switches the measurement procedure differs from that of the shunt switches as in this case a current-voltage (IV) curve is measured. Fig. 5.11 shows the position of the needles for this case and Fig. 5.12, Fig.5.13 and Fig.5.14 respectively summarize the IV curves obtained in case of device BAT-S, BAT-M and BAT-L . In this case a small voltage difference is applied to the two signal terminals of the switch and the current flowing through the device is monitored in as a function of the applied voltage. Table 5.2 summarizes the main electrical and electromechanical parameters extracted from the IV curves.
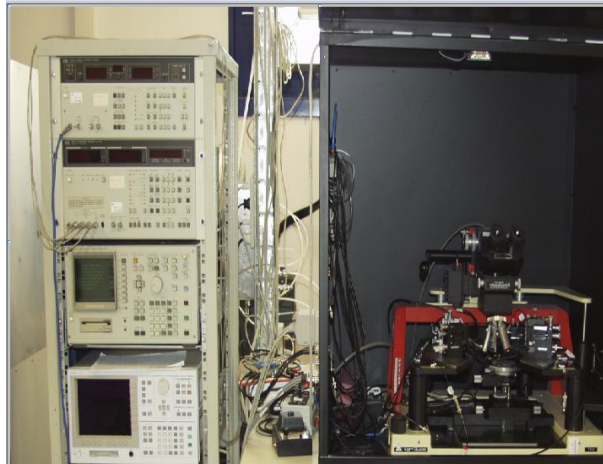

Figure 5.6: Set up for the quasi static CV measurement.

5.5 Transient Dyanmic measurment

Once the previous characterizations showed the functionality of the devices and provided the basic mechanical parameters, the transient dynamic behaviour of the devices was investigated. This investigation has been
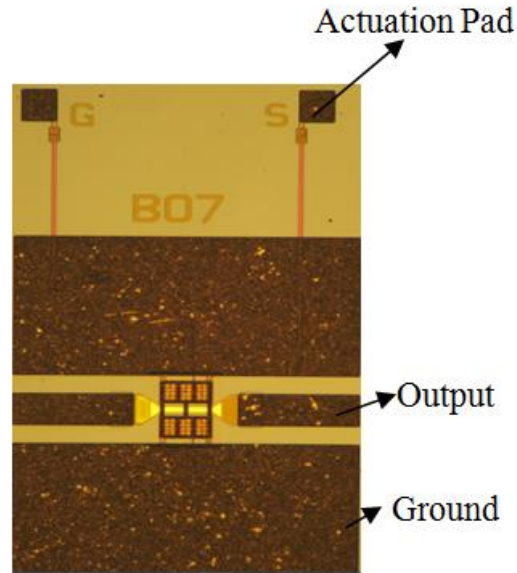
Figure 5.7: Picture of a device under test showing the position of the needles for CV measurement in case of a shunt switch.
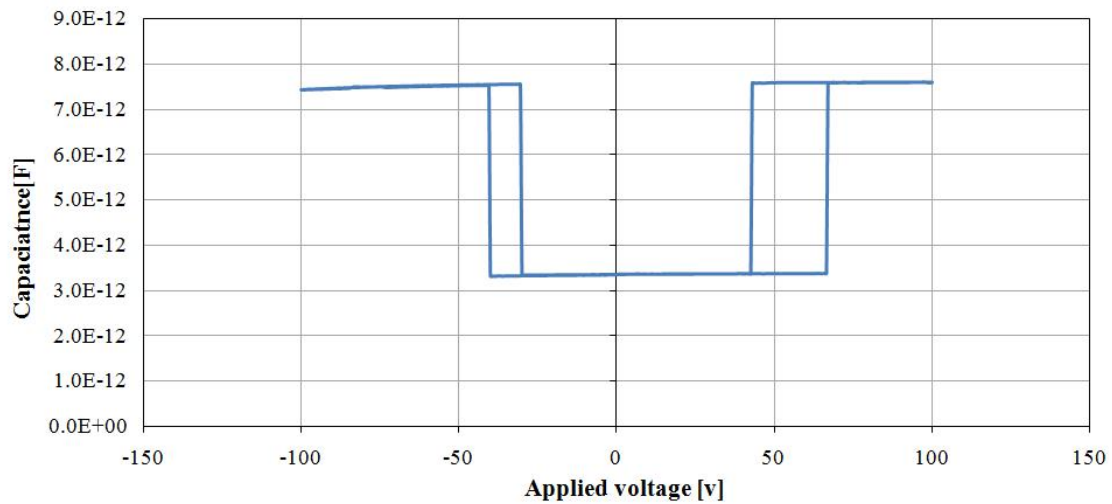

Figure 5.8: Quasi static CV curves of BO0.

performed at the University of Padova with a Polytec MSA-500 optical profilometer equipped for the dynamic characterization of MEMS struc-
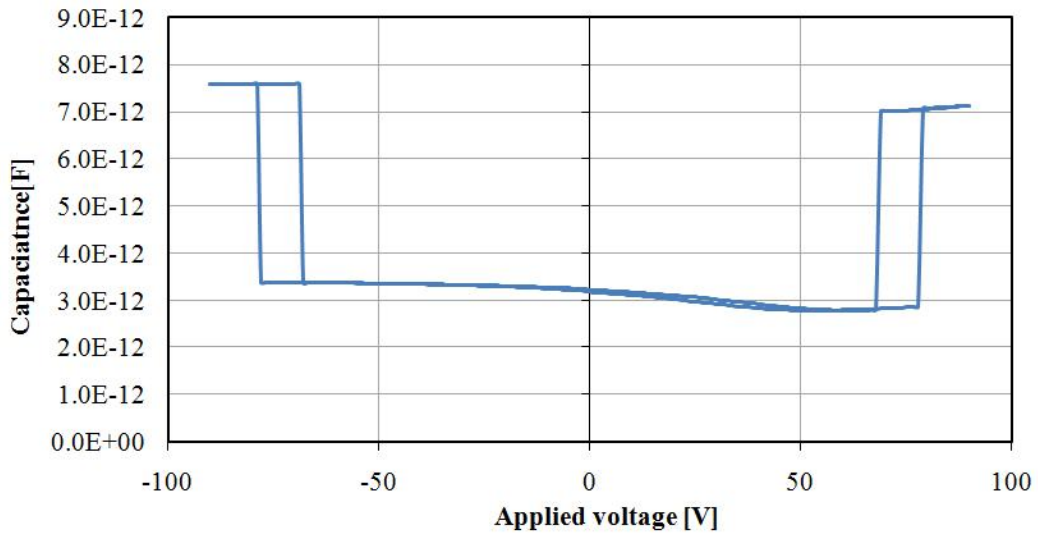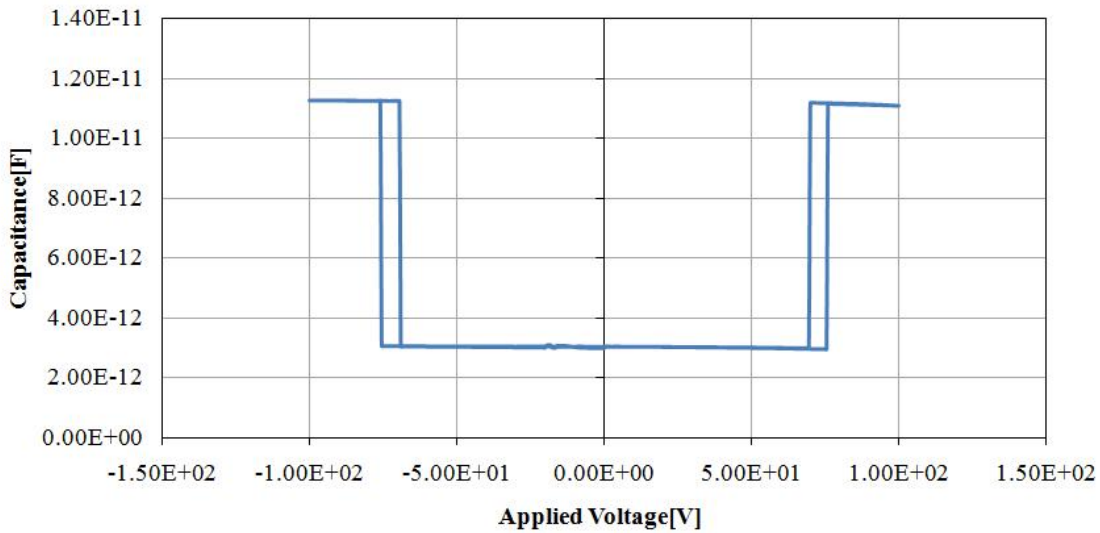
Figure 5.9: Quasi static CV curves of BO7a.

Figure 5.10: Quasi static CV curves of BO7b.

tures. This optical profilometer is mounted on a Cascade R4800 probe-station and isolated from environmental noise by means of a Newport anti-vibrating table. The MSA-500 profilometer integrates a microscope with Scanning Laser-Doppler Vibrometer, Stroboscopic Video Microscopy

	Pull in Voltage [V]	Pull in Voltage [V] [Simulation]	Pull out Voltage [V]	C_{on} [pF]	C_{off} [pF]	Curvature [m]	
BO0	67	66	42.5	7.58	3.36	-3,70	±2,73
BO7a	79	77.5	68	7.06	2.8	-1,45	±0,43
BO7b	76	74.5	69.5	1.12	2.98	-0,61	±0,80

Table 5.1: Summary the pull-in voltage,pull-out volatge,C_{on},C_{off},extracted by CV curve,together with simulated pull-in volatge and estimated radios of curvature of devices BO0,BO7a and BO7b
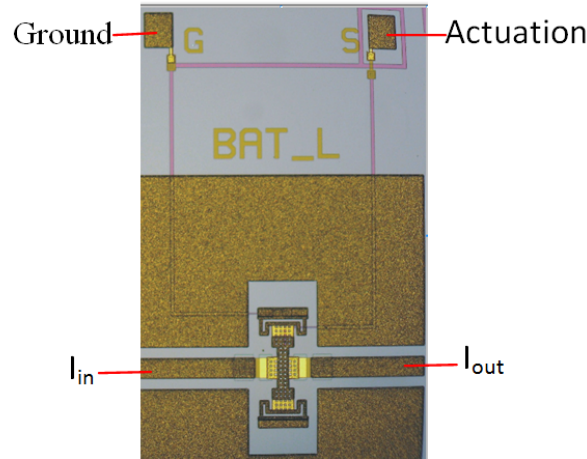

Figure 5.11: Position of the needle probes for the IV characterization of a series ohmic switch.

and White Light Interferometry, making possible topography analysis, as well as out and in-plane vibration analysis both over time, and frequency. A high voltage amplifier was employed to amplify the signal generated by the internal arbitrary waveform generator of MSA-500. A pseudo-random signal was applied to the device under test, measuring the LDV(Laser Doppler Vibrometer) response over frequency, whereas a square pulse signal (f=100Hz, d.c.=50 %) was used to characterize the displacement over time of the movable membrane during the actuation and release transients.
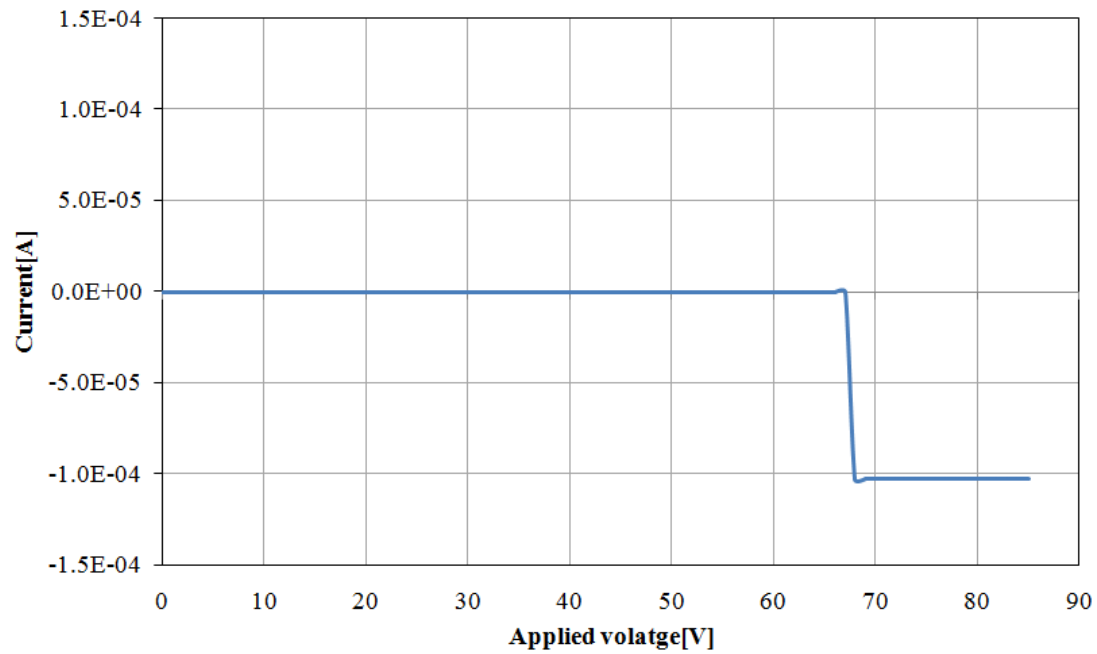
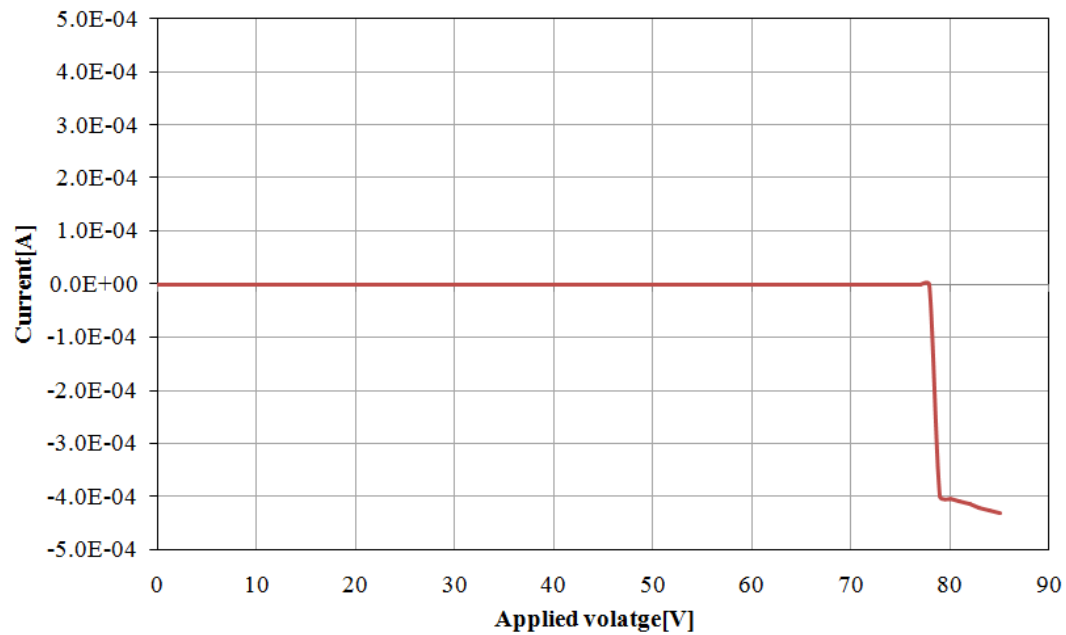Figure 5.12: The quasi static IV curves of BAT-L.

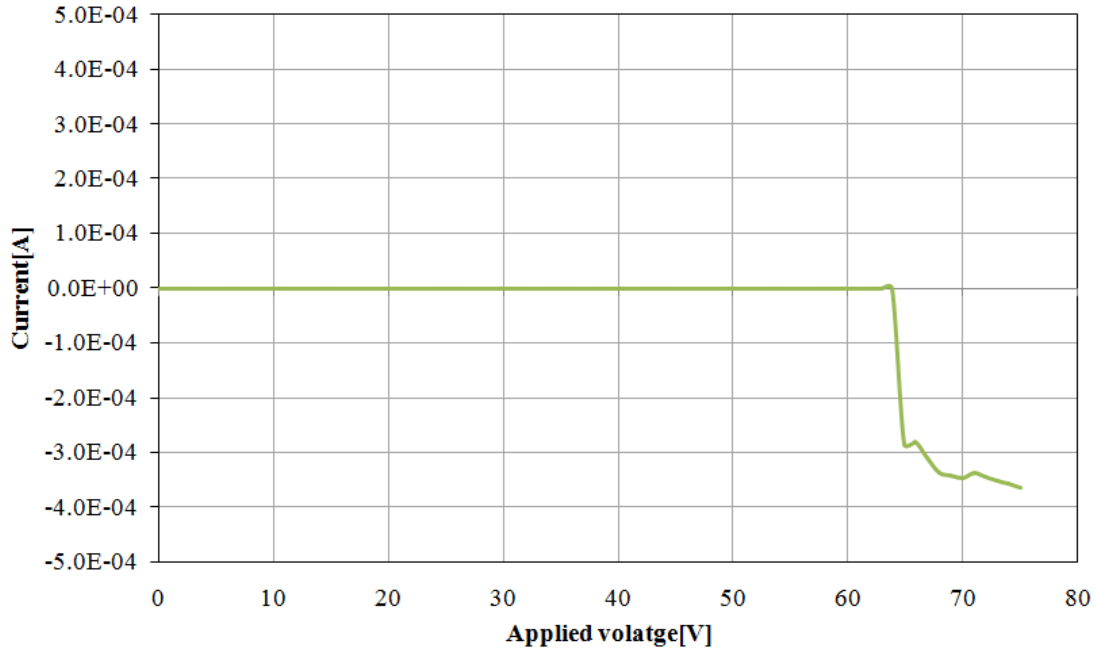Figure 5.13: The quasi static IV curves of BAT-M.

Figure 5.14: The quasi static IV curves of BAT-s.

A Tektronix TDS6804B DSO[Digital Storage Oscilloscope] (8GHz analogue bandwidth) completed the system, in order to monitor applied signals. The same DSO and an Hp 8114A pulse generator were used to characterize the actuation and release transients from the electrical point of view. A 6 GHz RF signal (0dBm, from the internal RF generator of an Hp 8753E Vector Network Analyzer) was applied to the input port of the DUT and the signal at the output port was measured. By comparing the bias signal applied to the actuator with the RF signal at the output port the actuation and release times were extracted. Fig 5.15 shows the set up of the instrument during the dynamic measurement. The dynamic measurement has been done on the central part of the structures. With this instrument an extensive characterization of the devices both in static and dynamic regime has been performed. Here we present a summary of the measurements.

	Pull in Voltage $[V]$	I_{in} $[A]$	Curvature $[m]$	
BAT-L	68	-1.03×10^{-4}	-4,8	$\pm 17,7$
BAT-M	78.9	-3.99×10^{-4}	-7.7	$\pm 7,2$
BAT-S	64.9	-2.58×10^{-4}	-0,5	$\pm 10,4$

Table 5.2: Summary of the main parameters of the IV curves together with the measured curvature of devices BAT-S,BAT-M,BAT-L
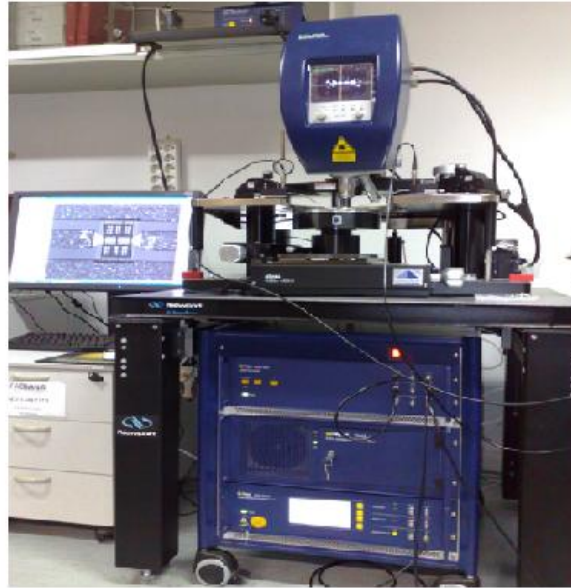

Figure 5.15: Picture of the set up for dynamic measurement.

5.5.1 The shunt switch BO0 (without pillars)

On this device transient dynamic measurements were performed at different applied voltages. Fig. 5.16 shows a micrograph of the device highliting the maesurment point,while Fig. 5.17 shows the resonance peak at a frequency of 40kHz as measured by the vibration test. Fig. 5.18 summarizes the displacement versus time curves at different applied voltages and Fig. 5.19 shows the same curves at the closure and release cycle at a much higher temporal resolution. It has to be noted that the displacement is

a relative measurement. It has been found that only the curves for 70 V and higher showed full pull-in. From the damped oscillations of the displacement versus time curves of the transients it was possible to measure the oscillation frequency for different applied voltages. This value has been compared with the measured resonace frequency of the structure. The results summarized in Table 5.3 show that for low applied voltages, less than the pull-in voltage, the oscillation frequency is in good agreement with the natural frequency of the structure, while at higher applied voltages the oscillation frequency decreases, probably due to the higher damping which reduces the resonant frequency.
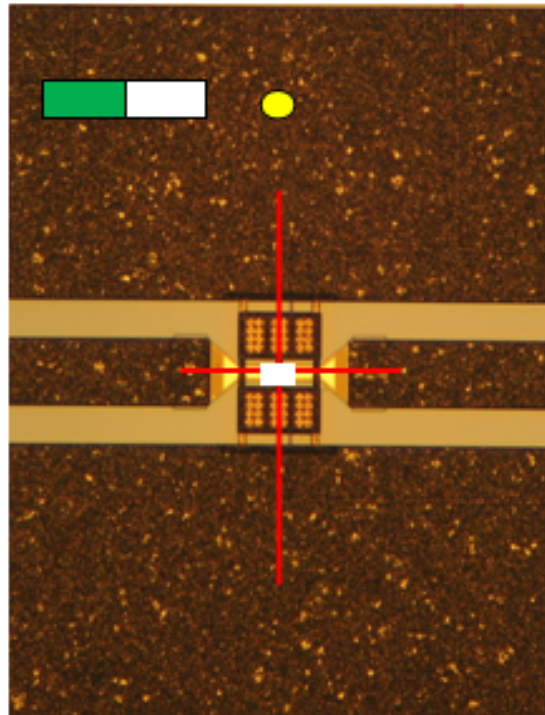

Figure 5.16: Micrograph of the BO0 device with the measurement point,white point (measurment point),the red cross indicate only the center of the screen,the green bar on the top left corner is the strength of the received signal,the yellow dot shows that the laser is switch on.
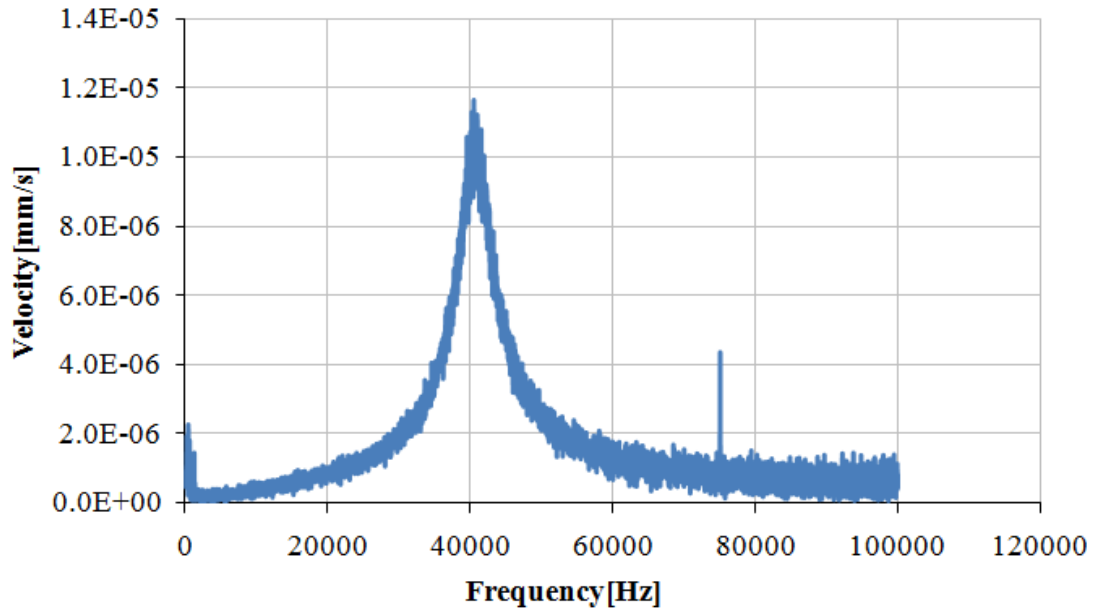
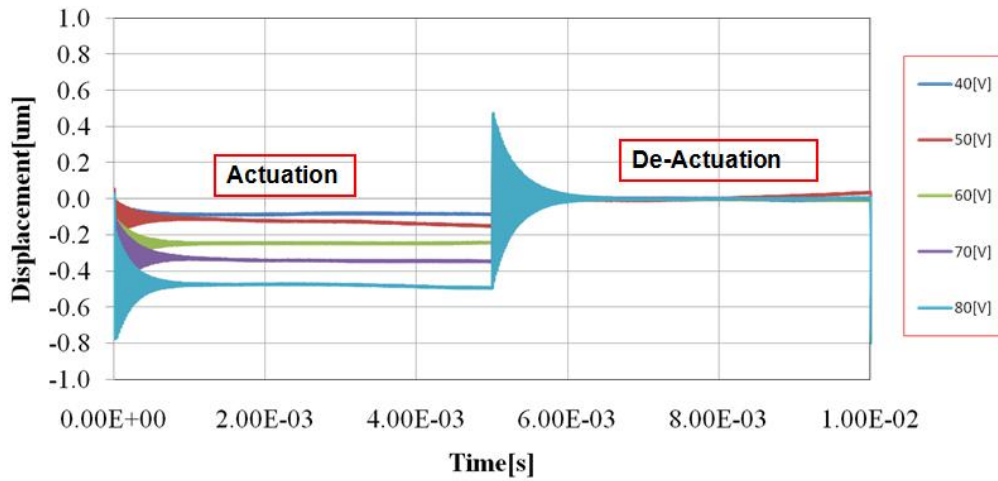Figure 5.17: Resonance peak measured on the device BO0.

Figure 5.18: Transient dynamic behavior of BO0 for different applied voltages.

5.5.2   The shunt switch BO7 (with pillars)

The same measurement has been performed on device BO7a and BO7b. In case of device BO7a , Fig. 5.20 shows the resonant frequency peak as
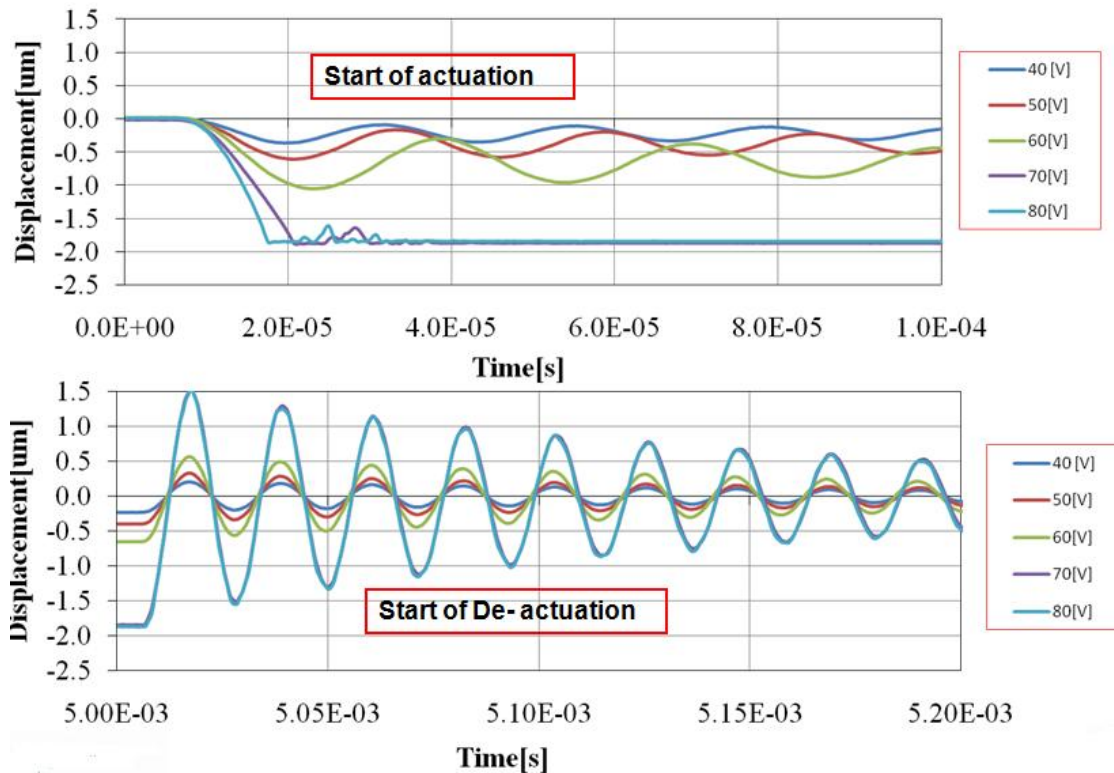
Figure 5.19: Close up of the transient dynamic behaviour of BO0 in the closure and release cycle. The displacement is a relative measurement. Only above 60 V the switch goes in pull-in. the ringing observed at higher voltages indicates that the device resting on the stopping pillars has residual vibrations even after pull-in.

measured by the vibration test, while Fig. 5.21 shows the results of the transient dynamic measurements for different applied voltages and Fig. 5.22 shows the results for short time scale. In this case we observe a resonant frequency peak about 10 kHz higher than in the former case even if the devices have the same mechanic structure. This is also reflected in the frequency of oscillation of the structure. According to the simulations shown in the previous chapter this is very likely due to a reduction of the damping operated by the pillars since they limit the squeeze film effect. Table 5.4 summarizes the the resonant frequencies of the structure extracted from the displacement vs time curves with different applied voltage.   In

Applied voltage [V]	Frequency [kHz]
40	41
50	39.38
60	33.68

Table 5.3: Oscillation frequencies of device BO0 for different applied voltages.
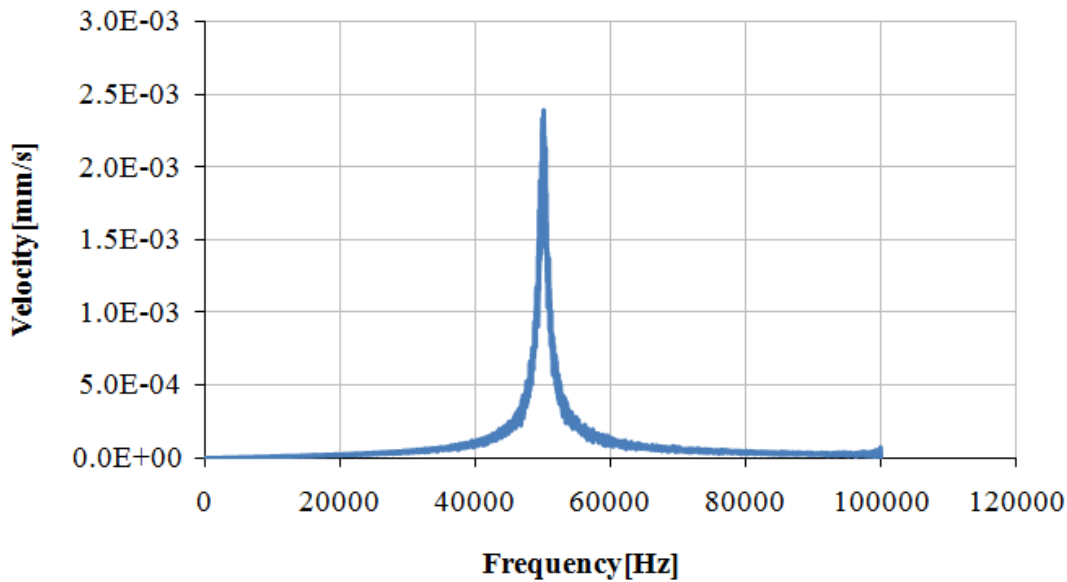

Figure 5.20: Resonance peak measured on device BO7a.

addition a BO7b device has been characterized in the same way as above. In this case the difference between the two devices is in the effective pillar height. As already mentioned, in case of device BO7b the pillar height with respect to the actuation electrode has been increased by removing the oxide layer on top of the actuation electrode .Therefore at pull-in the residual gap between the two electrodes is increased, which in turn reduces the squeeze film effect and the consequently the damping. Fig. 5.23 and Fig. 5.24 respectively show the displacement versus time curves for both devices with an applied voltage of 60 V and the same curves at the closure and release cycle with a shorter time scale. As already mentioned at the
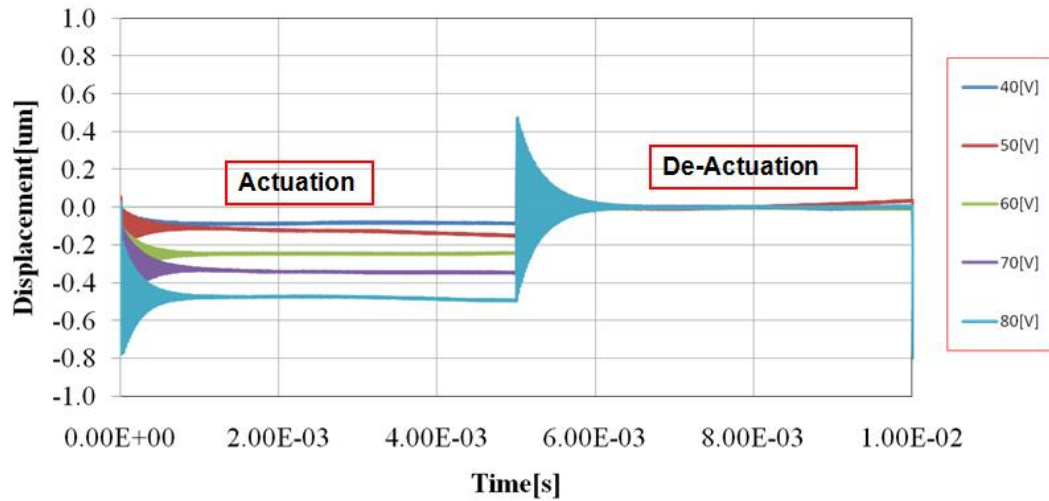
Figure 5.21: Transient dynamic behavior of BO7a for different applied voltages.
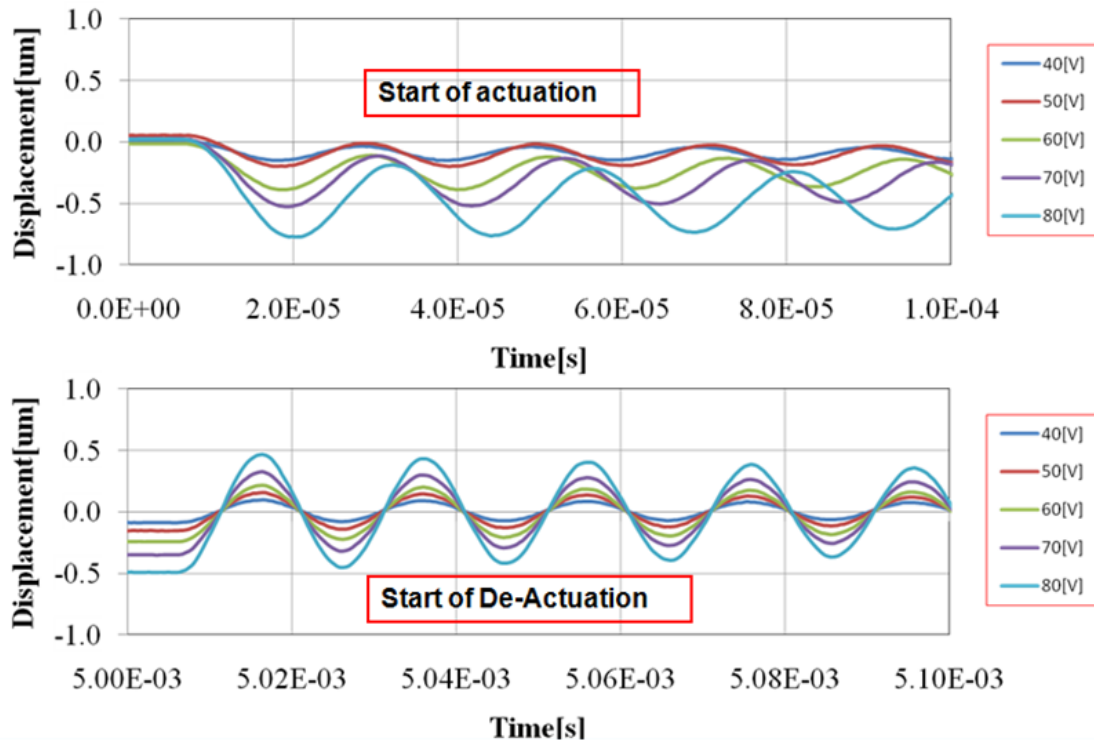

Figure 5.22: Close up of the transient in the closure and release cycle. The displacement is a relative measurement.

Applied voltage $[V]$	Frequency $[kHz]$
40	48.30
50	47.41
60	48.30
40	45.71
70	44.92
80	40

Table 5.4: Oscillation frequencies of device BO7a for different applied voltages.

beginning of this section, actuation and release transients were also characterized from the electrical point of view. Fig5.25 compares the actuation time of the three BAT-x devices. The result shows that the BAT-S can be faster than the BAT-L and BAT-M devices, and changing the meander part of the structure can be effective on the dynamic behavior of the device.
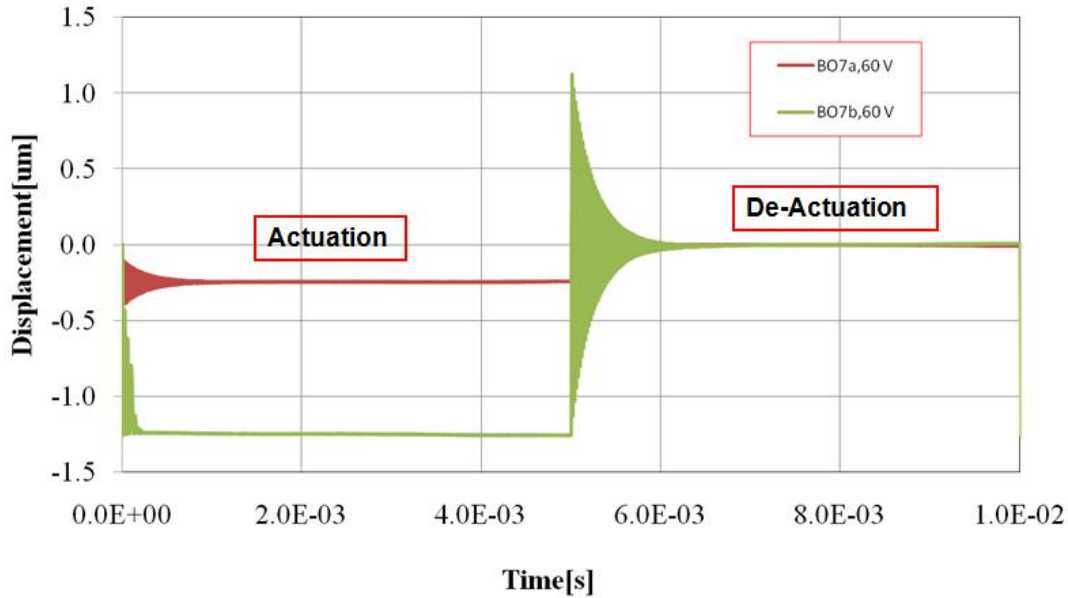
Figure 5.23: Transient dynamic behavior of BO7a and BO7b devices with an applied voltage of 60 V.
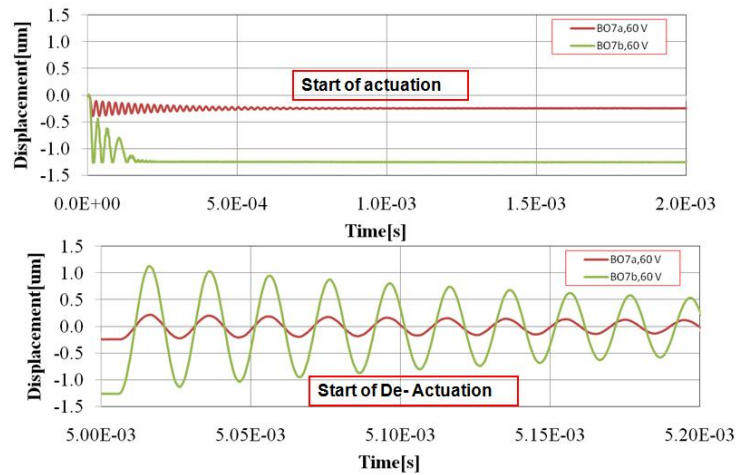
Figure 5.24: Close up of the transient in the closure and release cycle. The displacement is a relative measurement.

Figure 5.25: Actuation times versus applied voltage measured for the three BAT devices

5.6   Discussion

The survey with the static optical profilometer has shown that all devices substantially respect the geometrical specifications of the design. In particular the measured out-of-plane displacements are small and do not impair

Figure 5.26: Compare the result of the simulation with measurment.
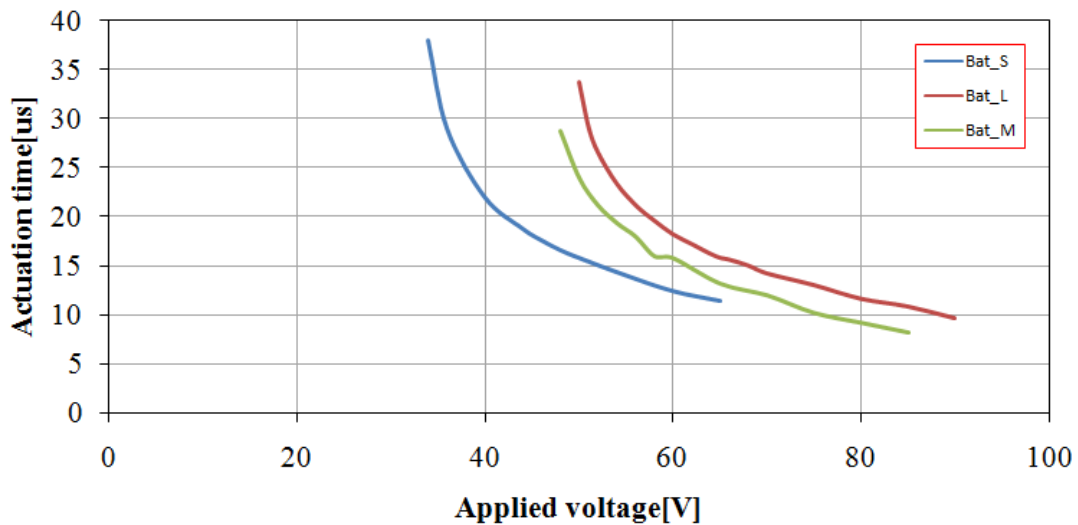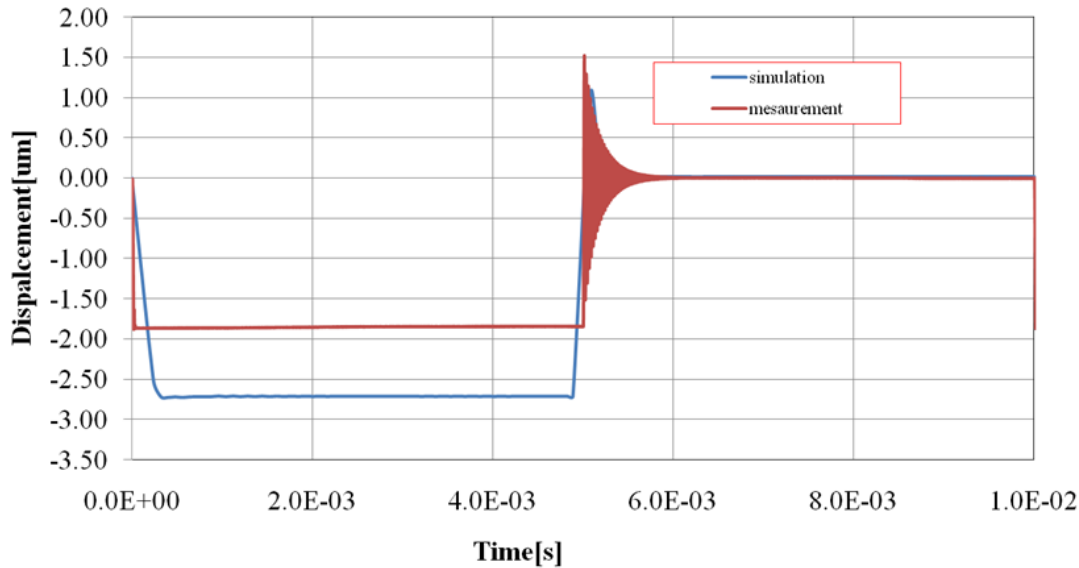
the functionality of the devices. This has been confirmed with the quasi static CV and IV measurements, which showed that all devices are functional. The electrical and electromechanical parameters extracted from the curves are compared in Table 5.1. The comparison between the measured and simulated actuation voltages is good . The differences are very likely due to difference between the nominal and effective layer thickness of the thin gold layer (BRIDGE layer) and the gap height. The first thickness is one of the less controlled parameters in the process and has a significant variation from the centre to the border of the wafer. This is also reflected in the behaviour of the these test devices, since they were included in different regions of the wafer layout. The gap height of the structure also exhibits non uniformities due to the processing, even if these are less evident than those due to the gold deposition. Nonetheless the comparison between calculated and measured values is good and no tentative to reduce the discrepancy was found necessary.The transient dynamic measurements showed that the devices qualitatively behave as expected from the simula-

tions. The comparison of the simulated and measured resonant frequencies is again in good general agreement, see Table 5.3. Again no tentative to achieve a perfect match between theory and experiment has been made. The reason for this was similar as in the case of the static parameters, i.e. the fact that the data are affected by some uncertainties due to the process parameters, which makes it not possible to calibrate the simulation of all devices with a single set of process data. Still these results show that there is enough agreement between experimental and simulated data, thus allowing the simulations to be used for future work on the optimization of the electromechanical aspects of the devices.Fig 5.26 compare the result of the measurment with simulation. The dynamic measurements also showed that a small change in the design of the actuation pad has an impact on the transient dynamic behaviour of the device. The addition of small pillars to the actuation pad increased the resonant frequency of the devices by 25%.Very likely the pillars modify the air flow in the gap and influence in this way the upcoming of the squeeze film. This is also evident from the comparison of the BO7a and BO7b with different pillar height, even if in this case a counter intuitive result has been found, i.e. the switching time decreased with increasing pillar. Due to lack of time it was not possible to investigate in more detail the dependence of the mechanical resonant frequency on the pillar height and which role is played by the distribution of the pillars. Anyway the dynamic measurements and the simulations show that there exists space for improving the mechanical properties of the switches and in particular for reducing the switching times, and the most effective way to do this is to optimize the air flow in the device and therefore the damping characteristics.

Chapter 6

Electromechanical Aspects of Tuneable Capacitors with In-plane Movement

6.1 Introduction

In this chapter we extend our investigation of the electromechanic aspects of RF MEMS devices build with the RF MEM switch technology to the design of tunable capacitors based on a specific shape that allows to exploit the in plane forces that develops in a parallel plate capacitor with partially overlapping electrodes to produce a rotation of the two electrodes against each other. In the recent past some limited research has been already performed on switches with lateral movement [39]. The devices discussed here are based partly on similar principles, but the design has been adapted to the specific technology concept of FBK. Actually such components are the basic ones that will be exploited, within the same technology platform, to develop complex networks. Eight design variants have been developed and realized. All designs show the general behavior of MEMS switches, while four designs show in addition also a behavior that is compatible with a rotation after the pull-down has been reached.

6.2   Concept and Design Description

In case of a parallel plate capacitor with partially overlapped electrodes, where the mobile electrode is allowed to move horizontally with respect to the fixed electrode, an in plane force develops once polarized due to the tendency of the system to minimize the energy stored in the electrical field [38]. In order to exploit this force to generate a rotation of the mobile electrode in a physical device and especially in a varactor, a butterfly shape obtained from two segments of a circle joined in the centre and suspended with a very flexible spring has been adopted. The fixed electrodes are placed in such a way that the developed in-plane forces are tangential and should induce a rotation of the overall butterfly structure. The device has two fixed electrodes; one is intended for "actuation", i.e. for rotating slightly the structure under polarization, while the second one is the fixed electrode of the variable capacitance. These two electrodes are also partially interdigitated in order to separate electrically the actuation circuit from the variable capacitor while still allowing to apply the voltage during the rotation of the structure and maximing the capacitive sensing. A second reason for the interdigitated design was that, in case the supporting spring should be too weak and the structures would collapse before rotating (i.e. vertical movement), the friction force should be lowered and the fingers of the electrodes could act as "rails" which still allow rotation after the collapse of the mobile electrode. The design of the device has been based on the FBK technology. The mobile electrode is in gold, suspended above the two fixed electrodes respectively in poly-silicon and metal. The latter ones have a reciprocal comb structure. In order to stiffen the mobile electrode a frame was added in thicker gold. The whole gold electrode is suspended with springs either straight or meander type. Fig 6.1 shows the cross section of the general design . Fig.6.2 shows one of the layouts as

designed in Tanner EDA L-Edit. Fig. 6.3 and Fig. 6.4 show respectively the gold layer with the reinforcement frame in thick gold and the two fixed electrodes in poly and metal. The pictures were taken from the GDS file of the final wafer layout for the fabrication. The other variants of this basic design concept have been developed by changing the spring design and will be described in the next sections. In order to test other ideas about this concept, two modified designs have been also prepared and added to a subsequent fabrication run.

Figure 6.1: shows the cross section of the general design.

6.3   3-D Optical Profilometer Characterization

After device fabrication all 6 designs have been inspected with the optical 3-D Profilometer. In Fig. 6.5 the height map of a device with meander type suspension spring is shown and in Fig.6.6 the height map of a device with stiff suspension springs. These profiles revealed a slight out-of-plane deformation of the mobile electrode of about 3 μm between the outer rim
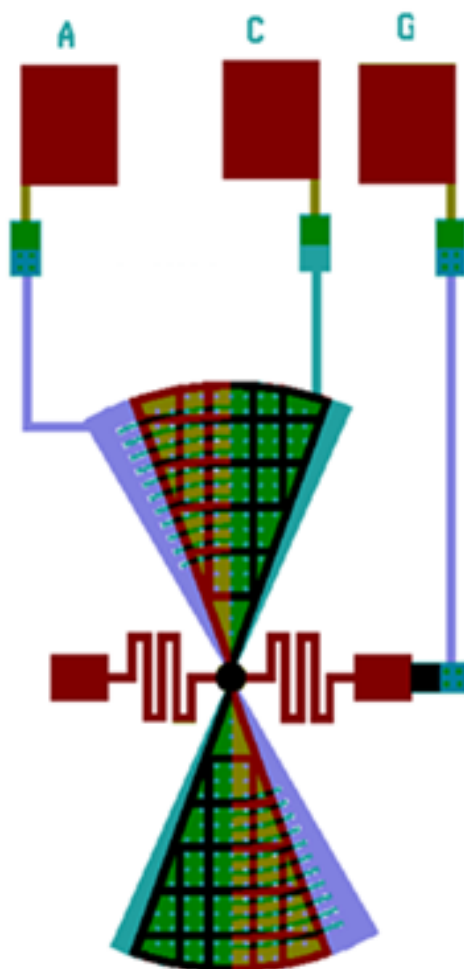
Figure 6.2: The layout as designed in L-EDT A: Actuation pad G: Ground C:capacitance.

and the centre point of the suspended membrane, as it can be seen in Fig 6.5 and also in Fig. 6.6. This deformation is caused by the built-in stress gradient within the gold layer. From the out of plane deformation a mean residual stress gradient of $\sim 2MPa/\mu m$ can be estimated from the curvature of the structure that extracted from the 3-D profilometer measurment. All in all these surveys on the devices showed that the realized devices are sufficiently close to ideally flat structures to be submitted to the electromechanic tests.
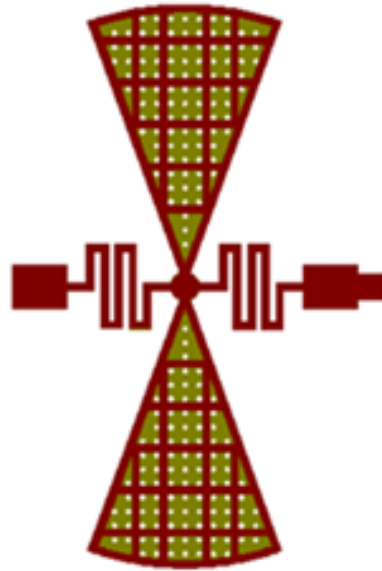
Figure 6.3: The gold layer and the reinforcement layer in thick gold .

6.4   Quasi-Static Capacitance-Voltage Characterization

As in the case of the RF MEMS switches the method of the quasi-static CV (Capacitance vs. Voltage) measurement has been employed in order to establish the basic electromechanic properties of these devices. The measurement procedure is identical to the one presented in chapter 5 with the only minor difference that in this case the capacitance has been measured between the mobile electrode and the fixed metal electrode, while the voltage has been applied to the fixed polysilicon electrode. All 6 designs are based on the general design introduced and will be referred to as Varactor 1 to 6 .The only significant differences between designs regard the shape
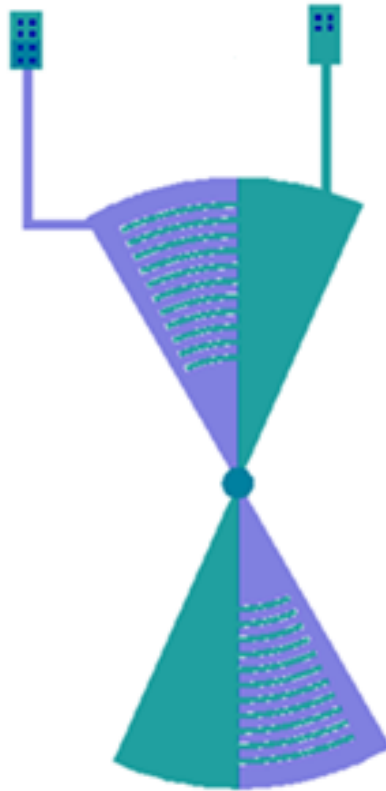
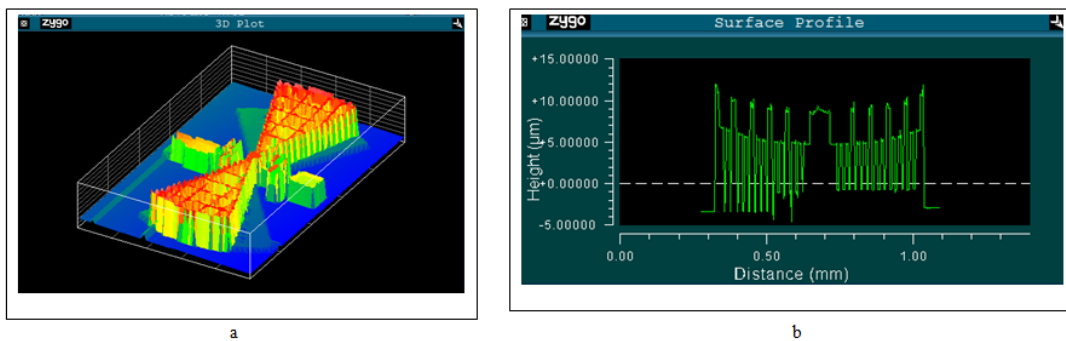Figure 6.4: The two electrodes in poly and metal.

Figure 6.5: 3-D view of the varactor obtained by means of 3D profilometer measure b) Height profile across the central axis of the mobile electrode.
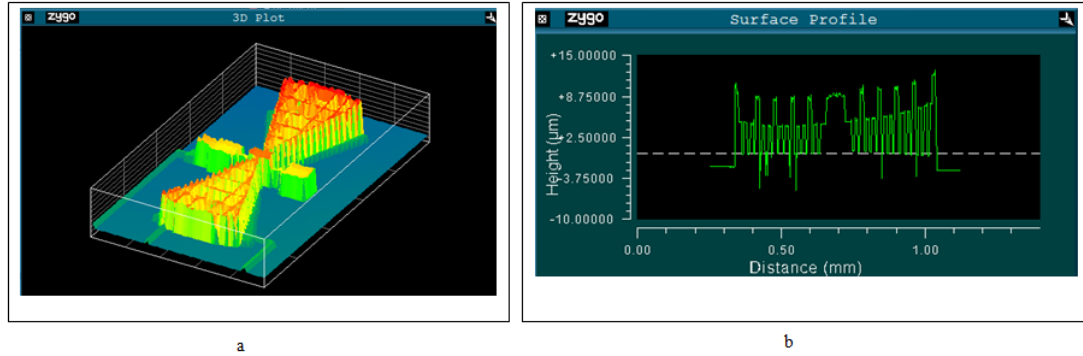
Figure 6.6: 3-D view of the varactor obtained by means of 3D profilometer measure b) Height profile across the central axis of the mobile electrode.

and dimension of the suspension springs and the radius of the arch. The two modified geometries fabricated by a subsequent run will be referred to as Varactor 7 and Varctor 8.

6.4.1   Varactor1

In this case the outer radius of the butterfly structure is 370 μm. Fig. 6.7 a,b) show the layout of the varactor together with the suspension spring and the actuation pad and Fig.6.8 shows the result of the CV measurement. As the in plane force developed by the parallel plate capacitor is likely very small the force exerted by the suspension springs must be very weak. Therefore this design features a meander type suspension spring with two meanders each in order to minimize the opposing torque exerted by the spring. As in the case of the switches the CV curve shows pull-in and pull-out of the structure. Due to the weakness of the spring the device reaches pull-in at relatively low voltages. Unlike the switches, once pull-in occurs the device continues to change in capacitance till finally the capacitance reaches a plateau. On the return sweep the capacitance follows initially the same curve till to a point were suddenly the capacitance raises at a

higher, nearly constant, value till reaching pull-out. The negative sweep of the curve is essentially symmetrical to the positive one.
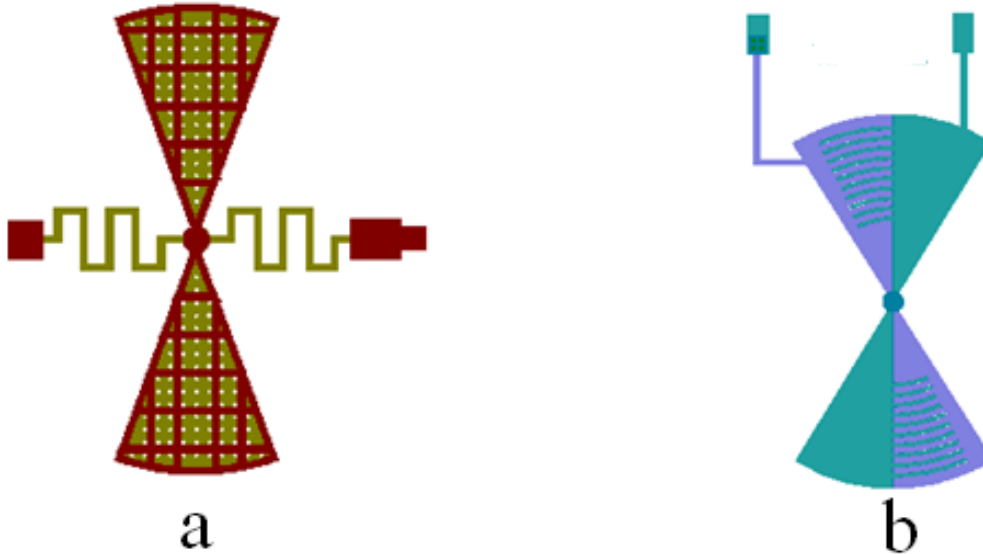

Figure 6.7: a) The layout and b) the actuation pad of varactor 1.

6.4.2   Varactor2

This design has again an outer radius of the butterfly structure of 370 μm. In this case the suspension spring is a much stiffer rectangular shaped spring with a conical width reduction at the joint in the centre in order to reduce the torque resistance of the joint.The layout of varactor 2 and the actuation pad are shown in Fig 6.9 a, b)respectively and Fig. 6.10 reports a typical CV curve of this structure. Also in this CV curve we observe the switch-like behaviour characterized by pull-in and pull-out. Evidently the much stiffer spring structure is not stiff enough to prevent the structure from collapsing at higher voltages. Again after pull-in and before pull-out the capacitance curve departs from the ideal switch like behaviour, i.e.
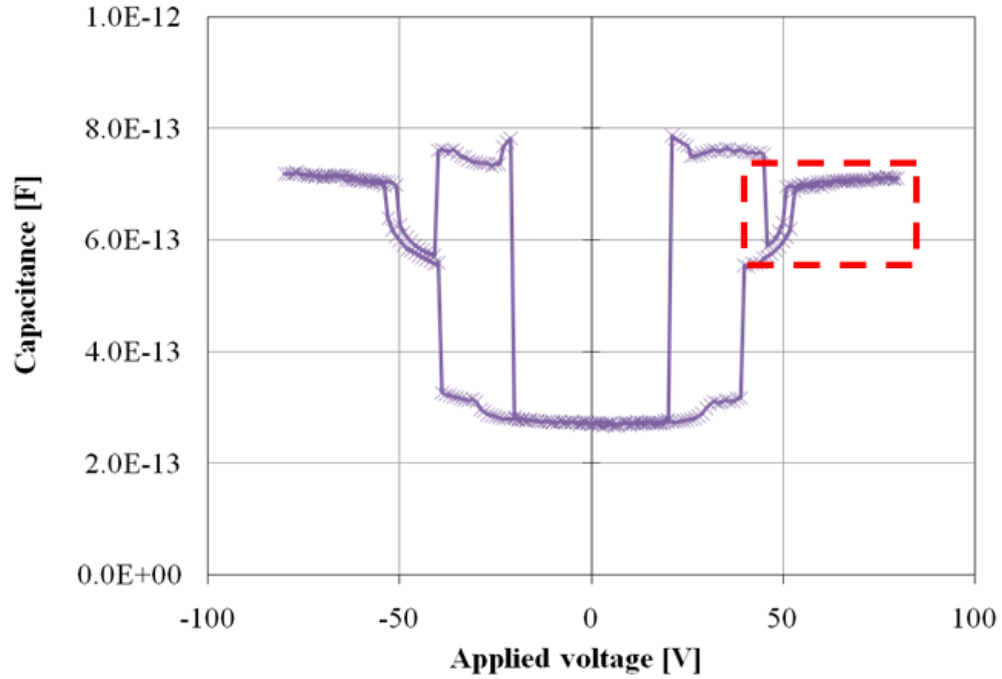
Figure 6.8: The Experimental CV Curve of varactor1.

instead of remaining constant the capacitance voltage curve has a distinct parabolic slope that is maintained in the return sweep until pull-out is reached. Also in this case the CV characteristics is reasonably symmetric.

6.4.3 Varactor3

In this design variant the outer radius of the butterfly shape is reduced to 345 μm. For the rest the geometry of the device is the same as those of the previous ones except for the suspension spring and the actuation pad that replace with the simple actuation pad . The latter one is again of the leaf type, again reduced in width near the centre joint in order to reduce the torsion force necessary for rotation and, in addition, with spring centre axes offset in order to favour the rotational movement.The layout of the
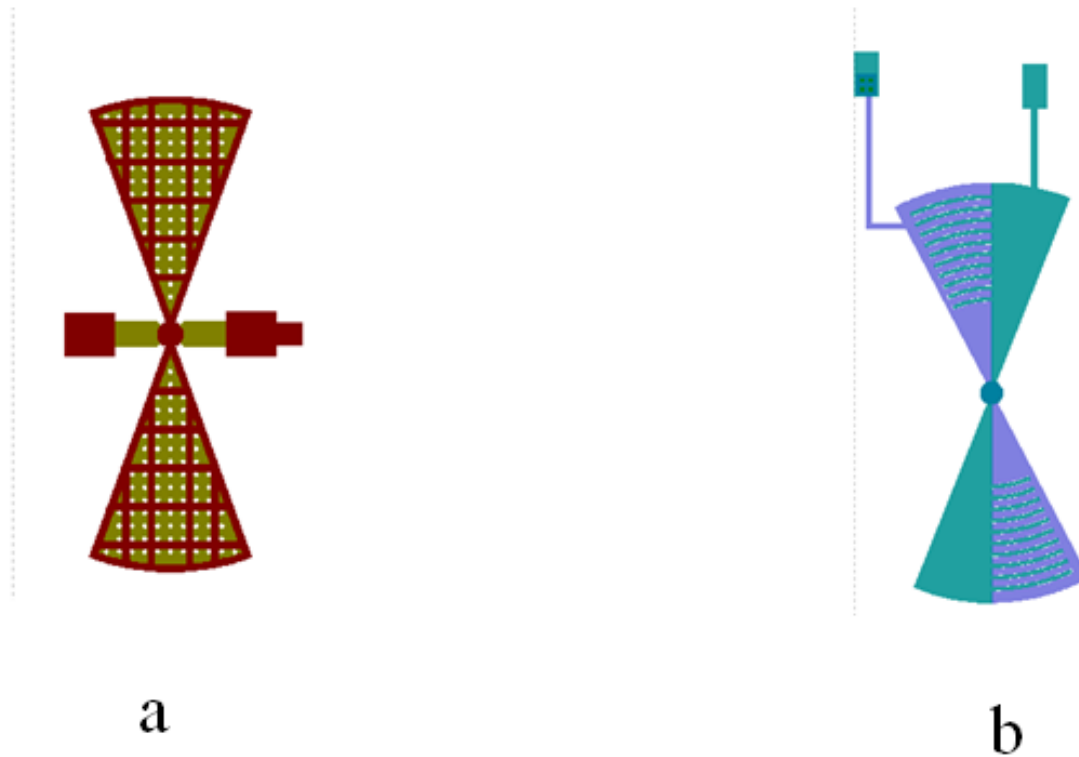
Figure 6.9: a)The layout and b) the actuation pad of varactor 2.

structure , the actuation pad are shown in Fig 6.11 a) and b) respectively and Fig. 6.12 shows the obtained result of the CV curve. The CV curve of this device shows a switch-like behaviour. Also in this case the vertical stiffness of the suspension springs is not enough to prevent the structure from collapse. After pull-in the capacitance reaches a fairly constant value. The slight increase of the capacitance can be due to an increased flattening of the structure, which initially has a positive curvature, operated by the increasing electric field. In the release branch of the voltage sweep the CV curve shows an unusual parabolic change prior final pull-out, similar in shape as the CV curve of varactor 1. The CV curve is symmetrical.
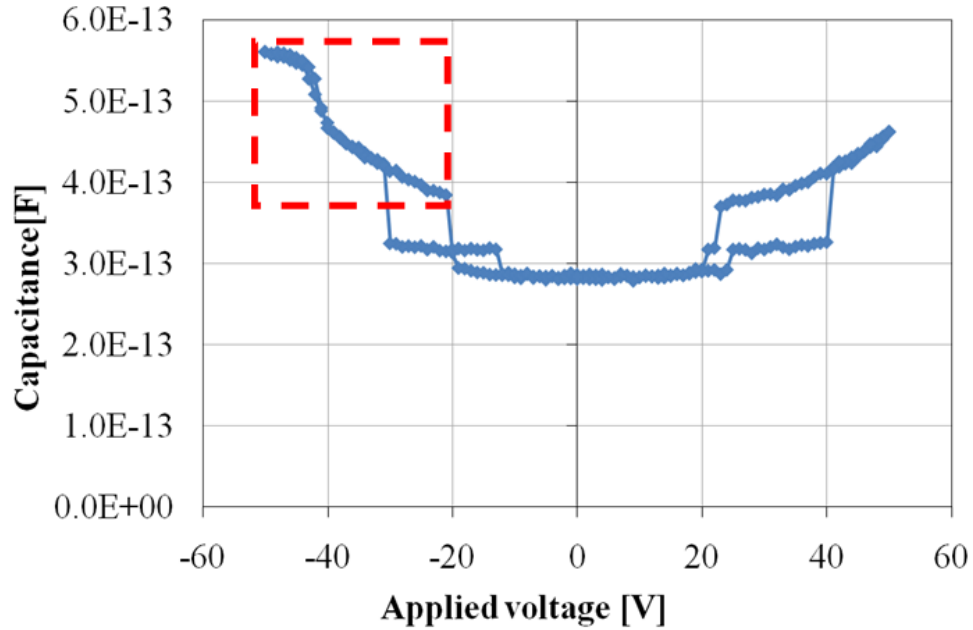
Figure 6.10: The CV Experimental data of varactor 2 .

6.4.4   Varactor4

The outer radius of the butterfly shape of this design variant is 345 μm. Again the structure differs for the suspension spring. In this case a very long and slender meander type spring has been realized in thin gold shown in Fig. 6.13 a) in order to provide an anchoring of the butterfly structure which applies a minimal torsion force on the mobile butterfly structure. Also in this case it is expected that the structure will collapse before rotating. In fig 6.13 b) the actuation pad of the structure is shown. A typical CV curve obtained on this structure is shown in Fig 6.14). Also for this device we observe next to the usual switch-like behaviour a capacitance change after pull-in and before pull-out. After pull-in the curve shows a very steep parabolic change that reaches a fairly constant value within a small voltage step, while on the return sweep the capacitance value degrades first suddenly and then very gradually till complete pull-out. As
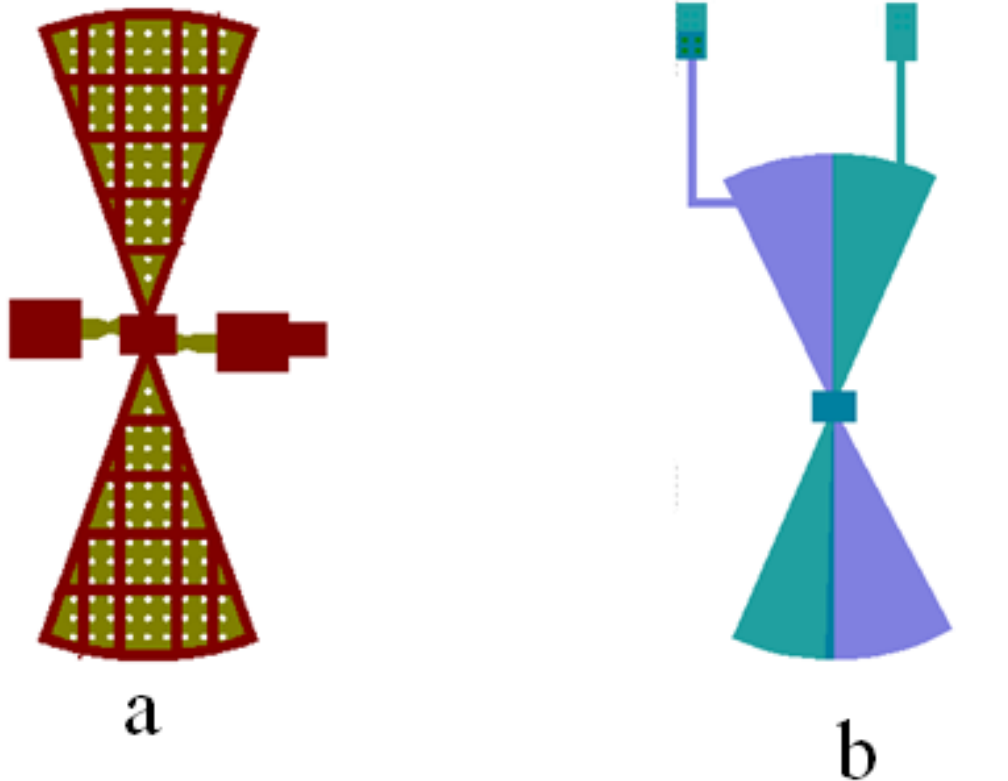
Figure 6.11: a)The layout and b) the actuation pad of Varactor 3.

expected from the very slender suspension spring the pull-out voltage is very low. Also in this case the curve is very symmetrical.

6.4.5 Varactor5

The outer radius of the butterfly structure of varactor 5 is 400 μm and the suspension spring is a meander with two bends. In this case the spring is build out of the two electroplated gold layers, i.e. both thin and the thick gold for a total thickness of 5.4 μm. The choice was motivated by the intention to make the suspension springs , stiffer with respect to vertical
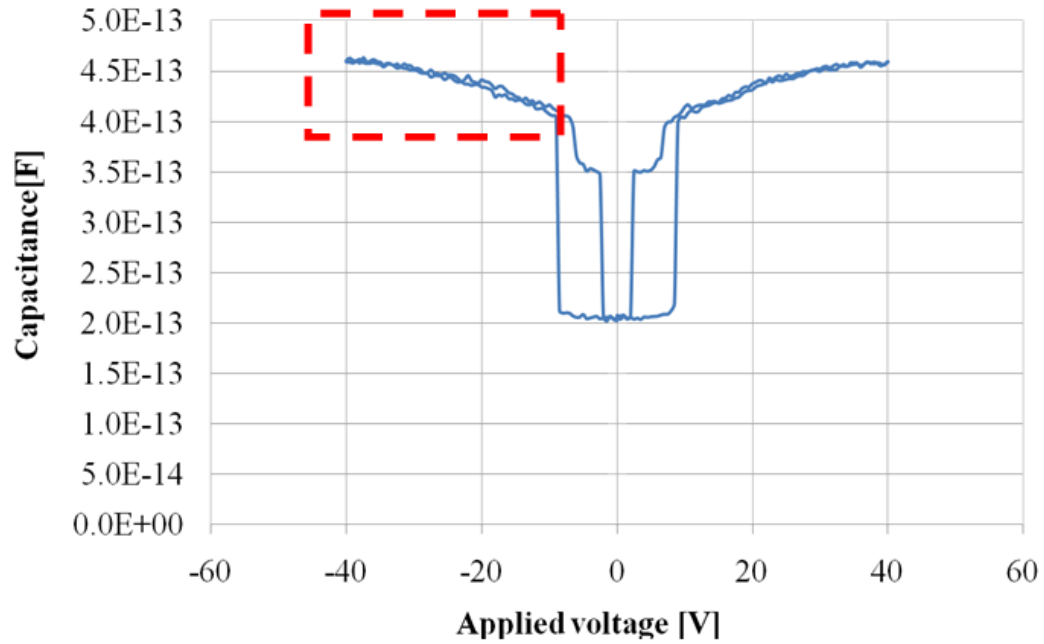
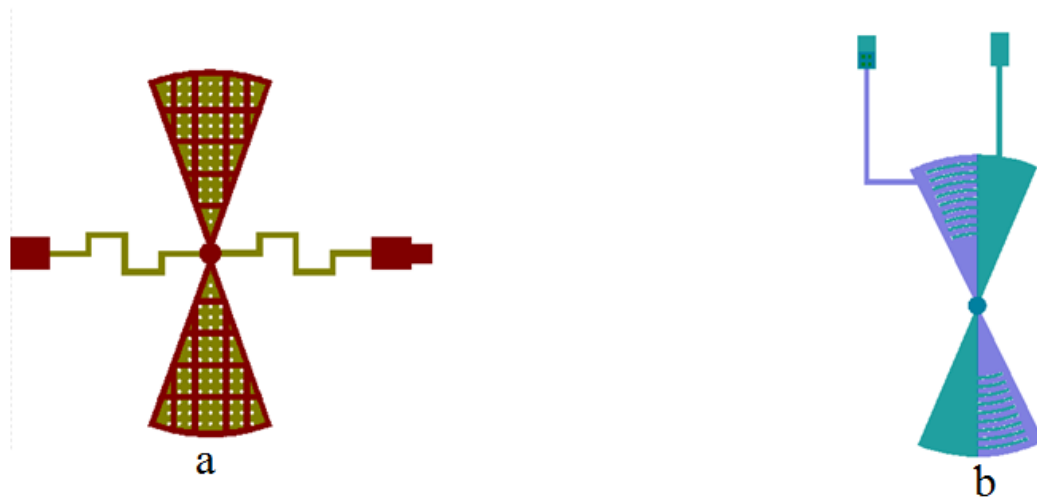Figure 6.12: The experimental CV curve of Varactor 3.

Figure 6.13: a)The layout and b) the actuation pad of varactor 4.

bending than to lateral bending, within the possibilities offered by the fabrication process.The layout of the structure, the actuation pad are shown in Fig 6.15 ,and obtained experimental CV curve are shown in fig 6.16.
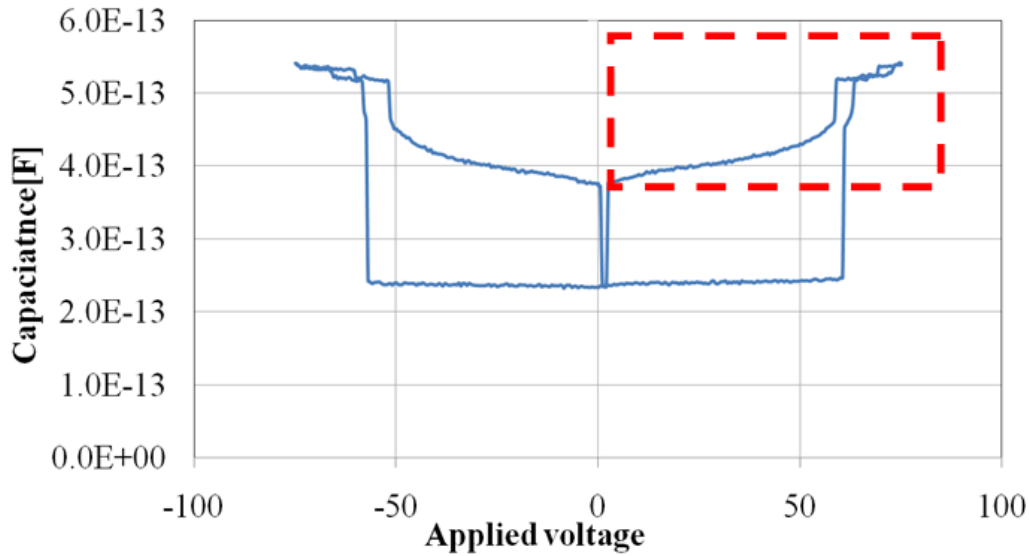
Figure 6.14: The experimental CV curve of Varactor 4.

The CV curve of this device is dominated by the switch behaviour. The first part of the voltage sweep shows a parabolic shape as expected from the slowly narrowing of the gap operated by the increasing electric force. After pull-in the curve shows some irregularities but no clear behaviour. Nonetheless the curve is perfectly symmetric with respect to voltage.

6.4.6 Varactor6

The outer radius of the butterfly structure of varactor 6 is $350\mu m$. The suspension spring is a meander spring similar to the previous device, in this case with a single bend. Also this spring is build by stacking the thin gold and the thick gold for a total thickness of 5.4 μm. The reduced number of bends in the meander springs makes them even stiffer in the vertical direction but, in turn, increases the torsion stiffness. The layout of the structure and the actuation pad are shown in Fig 5.17 a and b respectively

Figure 6.15: a)The layout and b) the actuation pad of Varactor 5.
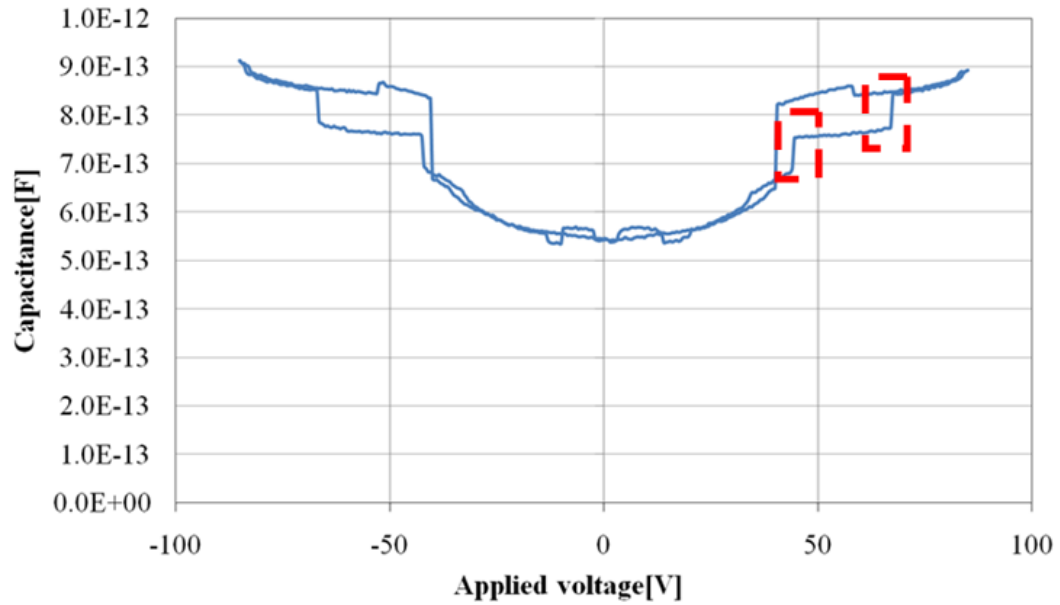
Figure 6.16: The experimental CV curve of Varactor 5.

the obtained CV curve are shown in fig 6.18. This design variant shows a true switch like behavior without any additional features. The first part of the polarization ramp has a parabolic shape as expected in a switch. Then pull-in occurs when the capacitance reaches a fairly constant plateau value. The slight increase still observed is very likely due to the bending of the mobile electrode, which after pull-in is pulled flatter and flatter on the fixed electrode at increasing voltages. Pull-out occurs at intermediated values, as expected for a stiffer suspension spring. Also in this case the CV curve is symmetrical with respect to voltage.

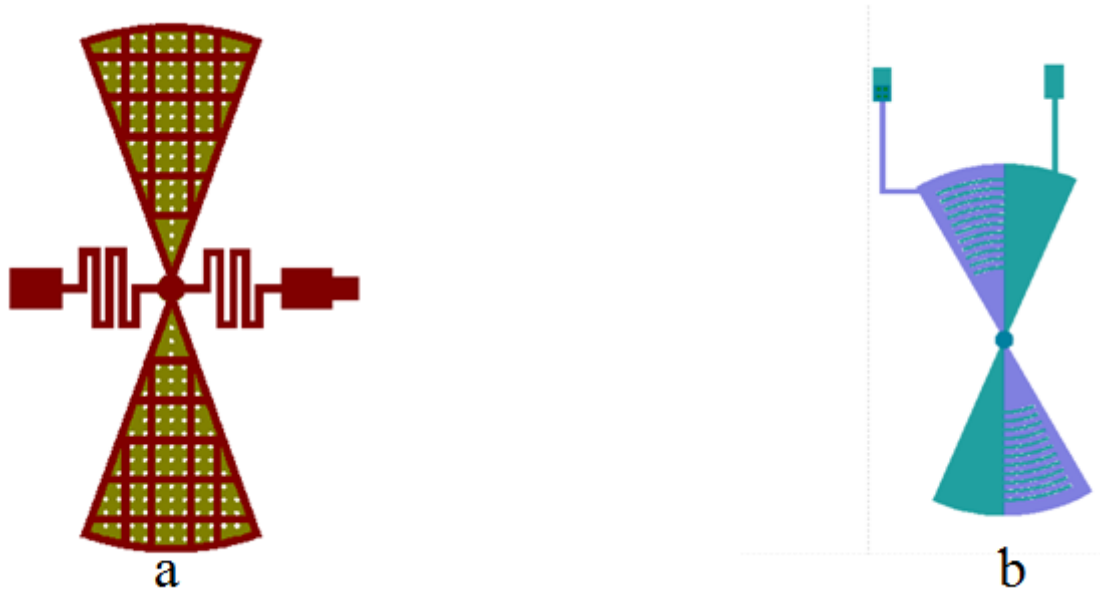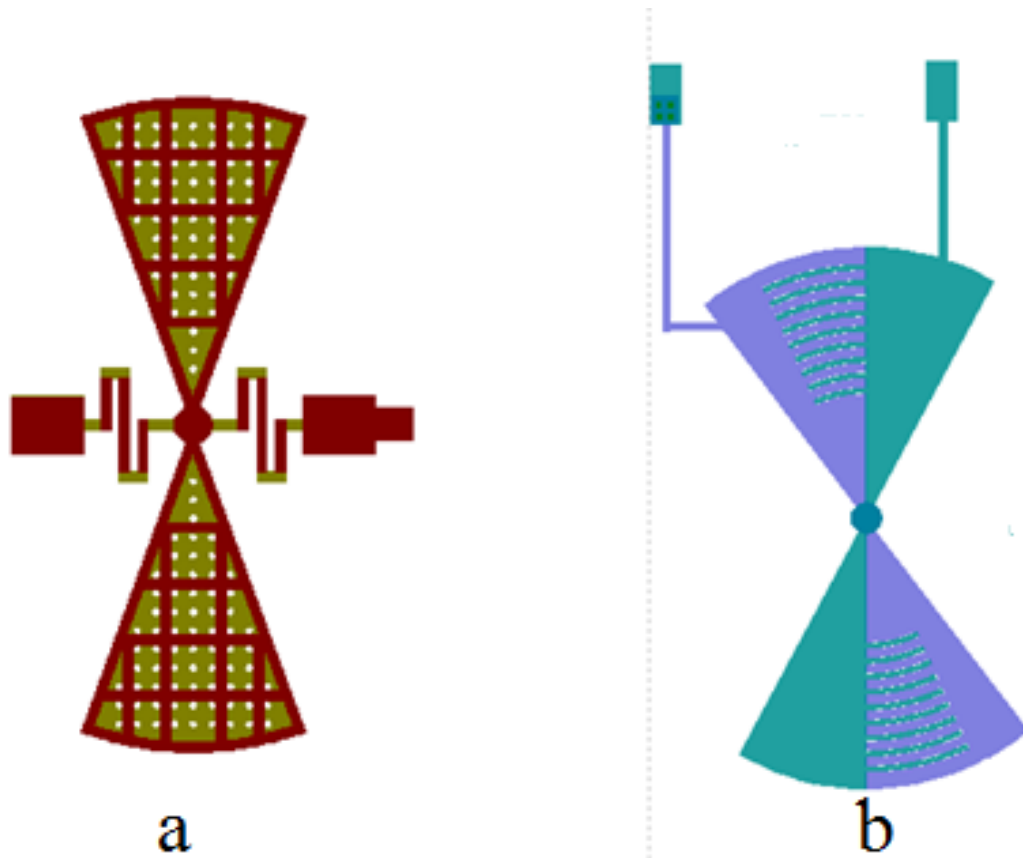
Figure 6.17: a)The layout and b) the actuation pad of Varactor 6.
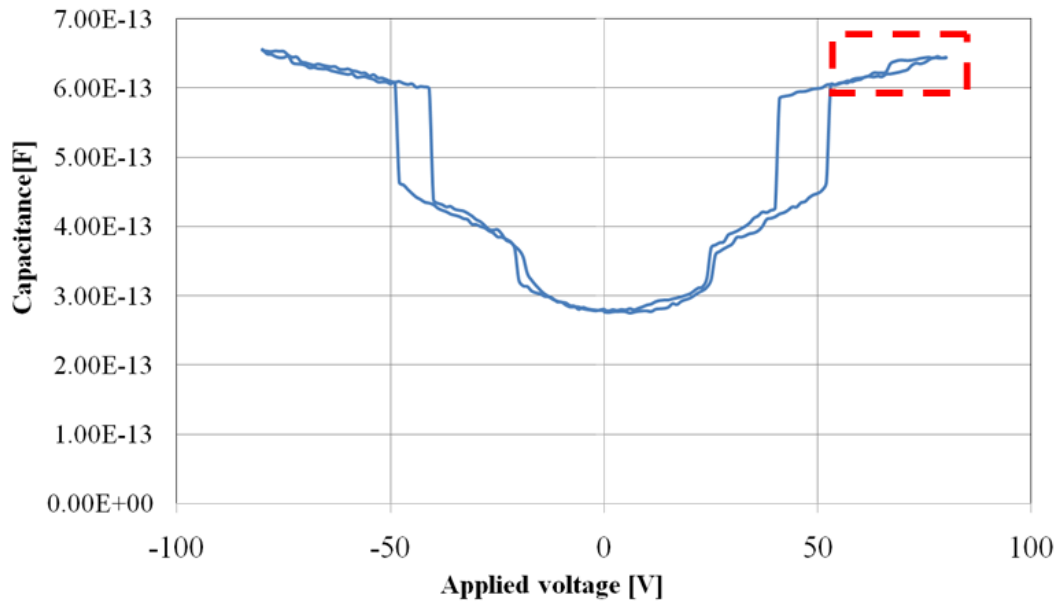
Figure 6.18: The experimental CV curve of Varactor 6.

6.4.7   Varactor7

This device differs from the other variants presented up to now as the overlapping fixed actuation electrode has been removed and substituted by a laterally placed electrode in the attempt to increase the pull in voltage, i.e. reduce the chance of premature pull-in of the whole structure as shown by the excerpt of the layout reported in Fig 6.19. Fig 6.19 respectively show a) the layout b) the actuation pad, while fig. 6.20 shows the obtained experimental data. Already from a purely qualitative point of view it is clear that in this way the forces developing between the mobile electrode and the fixed actuation pad are much more in plane with the wafer surface and much less orthogonal to the wafer surface. The rest of the design has been kept as before except for the digits of the sensing electrode which have been removed. As suspension spring a meander type spring with one bend has been chosen.
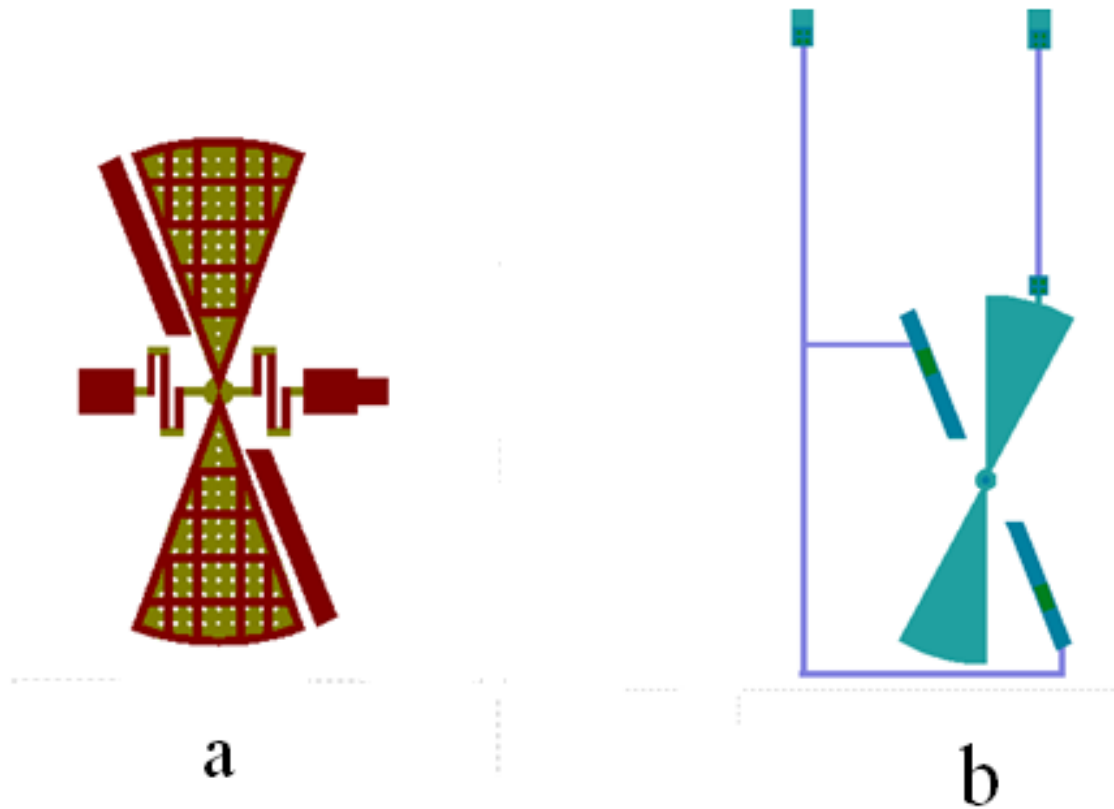
Figure 6.19: a)The layout and b) the actuation pad of Varactor 7.

6.4.8   Varactor8

The last device variant designed is based on the general layout presented above (varactor 1-6). In this case the major change has been a pillar added in the centre of rotation of the structure, about 1/3 of the gap height, that should act as a stopper, i.e. a turning point after the collapse of the structure onto the fixed electrodes. In this case if the mobile structure is stiff enough a complete collapse of the structure on the electrodes can be avoided. Fig 6.21 show a) the general layout of the device b) the actuation pad and the obtained CV curve are shown in Fig 6.22 . Also this design shows a true switch behavior like varactor design 6 without any additional
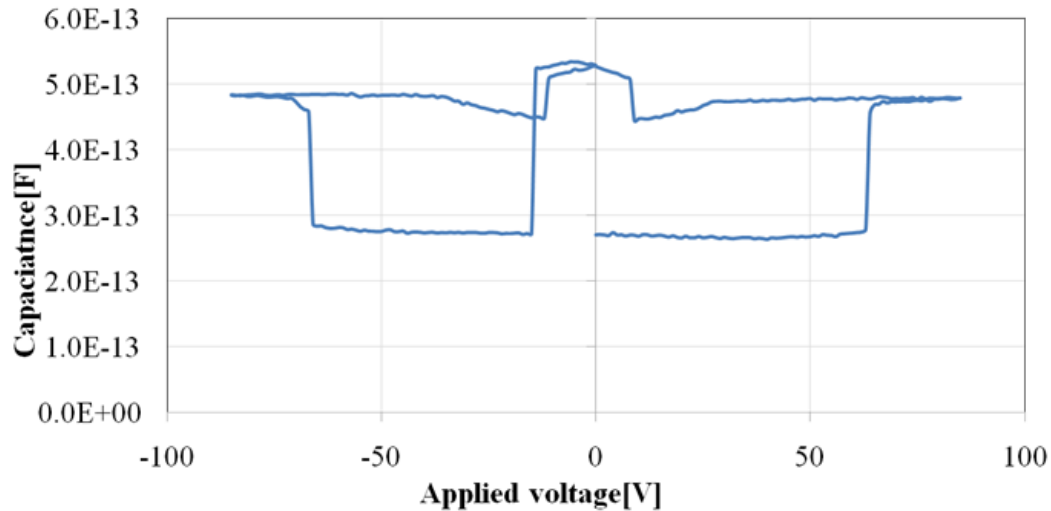
Figure 6.20: The experimental CV curve of Varactor 7.

features. Also in this case the CV characteristic is symmetrical with respect to the voltage.

6.5   Transient Dynamic Characterization

Due to the fact that the basic characteristic of the varactors is in any case dominated by a switch-like behaviour also some transient dynamic characterizations have been performed on these devices. At first for this measurment two device types have been selected , varactor 5 and varactor 6 which only differ for the number of meander type suspension spring and in the case of varactor 5 both thin and thick gold layer used in all of the meander. Fig 6.23 shows the set up for dynamic maesurmnet ,Fig 6.24 and 6.25 respectively show the result of the transient dynamic measurment of varactor 5 for different applied voltage and for shorter time scale. Fig 6.26 and fig 6.27 shows the result of the varactor 6 respectively for different applied voltage and for shorter time scale. The comparison between varactor
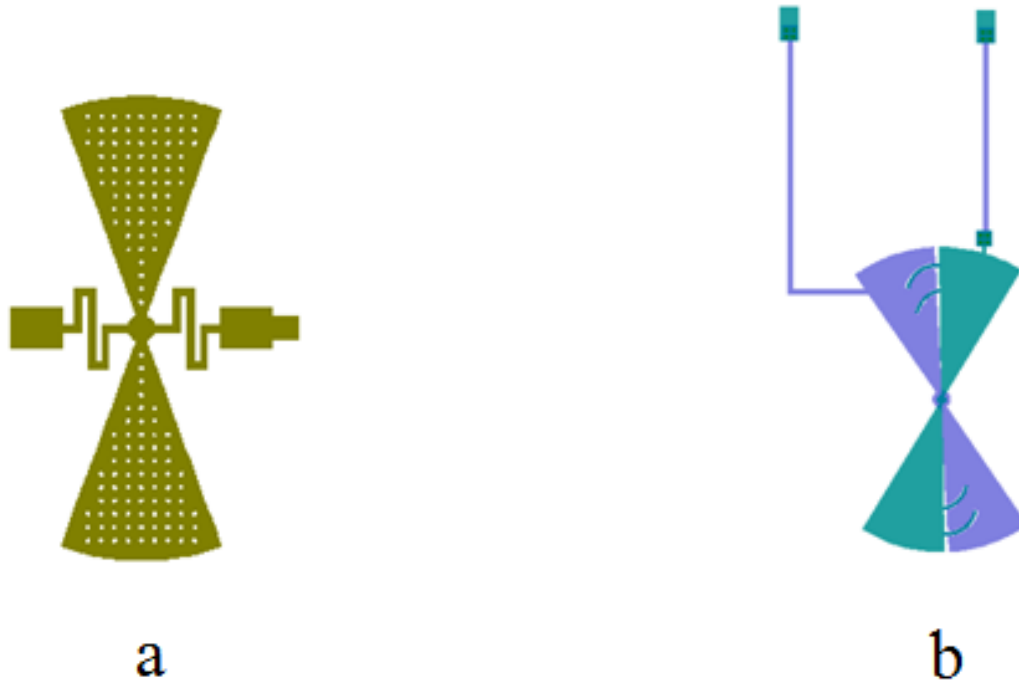
Figure 6.21: a)The layout and b) the actuation pad Of Varactor 8.

3 and varactor 6, where varactor 3 has stiffer suspention springs, can be
seen in Fig 6.28 and Fig 6.29 for an applied voltage of 80 V. The varactor
with the meander spring shows a damped ringing in the release transient,
while the device with the much stiffer suspension springs shows no ringing
at all. The height difference in the displacement after actuation is very
likely due to a non complete actuation of this device. As shown in chapter
5 the closure time of the structure becomes shorter with higher applied
voltages. In this case the times lowers from ~25 μs at 50 V to less than 5
μs at 80 V, which implies that in spite of the odd shape of the structure
the response time can be really fast.
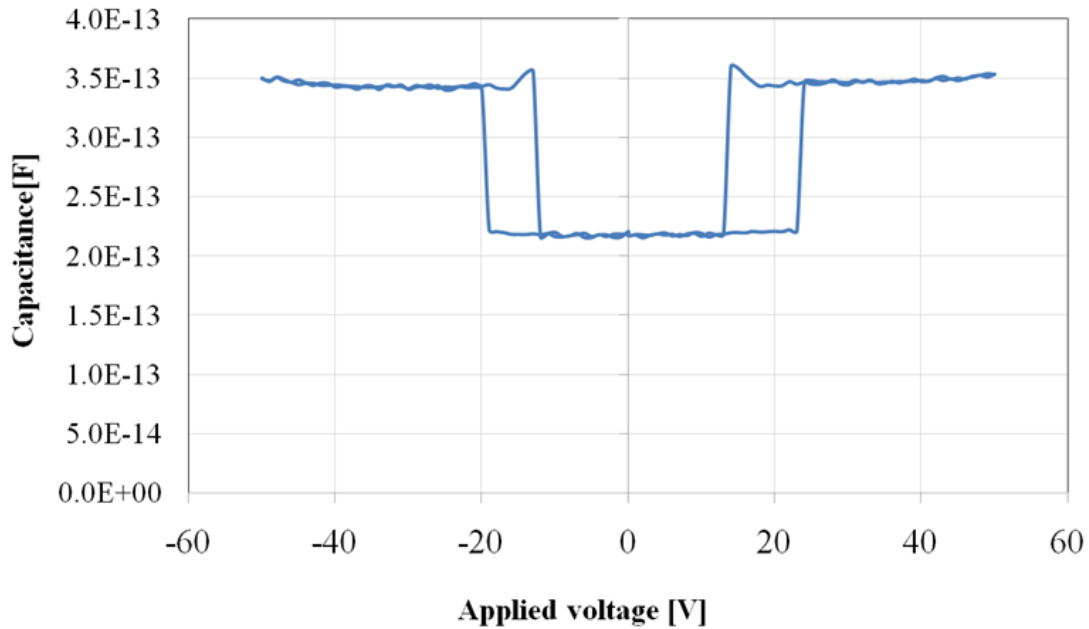
Figure 6.22: The experimental CV curve of varactor 8.

6.6 Analysis and Discussion

As described above the devices differ slightly in the radius of the outer border of the butterfly structure, which is 345-350 μm for variants 3, 4 and 6, 370 mm for varactors 1 and 2, and 400 μm for variant 5, while the overall shape of the mobile and fixed electrodes is the same for all devices. The main effect of this parameter is a change in the absolute value of the capacitance, i.e. larger devices have higher capacitance values. The real difference between devices lies in the type of the suspension springs. In this respect Three different types of designs have been tested: meander type springs in thin gold layer in varactor 1 and 4, straight leaf springs in varactors 2 and 3 and meander type springs in thin and thick gold in varactor 5. Fig 6.30 shows in detail the meander type spring and the leaf type spring in thin gold, while Fig. 6.31 shows the meander spring in both thin
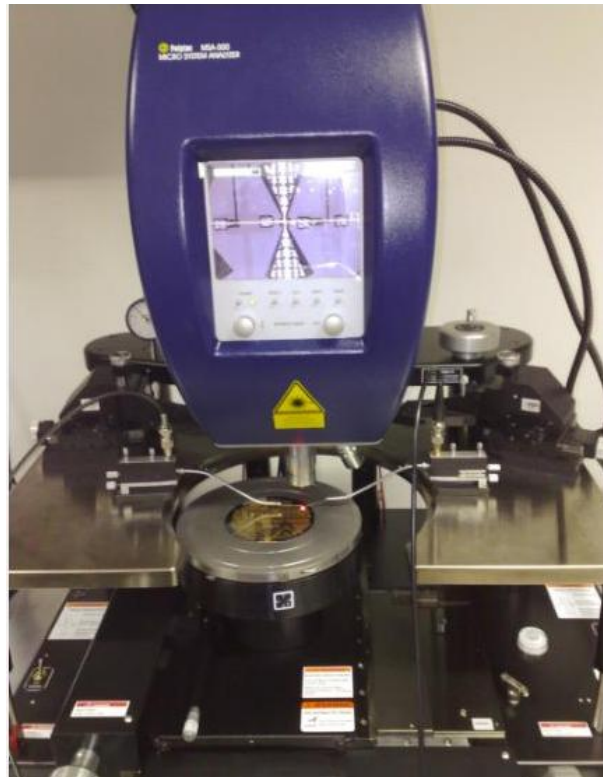
Figure 6.23: Picture of one of the varactors during the transient dynamic characterization.
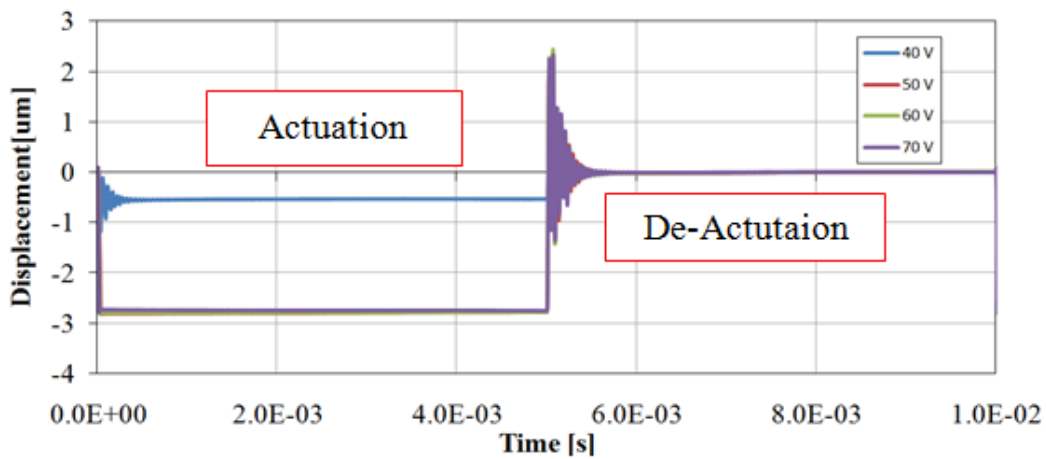
Figure 6.24: Transient behaviour of varactor 5 at different applied voltages.

and thick gold of the varactor 5. The primary objective of the different spring designs was to test different torsion spring constants as this will be
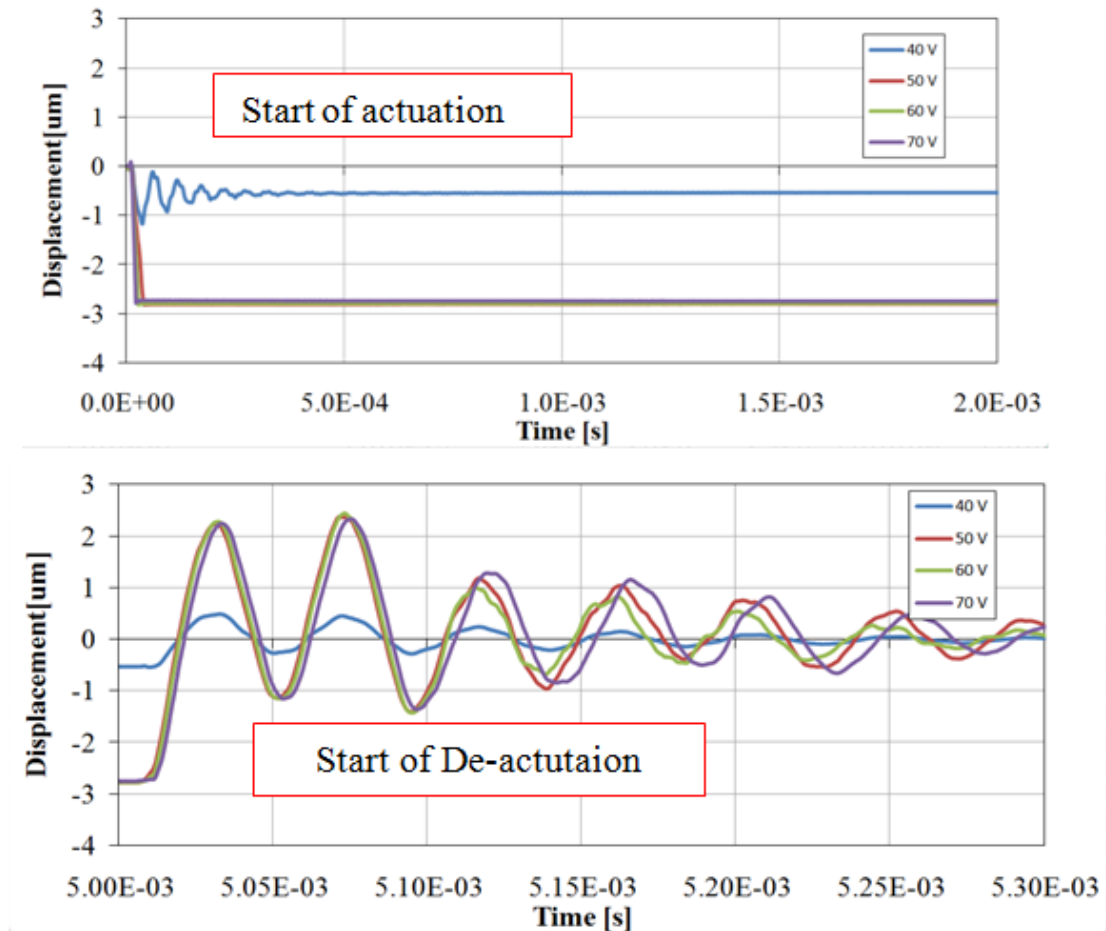
Figure 6.25: Transient at closure and release on a short time scale of Varactor 5.

one of the antagonist forces to the weak in plane electrostatic force. In this technology it is not possible to design a spring with a high spring constant for vertical bending and a very low spring constant for lateral bending. In fact this would require structures with an extremely high aspect ratio, that is not feasible because of technology limitations. As a result, from the beginning of the project it was accepted that the devices will go into pull-in. This happened for all devices and according to the stiffness of the single springs the devices are characterized by different values of pull-in and pull-out voltages. In Table 6.1 these values are summarized for all 8
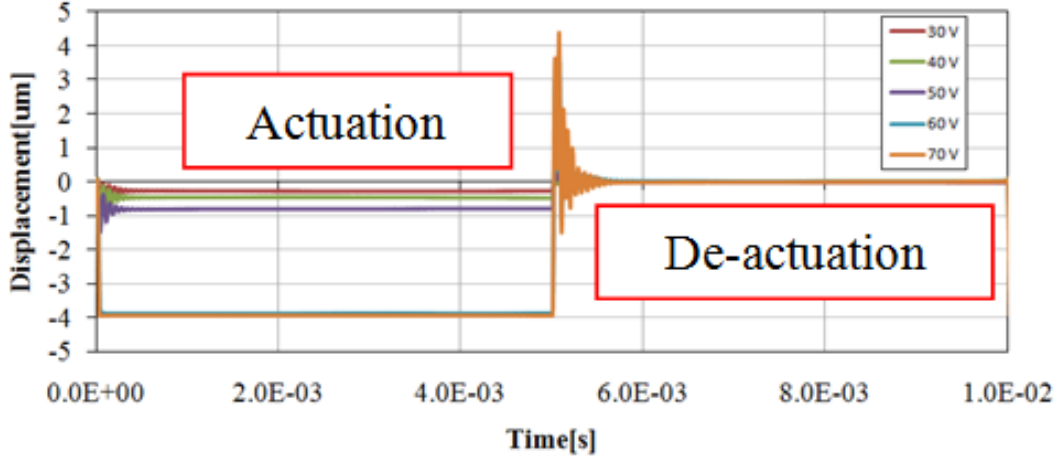
Figure 6.26: Transient behavior of varactor 6 at different applied voltages .

design variants. As pointed out above, 4 devices out of 8 show next to a basic switch-like behaviour also additional features in the CV curve, i.e. after pull-in and prior to pull-out these devices show a significant change in the capacitance value, which one would expect if the structure rotates after pull-in. In order to estimate the degree of rotation that could correspond to this capacitance change one has first to determine the capacitance value immediately after pull-in or prior pull-out (C1) and the capacitance of the plateau value (C2). Where possible these values have been reported in Table.6.1. The rotation eventually corresponding to this capacitance change can be roughly estimated by considering that the capacitance difference is due to an increased overlap between the two electrodes. Considering in any case a small angle of rotation, the area of this overlap is twice the area of the small triangle formed by the radius of the outer circular border of the butterfly structure and the small segment due to the rotation:

$$A_\theta = a^2\theta \qquad (6.1)$$
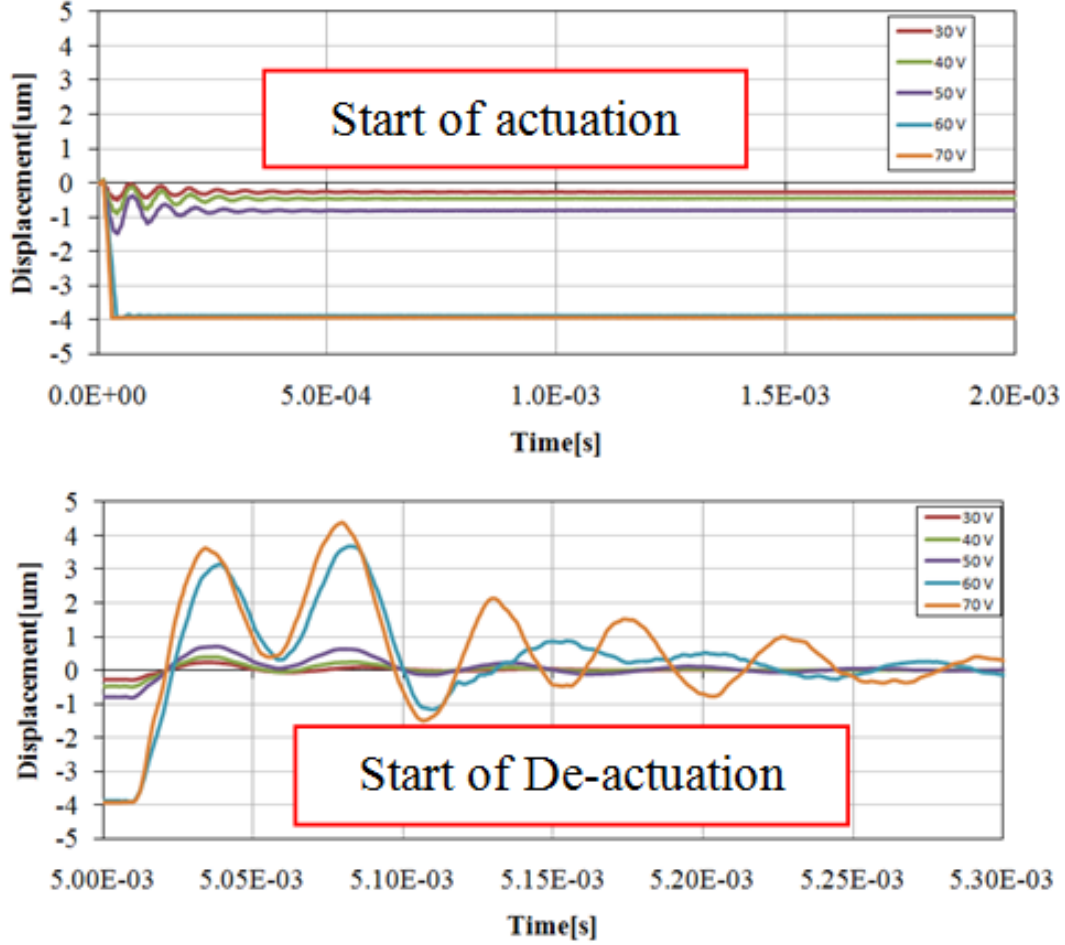
Figure 6.27: Transient at closure and release on a short time scale of varactor 6.

where a is the outer radius of the butterfly wing and θ is the angle of rotation. The corresponding capacitance difference is:

$$\triangle C = \frac{\varepsilon_0 \varepsilon_{0x} A_\theta}{d_{eff}} \tag{6.2}$$

where ε_0 is the permittivity of the vacuum, ε_{0x} the dielectric constant of oxide and d_{eff} the effective oxide thickness. The effective oxide thickness is the oxide thickness increased of a term taking into account the residual air gap created by the surface roughness of the two touching surfaces and
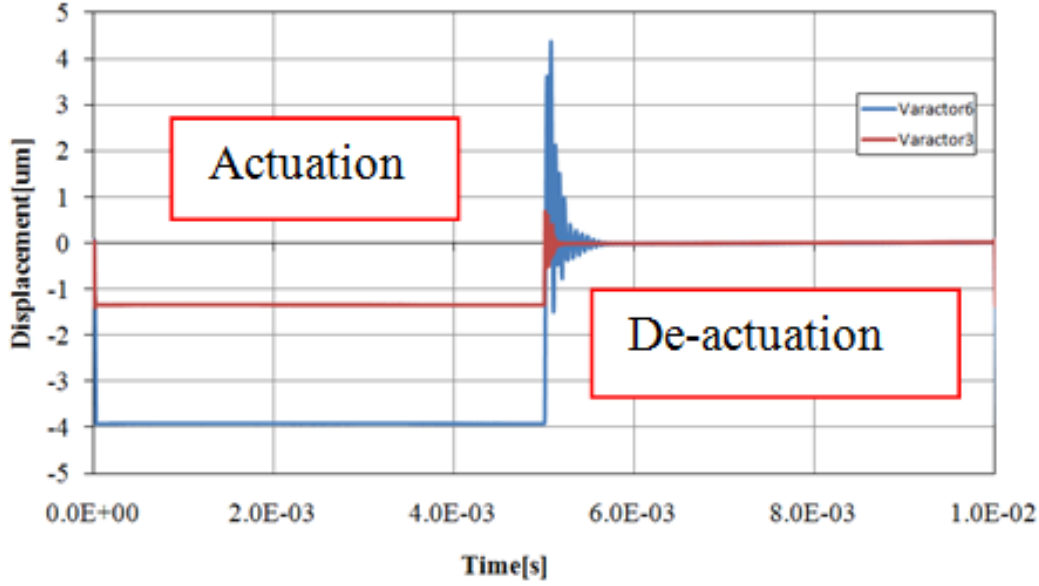
Figure 6.28: Transient behaviour of varactor 6 and varactor 3 at different applied voltage.

is expressed as:

$$d_{eff} = d_{ox} + \varepsilon_{ox}d_{air} \tag{6.3}$$

where d_{air} is the residual air gap caused by the surface roughness, typically in the order of 60 nm. These expressions have been used to estimate the rotation angle for those devices that show this peculiar CV characteristic and the obtained values have been listed in Table 6.1. The values are in the order of a few degrees, ranging from a minimum value of 42 arc min to a maximum value of 1 degree and 46 arc min, consistent with the expectations. In order to fully describe the expected CV characteristic due to rotation one has to start considering all forces acting on the mobile electrode. As only in plane forces are of importance once pull-in has been reached and the problem has radial symmetry, one has to consider actually the moment of these forces with respect to the centre of the structure, i.e. the turning point. Three moments govern the problem and balance
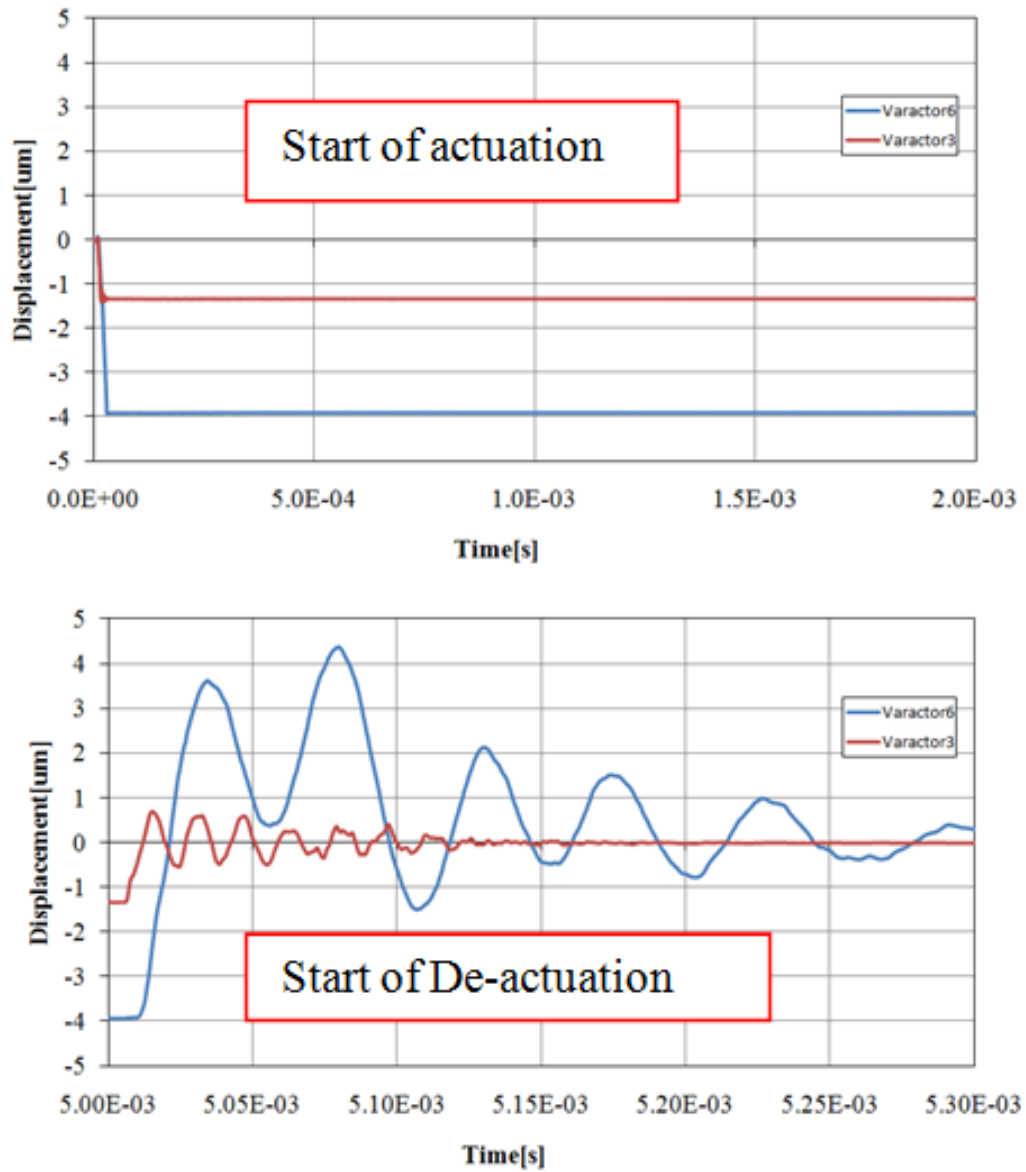
Figure 6.29: Transient at closure and release on a shorter time scale of Varactor 6 and 3.

each other: the moment generated by the lateral electrostatic force M_{el}, the opposing torsion moment of the suspension springs M_t and the antagonistic moment generated by the friction between the two electrodes M_f.

$$M_{el} = M_t + M_f \tag{6.4}$$

Figure 6.30: Detailed view of the a) meander spring and b) leaf type spring in thin gold.

The lateral electrostatic force F_{el} developed between the two electrodes is independent from the overlap and depends only on the voltage applied and can be expressed as:

$$F_{el} = \frac{\varepsilon_o \varepsilon_{ox} V^2}{d_{eff}}$$

(6.5)

while the friction force F_f is

$$F_f = \mu_f \varepsilon_0 \varepsilon_{0x} (A_0 + a^2 \theta) \frac{V^2}{d_{eff}^2}$$

(6.6)

where μ_f is the friction coefficient, a material constant specific to the two touching surfaces, their materials and surface roughness and A_0 is the fixed area overlap due to the interdigits of the two fixed electrodes. The torque moment M_t generated by the suspension springs is expressed as :

$$M_t = K_t + \theta$$

(6.7)

where k_t is the torque constant of the suspension springs. Substituting these expressions in the balance equation of the moments gives:

$$\frac{\varepsilon_0 \varepsilon_{ox} a^2 v^2}{d_{eff}} = K_t \theta + \mu_f (A_0 + a^2 \theta) \varepsilon_0 \varepsilon_{0x} a \frac{V^2}{d_{eff}^2}$$

(6.8)
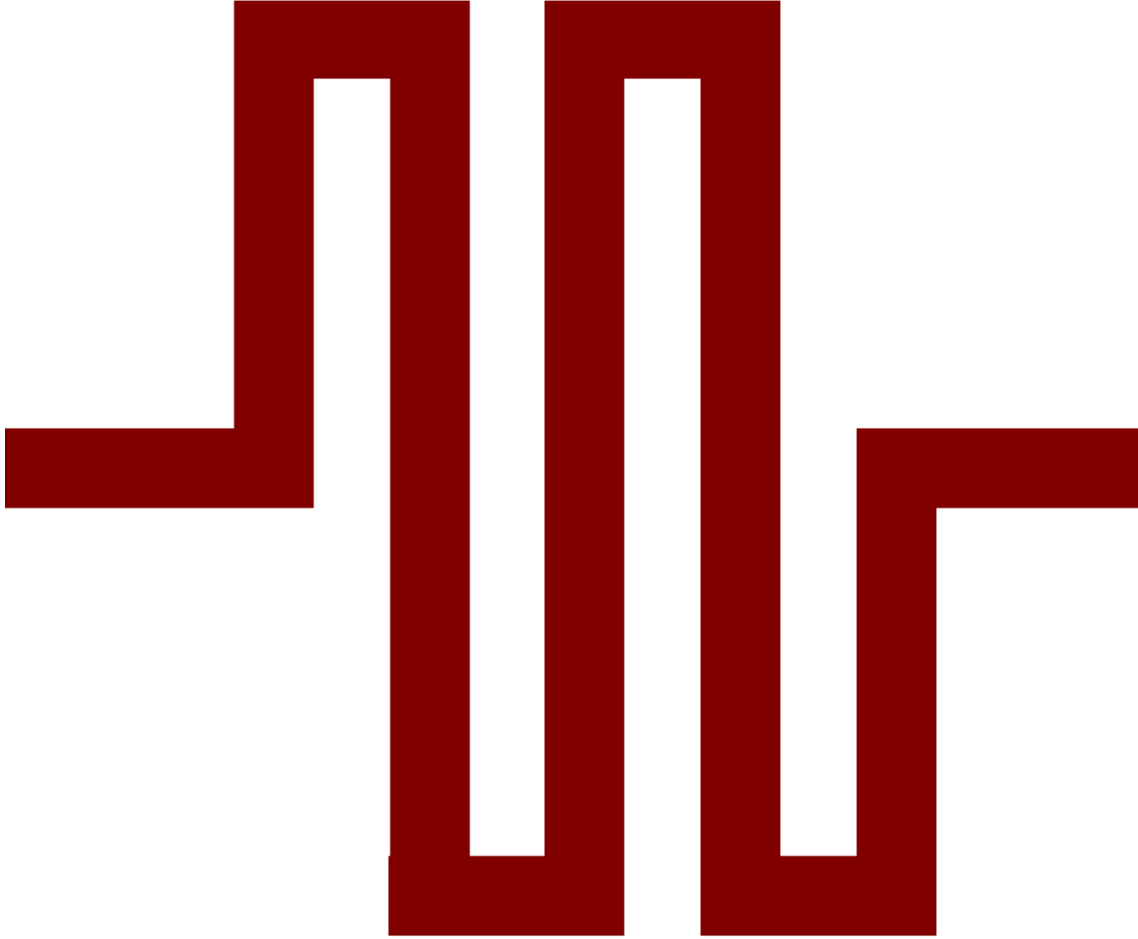
Figure 6.31: Detailed view of the meander type spring in thin and thick gold.

Expressing the rotation θ in terms of applied voltage gives the following formula:

$$\theta = \frac{\varepsilon_0 \varepsilon_{0x}(\frac{a^2}{d_{eff}} - \mu_f A_0 \frac{a}{d_{eff}^2})V^2}{K_t + \mu_f \varepsilon_0 \varepsilon_{0x} a^3 \frac{V^2}{d_{eff}^2}} \qquad (6.9)$$

Once the dependence of the rotation on the applied voltage is known one can easily express the capacitance curve in terms of the rotation:

$$C = C_0 + \varepsilon_0 \varepsilon_{0x} \frac{a^2 \theta}{d_{eff}} \qquad (6.10)$$

Device	Pull in Voltage [V]	Pull out Voltage [V]	C1 Pull in [pF]	C1 Pull out [pF]	C2[pF]	Estimated rotation	
						[Grad]	[Min]
Varactor1	40	20	0.553	0.278	0.688	1	46
Varactor2	41	20	0.404	0.289	0.577	1	9
Varactor3	9.5	2	0.404	0.206	0.457	1	14
Varactor4	61	57.5	0.452	0.373	0.518	0	42
Varactor5	44.5	42.5	0.753	0.827			
Varactor 6	53	24	0.604	0.324			
Varactor 7	64		0.456				
Varactor 8	21	13	0.346	0.218			

Table 6.1: Summary of the principal electromechanic parameters of the devices.

The dependence of the rotation angle on the applied voltage has the general expression:

$$y = \frac{x^2}{1 + x^2} \tag{6.11}$$

In Fig. 6.32 the graph of this generic curve is shown. The distinctive features of the curve are the parabolic part near the zero and the saturation at high values. These can also be found in all curves analyzed above which show an additional change in capacitance after pull-in. All of them have a first part that is similar to a parabola, i.e. after the pull-in the capacitance increases more than linearly with the applied voltage. Depending on the stiffness of the suspension springs this feature can be more evident like for varactor 2 and 4 or less evident as for varactor 1 and 3. The second characteristic of the general curve, i.e. the saturation, can be seen only in device 2. In all other cases the transition to a constant capacitance value is abrupt. The reason for this may be an additional friction resistance not accounted for in the very simple expression used for the model. Nonetheless the qualitative correspondence, at least in selected cases, between this very simple model and the measurements is good and suggests that the

additional capacitance changes in the CV curves observed together with the classical switch type behaviour is actually due to a small rotation of the structure. From this analysis we can conclude that all those structures which have a sufficiently weak suspension spring that generates only a small torsion moment can rotate after pull-in, while those structures which have stiffer suspension springs don't give rise to a rotation. Of course this work is for the moment only a preliminary proof of principle. In order to design and realize a tuneable capacitor on this electro-mechanic principle also a quantitative fit of the model with the measurements will have to be achieved. This refined and validated model can then be used to design a device optimized for an RF application.
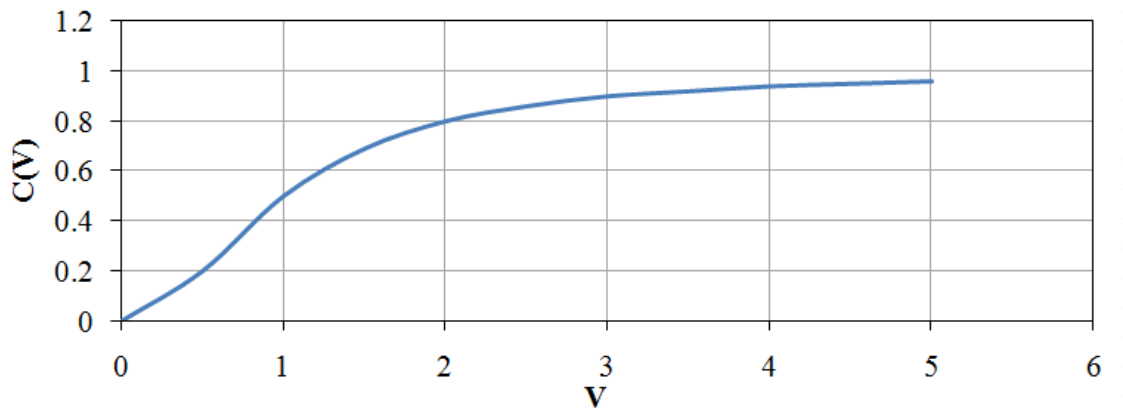

Figure 6.32: General shape of the curve of the expression of the rotation angle vs the applied voltage.

Chapter 7

Conclusion

The research work reported and summarized in this thesis contributed to the field of RF MEMS devices, which nowadays are gaining more and more importance due to the widespread use of RF applications both in consumer electronics and telecommunication. Europe is heavily involved in the development of Micro System Technologies and a small but active community is involved in the RF MEMS field. Inside this community FBK is active in the development of technologies which play a crucial role. In particular FBK has been developing since years a proprietary platform concept for RF MEMS switches and low loss RF components finalized to the monolithic integration of complex RF circuits such as switching matrixes, filters and phase shifters, for ground based and satellite applications. While in the early stages of the technology development the RF aspects of the devices played a major role, now the attention is shifting more and more towards the mechanical and electromechanical aspects because these subjects determine important characteristics like switching speed and partially influence the long term reliability of the devices. This thesis is focused on the dynamic behavior of RF MEMS devices, which is of great interest not only for the switching speed of RF switches but also for some reliability aspects and for a new and unusual varactor concept, where an attempt is made to ex-

ploit an in-plane movement in order to build a compact and robust tunable capacitor. In the first part of the research work considerable time has been invested in developing a numerical modeling procedure able to describe the devices both from static and dynamic point of view. With ANSYS Multiphysics a three-step modeling procedure has been set up and validated on devices build with the well established FBK RF MEMS process. The numerical simulation first establishes static device characteristics as pull-in and pull-out voltages. Next a modal analysis identifies the mechanical frequency spectrum of the structures. Finally a full dynamic model is built which takes into account the mechanics of the structure and the fluid dynamics of the surrounding gas. This modeling concept has been validated on selected devices and a good agreement has been found with the measurements. The procedure has then been used to investigate the relevance of the dynamic characteristics of devices to different design parameters. A total of six parameters or conditions have been studied. Among these the most significant ones are the applied voltage, the gap height, the material and, last but not least, the introduction of specific stoppers. The latter solution, originally designed to reduce the oxide charging, which is a common problem of these devices, showed to be quite effective in reducing the squeeze film effect. The second part of the work has been dedicated to the electromechanical characterization of the devices. To this end a bottom up approach was followed. First a structural characterization was performed with an optical profilometer in order to assess the topography of the devices. This analysis was then followed by the measurement of the principal electromechanical parameters of the structures and the results were compared with the simulated values. In general a good agreement could be found. Finally, with the help of the equipment of the University of Padova , a full transient dynamic characterization was successfully performed. Future work on these topics will have to focus on the optimization

of the device parameters that have a significant impact on the dynamic performance. The validated modeling procedure can now be adopted to evaluate the new designs. In parallel to this work a new concept of tunable capacitor has been developed as well. This device is based on the in-plane forces which develop in a parallel plate capacitor. This work is mainly done with an experimental approach rather than a modeling approach, because it was clear from the beginning that modeling of the structure would be simple. Therefore 8 different structures have been designed, fabricated and measured. All design variants are based on a butterfly structure with different types of suspension springs and with variations of the actuation electrodes. The optical characterization shows that all realized structures fulfill the minimum requirements of planarity to be sufficiently compliant to the project. The electromechanical characterization has been carried out with CV measurements. As expected the general behavior of all devices is dominated by a switch like behavior, but 4 out of 8 devices show also additional features in the CV characteristics that are compatible with a small rotation of the structure in the collapsed state. The devices with the weakest springs present this behavior very clearly and in a repeatable manner. Anyway the detected rotations are very small, in the order of a few degrees only. The small entity of rotation prevented up to now a direct measurement (e.g. by optical means) of the displacement. Nonetheless the capacitance variation associated with the rotation is not negligible. Moreover, it was possible to develop a simple mechanical model that qualitatively reproduces the measured CV characteristics, endorsing the claim that there is an in-plane rotation of the structure during polarization. All of these first results on this very unusual concept are very encouraging, as they show that a mechanical tunable capacitor with in-plane motion is feasible, even if this could be done only in the collapsed mode and not in the suspended mode. The latter feature is not necessarily a negative

aspect as this implies that device works without suspended parts, which, during operation, will make it less sensitive to vibrations and sudden accelerations. Future work on the tunable capacitor should concentrate both on the consolidation of the experimental evidence of the functionality of the concept and on the optimization of the mechanics of the device. In addition some other aspects such as the friction of the rotating structure should be addressed as well, and included in a quantitative model. Also the tuning range has to be increased in order to fully develop the device and to become of interest for practical applications. This PhD research work proved to be successful in providing a validated numerical modeling approach for the dynamic behavior of RF MEM structures. In addition the main parameters in-fluencing the dynamic characteristics of the MEMS switches have been identified. In the second part of the work an interesting new concept for a tunable capacitor has been demonstrated.

7.1 Acknowlegment

Dr. Paola Farinelli for allowing me to use some of the structures designed by her for the work of her Ph.D. thesis. My Special thanks to Dr. Alessandro Faes and Dr. Flavio Giacomozzi for helping, reading and commenting on my thesis and guiding me in the Laboratory works, respectively. My friendships along the way have been invaluable. For this I thank the entire MEMS group of the Foundation Bruno Kessler. I owe special thanks to all of my office-mates and colleagues along the way:Francesco Solazzi Jacopo Iannacci, Viviana Mulloni, Sabrina Colpo, Alvise Bagolini, Giuseppe Resta, Francesca Mattedi, Claudia Giordano, Dan Adrian Vasilache. My parents, my brother and my sister have been there for me throughout my life with advice,encouragement, love and support; thank you. Trento, April 2010.

Bibliography

[1] P. Albert, J. Costello, and P. Slamon. *MEMS in CMOS-21st Century RF and Microwave applications.* pp. 32-36. 2000.

[2] M. Andrews, I. Harris, and G. Turner. *A Comparison of squeeze-film theory with measurements on a microstructure.* vol. 36, pp. 79-87. Sensors and Actuators, 1993.

[3] J. Bergqvist, F. Rudolf, and J. Miasana. *A Silicon Condenser Microphone with a highly perforated back plate.* pp. 266-269. International Conference on Solid-State Sensors Actuators Digest, 1991.

[4] B.Pillans. *RF power handling of capacitive RF MEMS device.* pp.329-332. Microwave Symposium Digest, 2002.

[5] A. R. Brown and G. M. Rebeiz. *A high Performance integrated K-B and diplexer.* vol. 47, no. 8, pp. 1477-1481. IEEE Trans. Microwave Theory and Tech, 1999.

[6] E. R. Brown. *RF MEMS Switches for reconfigurable Integrated Circuits.* vol. 46,no. 11,pp. 1868-1880. IEEE Trans on Microwave theory and Techniques, 1998.

[7] G. Carchon, B. Nauwelaers, P. Pieters, and E. Beyne. *Multi- layer thin film MCM-D for integration of high performance wireless front end systems.* vol. 44,no. 2, pp. 96-110. Microwave Journal, 2001.

[8] C.Goldsmith. *Lifetime characterization of capacitive RF-MEMS switches.* EEE MTT-S Digest, 2001.

[9] LIU. Chang. *"Foundation of MEMS".* Illinois ECE Series,Pearson Prentice Hall, 2006.

[10] S. C. Chen and M. Feng. *Low actuation Voltage RF-MEMS switches with signal frequencies from 0.25GHz to 40GHz.* pp. 689-692. IEDM, 1999.

[11] D.Dubuc. *Methodology to assess the reliability behaviour of RF-MEMS.* Gallium Arsenide applications symposium, 2004.

[12] S. Duffy, C. Bozler, J. Knecht, L. Travis, P.Wyatt, and M. Gouker. *MEMS microswitches for reconfigurable microwave circuitry.* vol. 11, no. 3, pp. 106-108. IEEE Microwave Wireless Compon, 2001.

[13] L. Dussopt and G. M. Rebeiz. *a new tuning approach for microwave integrated circuits.* pp.1247-1256. IEEE Trans. on Microwave Theory Tech, 2003.

[14] G.B.Brook E.A.Brandes. *Smithells Metals Reference Book.* pp:1194-1198. Butterworth-Heinemann, 2004.

[15] F.R.Archibald. *Load capacity and time realations for squeeze film.* pp.29-35. tarns of the ASME, 1956.

[16] P.J. French. *"Polysilicon: A Versatile Material for Microsystems".* vol. A99, no. 1-2, pp. 312. Sensors and Actuators, 2002.

[17] C. Goldsmith, T. H. Lin, B. Powers, W-R. Wu, and B. Norwell. *Micromechanical Membrane switches for microwave application.* pp. 91-94. IEEE Microwave Theory and Technique Symp, 1995.

[18] C. L. Goldsmith and D. I. Forehand. *Temperature Variation of Actuation Voltage in Capacitive MEMS Switches.* IEEE Microwave and Wireless Components Letters, 2005.

[19] C.L. Goldsmith, Z. Yao, S. Eshelman, and D. Denniston. *Performance of low-loss RF MEMS capacitive switches.* vol. 8, no. 8, pp. 269-271. IEEE Microwave and GuidedWave Letters, 1998.

[20] P. D. Grant, R. R. Mansour, and M. W. Denho. *A Comparison between RF MEMS switches and Semiconductors Switches.* vol. 27, no. 1. Can.Jou. Elect. Comput. Engineering, 2002.

[21] H. H. Jansen, H. A. C. Tilmans, and K.Baert. *Micromachined devices for space Telecom Applications.* pp.135 - 140. 3rd round table on Micro-Nano Technologies for Space ESTEC, 2000.

[22] B. D. Jensen, L. W. Chow, and K. Kurabayashi. *Force dependence of RF MEMS switch contact heating.* pp:137140. 17th IEEE International Conference, 2004.

[23] B. D. Jensen, H. Kuangwei, and K. Kurabayashi. *Asperity heating for repair of metal contact RFMEMS switches.* pp:19391942. Microwave Symposium Digest, 2004.

[24] J.Maciel. *Recent Reliability Results in RF MEMS.* the 2005 he 2005 IEEEMTT-S Int. Microwave Symposium, 2005.

[25] W. Weaver Jr, S. P. Timoshenko, and D. H. Young. *Vibrations Problems in Engineering.* John Wiley and Sons, 1990.

[26] W.E. Langlois. *Isothermal squeeze films.* pp.29-35. Quarterly of Applied NMathematics, 1962.

[27] L. E. Larson, R. H. Hacket, M. A. Melendes, and R. F. Loher. *Micromachined microwave actuator (MIMAC) technology - a new tuning approach for microwave integrated circuitst.* pp. 27 -30. 1991.

[28] L. Lorenzelli, K. J. Rangra, F. Giacomozzi, B. Margesin, and F.Pianegiani. *On-wafer electro-mechanical characterization of silicon MEMS switches.* pp. 281-285. On-wafer electro-mechanical characterization of silicon MEMS switches, 2003.

[29] Marc. J. Madou and L. P. B. Katehi. *Micromachined devices for space Telecom Applications.* pp.135 - 140. 3rd round table on Micro -Nano Technologies for Space ESTEC, 2000.

[30] S. Melle. *Investigation of dielectric degradation of microwave capacitive microswitches.* pp.141-144. 17th IEEE International Conference on Micro Electro Mechanical Systems, 2004.

[31] J.B. Muldavin and G.M. Rebeiz. *"High-Isolation CPW MEMS Shunt Switches-Part1: Modeling".* vol. 48, no. 6, pp. 10451052. IEEE Transactions on Microwave Theory and Techniques, 2000.

[32] V. Ostaseviciusa, R. Daukseviciusa, and A. Paleviciusa. *Numerical analysis of fluidstructure interaction effects on vibrations of cantilever microstructure.* Journal of Sound and Vibration, 2007.

[33] S. P. Pachec and C. T-C. Naguyen. *"Design of Low Actuation voltage RF MEMS Switches".* pp. 165 - 168. IEEE, MTT-S Digest, 2000.

[34] J. Y. Park, G. H. Kim, and K. W. Chung. *Low actuation Voltage RF-MEMS switches with signal frequencies from 0.25GHz to 40GHz.* pp. 689-692. IEDM, 1999.

[35] D. Peroulis. *RF MEMS DEVICES FOR MULTIFUNCTIONAL INTEGRATED CIRCUITS AND ANTENNAS.* PhD thesis, 2003.

[36] K.E. Petersen. *"Micromechanical Switches on Silicon"*. vol. 23, no. 4, pp. 376-385. IBM Journal of Research and Development, 1971.

[37] K.E. Petersen. *"Silicon as a Mechanical Material"*. vol.70, no. 5, pp. 420-457. 1982.

[38] B.Margesin P.T.Savadkoohi, S.Colpo. *Novel design of a RF-MEMS tuneable capacitor based on electrostatically induced torsion.* 10.1007/s00542-009-0946-7. Journal of Microsystem technology, 2009.

[39] G.M .Rebeiz. *"RF MEMS design and theory"*. vol. 48, no. 6, pp. 10451052. John willey and Sons, 2003.

[40] X. Rottenberg. *Distributed dielectric charging and its impact on RF MEMS device.* 34th European Microwave Conference, 2004.

[41] S.D. Senturia. *"Microsystem Design"*. Kluwer Academic Publishers, 2000.

[42] S.Melle. *Reliability behaviour of RF MEMS.* Semiconductor Conference, 2003.

[43] M. Soyer, K. A. Jenkins, and J. N. Burghartz. *A 3V 4GHz NMOS voltage controlled Oscillator with integrated resonator.* pp.471-476. IMAPS, 2001.

[44] B. Stark. *MEMS Reliability Assurance Guidelines for Space Applications.* 1999.

[45] J. B. Starr. *Squeeze-film damping in solid-state accelerometers.* IEEE Solid-State Sensors and Actuators Workshop, 1990.

[46] W.C-K .Tang. *Electrostatic Comb Drive for Resonant Sensor and Actuators Applications.* phd thesis, 1990.

[47] A. Tazzoli, V. Peretti, E. Zanoni, and G. Meneghesso. *Transmission Line Pulse (TLP) Testing of Radio Frequency (RF) Micro-machined Micro-electromechanical Systems (MEMS) Switches.* pp.295303. 28th Electrical Overstress/Electrostatic Discharge Symposium, 2006.

[48] A. Tazzoli, A. Tazzoli, and G. Meneghesso. *Reliability issues in RF-MEMS switches.* pp. 3134. IRPS 2006, 2006.

[49] H. A. C. Tilmans. *MEMS component for wireless communications.* The 16th European conference on Solid-State Transducer, 2002.

[50] S. P. Timoshenko and J. N. Goodier. *Theory of Elasticity.* McGraw Hill, 1970.

[51] M. Ulm, M. Reimann, and T. Walter. *Capacitive RF MEMS Switches for W-Band.* pp. 25-27. 31st European Microwave Conference, 2000.

[52] A.J. van Roosmalen. *"Microelectronic technology".* Springer, 2006.

[53] www. Radant.com.

[54] www.TeraVicta.com.

[55] J. J. Yao and M. F. Chang. *A surface micromachined miniature switch for telecommunication applications, with signal frequencies.* pp. 384-387. International Conference, on Solid State Sensors and Actuators, 1995.

[56] D. J. Young and B. E. Boser. *A Micromachined variable capacitor for monolithic low noise VCOs.* pp.86-89. Solid State Actuators and Sensors Workshop, 1996.

[57] R. J. Roark W. C. Young. *Formulas for Stress and Strain.* McGraw-Hill, 1989.

[58] Y.Oya. *A reliable and compact polymer-based package for capacitive RF-MEMS switches.* pp. 3134. IEDM Technical Digest. IEEE International, 2004.

[59] X. Yuan, S. Cherepko, C. L. Goldsmith, and C. Dyck. *Initial Observation and Analysis of Dielectric-Charging Effect on RF MEMS Capacitive Switches.* pp. 19431946. IEEE MTT-S International Microwave Symposium Digest, 2004.

[60] P. M. Zavracky, N. E. McGruer, R. H. Morrison, and D. Potter. *Microswitches and microrelays with a view toward microwave applications.* vol. 9, no. 4. International Journal of RF and Microwave Computer Aided Design, 1999.

[61] J. L. Zunino. *Micro-electromechanical Systems (MEMS) Reliability Assessment Program for Department of Defense Activities.* pp.463466. 2005 NSTI Nanotechnology Conference and Trade Show (Nanotech), 2005.